

Search for Resonances in the Three- and Four-Neutron Systems in the ${}^7\text{Li}({}^7\text{Li}, {}^{11}\text{C})3n$ and ${}^7\text{Li}({}^7\text{Li}, {}^{10}\text{C})4n$ Reactions

D. V. Aleksandrov, E. Yu. Nikol'skii, B. G. Novatskii, S. B. Sakuta*, and D. N. Stepanov

Russian Research Centre Kurchatov Institute, pl. Akademika Kurchatova 1, Moscow, 123182 Russia

* e-mail: sakuta@dni.polyn.kiae.su

Received December 1, 2004

The spectra of the ${}^{11}\text{C}$ and ${}^{10}\text{C}$ nuclei from the ${}^7\text{Li}({}^7\text{Li}, {}^{11}\text{C})3n$ and ${}^7\text{Li}({}^7\text{Li}, {}^{10}\text{C})4n$ reactions, respectively, have been measured at a ${}^7\text{Li}$ energy of 82 MeV and an angle of 2° up to excitation energies of 20–30 MeV of the desired multineutrons. The experiments were carried out with a magnetic separator, which made it possible to significantly increase the intensity of a beam by removing scattered particles and to carry out small-angle measurements. The energy spectra are well described by four- and five-particle phase spaces. No evidence has been found for the existence of nuclear stable and resonance states (with $\Gamma < 3$ MeV) of multineutrons. The upper limits have been obtained for the cross sections for the formation of nuclear stable states of $3n$ (1.4 nb/sr) and $4n$ (0.1 nb/sr) in the center-of-mass system. © 2005 Pleiades Publishing, Inc.

PACS numbers: 25.70.Hi; 27.10.+h

1. INTRODUCTION

Numerous experimental and theoretical investigations carried out during the last decades show that there are neither bound nor quasi-stationary states of dineutron and trineutron (see reviews [1–3] and references cited therein) with a lifetime exceeding 10^{-22} s. At present, only the situation with resonance states of the trineutron remains contradictory. In particular, a significant increase in the cross sections for the ${}^3\text{He}(\pi^-, \pi^+)3n$ and ${}^4\text{He}(\pi^-, p)3n$ reactions has been found at an energy of $E_\pi^- = 140$ MeV [4, 5] near the $3n$ threshold. This increase was first attributed to the final state interaction of three nucleons. However, more recent analysis showed that the observed excess of cross sections over the phase-space distribution can also be attributed to the interaction between two neutrons [6]. No deviations from the phase-space distribution were found in the ${}^7\text{Li}({}^7\text{Li}, {}^{11}\text{C})3n$ and ${}^3\text{H}({}^7\text{Li}, {}^7\text{Be})3n$ reactions [7, 8]. Thus, the existence of resonances in three-nucleon system is an open question.

The lightest neutron nucleus that can probably be nuclear stable is $4n$. The discovery of such a nucleus would have fundamental consequences for the existence of heavier neutron nuclei. The upper limit of the binding energy of $4n$ is equal to 3.1 MeV and determined by the nuclear stability of the ${}^8\text{He}$ nucleus. This limit decreases to 1 MeV in view of a known experimental fact that the decay of the ${}^8\text{He}$ nucleus with the emission of ${}^6\text{He}$ prevails over the process with the emission of an α particle [9, 10]. Since the decay into four neutrons is the only channel of the decay of the tetra-neutron ($4n$), $4n$ can exist at an arbitrarily low binding energy. The probability of its decay is reduced due to

the smallness of the phase space of the final state of four particles [1].

Although theoretical estimates testify to the absence of the bound tetra-neutron, its existence is not completely excluded [1–3, 11, 12]. To date, the existence of the nuclear stable tetra-neutron has been reported only in one experimental work [13]. A negative result has been obtained in all the other experiments beginning with [14, 15] and ending with recent works [16, 17], although investigations were carried out with the use of various procedures with beams of π^- and heavy charged particles, as well as with the use of an activation procedure to search for the tetra-neutron in the decay products. Resonances with $T = 2$ have also not yet been detected in the four-neutron system.

More than four decades of investigations seem to show that nuclear stable and quasi-stationary states of the tetra-neutron do not exist. However, recent paper [18] reported the observation of six events associated with the formation of an $4n$ cluster in the reaction of the fragmentation of the nuclei of the secondary radioactive ${}^{14}\text{Be}$ beam with an energy of 35 MeV per nucleon when they interact with carbon. More recently, the observation of 12 events associated with a bound $4n$ cluster in the $\alpha + 4n$ channel in the experiment with a ${}^8\text{He}$ beam was reported [19]. Finally, stable and quasi-stationary states of the tetra-neutron were searched for in the $d({}^8\text{He}, {}^6\text{Li})4n$ reaction [20]. Despite the low statistics, the preliminary result shows that the spectrum of ${}^6\text{Li}$ nuclei near the $4n$ threshold noticeably differs from the five-particle phase space distribution and testifies to the observation of a resonance-like structure in the $4n$ excitation spectrum at 2.5 MeV. These results stimulate

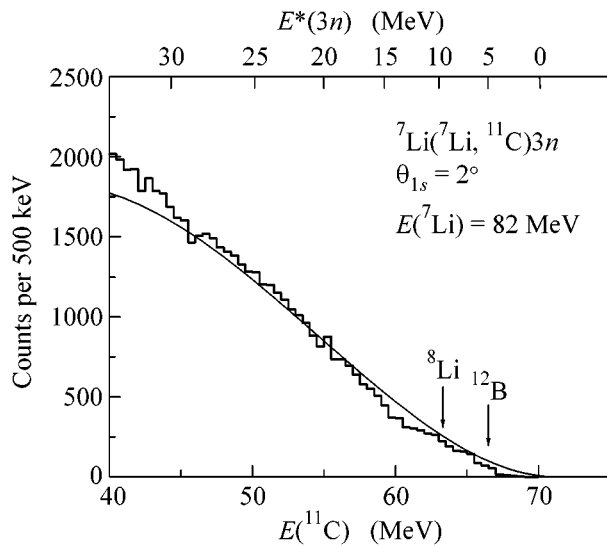


Fig. 1. Energy spectrum of ^{11}C nuclei from the $^7\text{Li}(^7\text{Li}, ^{11}\text{C})3n$ reaction obtained on the MASE magnetic separator at an angle of 2° . The arrows show the positions of the ground states of the ^8Li and ^{12}B nuclei formed in the $^{12}\text{C}(^7\text{Li}, ^{11}\text{C})^8\text{Li}$ and $^{16}\text{O}(^7\text{Li}, ^{11}\text{C})^{12}\text{B}$ reactions, respectively. The solid line is the four-particle phase space.

interest in the problem of the stability of light neutron systems.

The aim of this work is to study the $^7\text{Li}(^7\text{Li}, ^{11}\text{C})3n$ and $^7\text{Li}(^7\text{Li}, ^{10}\text{C})4n$ reactions at small angles with the use of a new procedure based on a magnetic separator. A considerable increase in the beam intensity without an increase in the load of the electronics makes it possible to significantly increase the statistical accuracy of the measured spectra and to reduce the background of random coincidences in a wide energy range, including the region corresponding to nuclear stable multineutrons.

Previously, we studied these reactions at an angle of 10° and a ^7Li energy of 82 MeV using the standard $\Delta E-E$ and $E-t$ analysis [8, 16]. The spectra measured for the ^{11}C and ^{10}C nuclei were well described by the distributions of four- and five-particle phase spaces, respectively. No features testifying to the presence of a bound state and resonances have been found in the mentioned multineutron systems.

2. EXPERIMENTAL PROCEDURE

The measurements were carried out on a $0.3\text{-}\mu\text{A}$ beam of triply charged ^7Li ions accelerated to an energy of 82 MeV at the isochronic cyclotron, Russian Research Centre Kurchatov Institute. A target was manufactured by the vacuum evaporation of metallic lithium enriched in the ^7Li isotope to 99.9% on a thin ($<0.2\ \mu\text{m}$) organic film. The thickness of the target was equal to $0.48\ \text{mg}/\text{cm}^2$ and determined from the energy

losses of α particles from a ^{228}Th α source. The prepared targets were transported to the scattering chamber in a special container with a vacuum lock, which minimized the oxidation of the target.

The spectra of the $^7\text{Li}(^7\text{Li}, ^{11}\text{C})3n$ and $^7\text{Li}(^7\text{Li}, ^{10}\text{C})4n$ reactions were measured by means of a magnetic separator (MASE) [21] with a maximum input aperture of $\pm 1^\circ$. The setup is based on a magneto-optical system consisting of two dipole and five quadrupole magnets forming a double symmetric achromat. The first half of the achromat analyzes charged particles emitted from the target placed at the center of the MASE target block. The second half is focusing. The separated particles are focused at the end of the setup on a detector as a spot with a size $\leq 15\ \text{mm}$. Measurements were carried out using a silicon detector telescope, which includes thin ($30\ \mu\text{m}$) and thick ($0.5\ \text{mm}$) counters for measuring the specific ionization (ΔE) and total energy (E), respectively, and forms a two-dimensional $\Delta E-E$ spectrum. The E counter is included in the scheme of two-dimensional $E-t$ analysis with a flight base of 4 m. Connection to the cyclotron frequency is performed. The time resolution is equal to about 2 ns. The ^{11}C and ^{10}C nuclei from the $^7\text{Li}(^7\text{Li}, ^{11}\text{C})3n$ and $^7\text{Li}(^7\text{Li}, ^{10}\text{C})4n$ reactions, respectively, are selected by coincidence of the respective regions in the two-dimensional $\Delta E-E$ and $E-t$ spectra. The total energy resolution is equal to 400 keV. Since the MASE may pass particles within an interval of 10–15% of the average energy of a detected particle with 100% efficiency at the given magnetic rigidity of the separator, the total energy spectrum is obtained by joining partial spectra obtained for different regimes of the adjustments of the MASE along the overlapping sections on a computer. At a certain adjustment, each sort of particles has its own energy range, and this circumstance enables one to reliably separate the Be, B, and C isotopes. One more advantage of this procedure is that the MASE separates the desired nuclei from scattered particles, which makes it possible to significantly increase the beam intensity without the load of electronics and thereby considerably reduces the background of random coincidences.

3. MEASUREMENT RESULTS AND DISCUSSION

Figures 1 and 2 show the spectra of the ^{11}C and ^{10}C nuclei, respectively, emitted at an angle of 2° in the laboratory system. The upper axes show the excitation energies in the three- and four-neutron systems beginning with the zero binding energy. The measured spectra are similar to each other. In both cases, the cross sections increases continuously up to the excitation energies 20–30 MeV. For calibration, the $(^7\text{Li}, ^{11}\text{C})$ and $(^7\text{Li}, ^{10}\text{C})$ reactions on the ^{12}C and ^{16}O nuclei were used. The spectra for these reactions were obtained at the same angle. Previous measurements [8, 16] show that the

cross sections for the formation of ${}^8\text{Li}$ and ${}^{12}\text{B}$ in the ground states at an angle of 10° are equal to 150 and 100 nb/sr, respectively, in the center-of-mass system. The cross sections for the emission of ${}^{10}\text{C}$ with the formation of the ${}^9\text{Li}$ and ${}^{13}\text{B}$ residual nuclei are equal to 20 and 230 nb/sr, respectively. The positions of the ground states of the mentioned nuclei are shown by arrows in the figure. The absence of any peaks in these positions is evidence that the possible impurities of carbon and oxygen in the target are insignificant and do not distort the spectra of the ${}^{11}\text{C}$ and ${}^{10}\text{C}$ nuclei emitted due to ${}^7\text{Li}$ - ${}^7\text{Li}$ interaction. Since the energies of the nuclei formed on the most probable impurities in the target are at least 3 MeV lower than the energies of ${}^{11}\text{C}$ and ${}^{10}\text{C}$ corresponding to the zero binding energies of $3n$ and $4n$, counts in the region $E_x \sim 0$ can be caused only by the random-coincidence background. In the present measurements, this background is nearly absent due to the use of the magnetic separator.

The energy spectrum of ${}^{11}\text{C}$ nuclei from the $({}^7\text{Li}, {}^{11}\text{C})$ reaction up to an excitation energy of 30 MeV is well reproduced by four-particle phase space for the ${}^{11}\text{C} + 3n$ system (Fig. 1). Background events in the region of the zero binding energy of $3n$ determine an upper limit of 1.4 nb/sr for the cross section for the formation of the nuclear stable trineutron in the center-of-mass system. This value is much smaller than the estimate of 70 nb/sr (center-of-mass system) obtained in [22], where the same reaction was studied for an angle of $\theta_{\text{ls}} = 7.4^\circ$ and a beam energy of 79.6 MeV, which is close to the beam energy in our experiment. Thus, neither quasi-stationary nor resonance states with widths $\Gamma \leq 3$ MeV in the system of three neutrons are found in the spectrum of ${}^{11}\text{C}$ nuclei from the ${}^7\text{Li}({}^7\text{Li}, {}^{11}\text{C})3n$ reaction at an angle of 2° up to an excitation energy of 30 MeV.

The spectrum of ${}^{10}\text{C}$ nuclei from the $({}^7\text{Li}, {}^{10}\text{C})$ reaction is well reproduced by five-particle phase space for the ${}^{10}\text{C} + 4n$ system under the assumption of noninteracting neutrons (the solid line in Fig. 2). We emphasize that the total yield of ${}^{10}\text{C}$ nuclei is an order of magnitude higher than that obtained in the measurements at an angle of 10° [16]. Events detected in the region of the zero binding energy of the tetraneutron correspond to an upper limit of 0.1 nb/sr for the cross section for the formation of bound or quasi-stationary states of the tetraneutron in the center-of-mass system. This value is a record for the reaction under investigation. Previously, this reaction was studied with the use of the standard $\Delta E-E$ and $E-t$ procedures in [16, 22], where estimates of 2 and 30 nb/sr, respectively, were obtained.

In connection with reports on the discovery of the nuclear stable tetraneutron in the reactions of the fragmentation of ${}^{14}\text{Be}$ and ${}^8\text{He}$ radioactive beams [18, 19], we estimate the cross section for the formation of a four-neutron cluster in the ${}^7\text{Li}({}^7\text{Li}, {}^{10}\text{C})4n$ reaction with the use of the distorted wave method assuming the

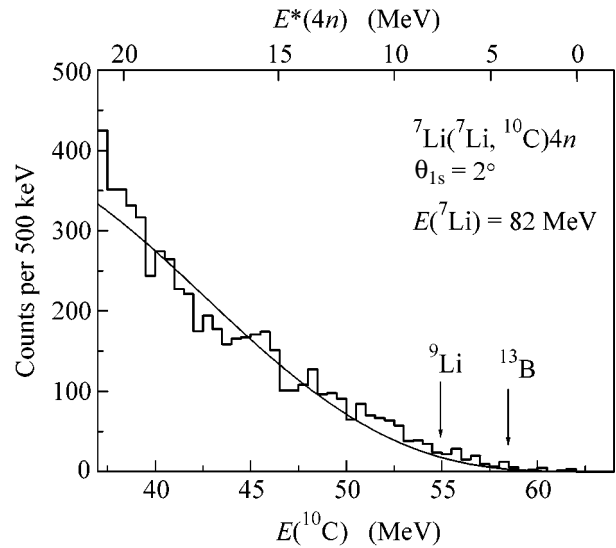


Fig. 2. Same as in Fig. 1, but for the $({}^7\text{Li}, {}^{10}\text{C})4n$ reaction.

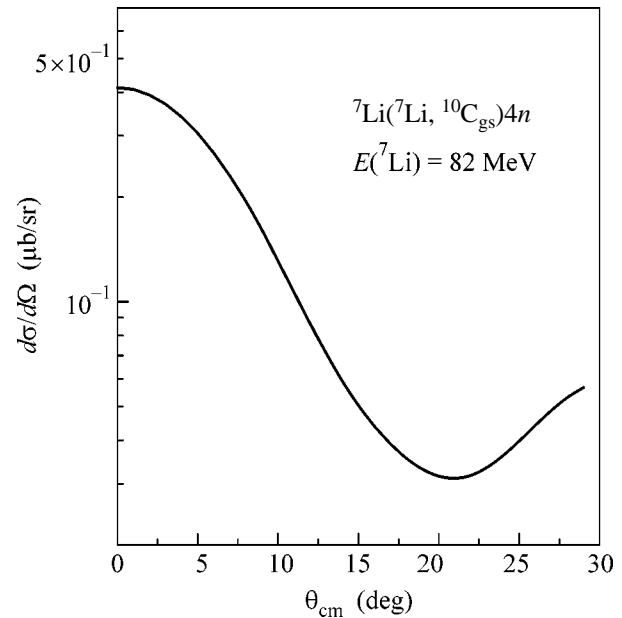


Fig. 3. Angular distribution for the ${}^7\text{Li}({}^7\text{Li}, {}^{10}\text{C})4n$ reaction as calculated by the distorted-wave method.

mechanism of the pick-up of three protons by the ${}^7\text{Li}$ nucleus ($\Delta L = 0$). The wave functions of the bound states of the three-proton cluster in the ${}^7\text{Li}$ and ${}^{10}\text{C}$ nuclei are calculated with the Woods-Saxon potentials with a radius of $R = 2.1$ and 2.3 fm, respectively, and a diffusivity of 0.65 fm. Distortions in the input and output channels are calculated with the optical potentials found from analysis of elastic scattering in the systems ${}^7\text{Li} + {}^6\text{Li}$ [23] and ${}^{12}\text{C} + \alpha$ [24]. The spectroscopic factors for ${}^7\text{Li}(3p + 4n)$ and ${}^{10}\text{C}({}^7\text{Li} + 4n)$ are set to unity. Figure 3 shows the results of the calculation performed

with the DWUCK5 code. As is seen in this figure, the cross section for the formation of the tetraneutron at small angles may be equal to 400 nb/sr. The small value is explained by the strong endothermic effect of the reaction ($Q = -18.17$ MeV) and by the high momentum transfer (0.85 fm^{-1} at 0°) that gives rise to the kinematic suppression of transitions with the orbital angular momentum transfer $\Delta L = 0$. The value obtained above should be considered only as an upper limit. First, the spectroscopic factors entering into the expression for the cross section are evidently smaller than unity. Second, the nuclear stable tetraneutrons must have a low binding energy and large sizes. As was mentioned in [1], the emission of such a tetraneutron is suppressed compared to the usual cross sections by a factor of about $F = (\varepsilon/E)^{9/2}$, where ε is the tetraneutron binding energy and $E = \hbar^2/2mr^2 \sim 1$ MeV is the characteristic energy corresponding to the reaction radius. Therefore, the calculated cross section may be an order of magnitude smaller. Thus, the upper limit obtained above for the cross section for the formation of the nuclear stable tetraneutron apparently indicates that this tetraneutron is absent.

4. CONCLUSIONS

In this work, nuclear stable and quasi-stationary states, as well as resonances, were searched for in the $3n$ and $4n$ systems. To this end, the energy spectra of the ${}^7\text{Li}({}^7\text{Li}, {}^{11}\text{C})3n$ and ${}^7\text{Li}({}^7\text{Li}, {}^{10}\text{C})4n$ reactions have been measured for $E({}^7\text{Li}) = 82$ MeV and $\theta_{\text{ls}} = 2^\circ$ up to multineutron excitation energies 20–30 MeV. These investigations have considerable advantages over experiments with radioactive beams due both to the high intensity of stable nuclear beams (incomparable with the intensities of radioactive beams) and to the sufficiently large expected cross sections for the reactions. The combination of the magnetic separator with the $\Delta E-E$ and $E-t$ procedures enabled us (i) to carry out measurements near 0° , to increase the beam intensity without an increase in the load of the electronics, and to thereby improve the statistical accuracy of the measured spectra; (ii) to ensure the reliable separation of carbon isotopes; and (iii) to reduce the random-coincidence background.

As a result, new upper limits have been obtained for the cross sections for the formation of nuclear stable $3n$ [$(d\sigma/d\Omega)_{\text{cm}} = 1.4$ nb/sr] and $4n$ [$(d\sigma/d\Omega)_{\text{cm}} = 0.1$ nb/sr] at small angles. The measured energy spectra are well described by four-particle (${}^{11}\text{C} + 3n$) and five-particle (${}^{10}\text{C} + 4n$) phase spaces. Quasi-stationary states in the systems of three and four neutrons have not been found even with the high sensitivity achieved in these measurements.

This work was supported by the Russian Foundation for Basic Research (project no. 04-02-16365).

REFERENCES

1. A. I. Baz', V. I. Gol'danskiĭ, V. Z. Gol'dberg, and Ya. B. Zeldovich, *Light and Intermediate Nuclei Near*

the Neutron Stability Boundary (Nauka, Moscow, 1972) [in Russian].

2. S. Fiarman and S. S. Hanna, *Nucl. Phys. A* **251**, 1 (1975).
3. A. A. Ogloblin and Yu. E. Penionzhkevich, in *Nuclei Far from Stability, Treatise on Heavy-Ion Science*, Ed. by D. A. Bromley (Plenum, New York, 1989), Vol. 8, p. 261.
4. J. Sperinde, D. Fredrickson, R. Hinkins, *et al.*, *Phys. Lett. B* **32**, 185 (1970).
5. L. Kaufman, V. Perez-Mendez, and J. Sperinde, *Phys. Rev.* **175**, 1358 (1968).
6. G. C. Phillips, *Phys. Lett. B* **33**, 260 (1970).
7. J. Cerny, R. B. Weisenmiller, N. A. Jelley, *et al.*, *Phys. Lett. B* **53**, 247 (1977).
8. D. V. Aleksandrov, Yu. A. Glukhov, E. Yu. Nikol'skiĭ, *et al.*, *Yad. Fiz.* **45**, 1217 (1987) [*Sov. J. Nucl. Phys.* **45**, 755 (1987)].
9. R. R. Warner, R. A. Patty, P. M. Voyles, *et al.*, *Phys. Rev. C* **54**, 1700 (1996).
10. R. R. Warner, M. H. McKinnon, N. C. Shaner, *et al.*, *Phys. Rev. C* **62**, 024608 (2000).
11. S. Fiarman and W. E. Meyerhof, *Nucl. Phys. A* **206**, 1 (1973).
12. D. R. Tilley and H. R. Weller, *Nucl. Phys. A* **541**, 1 (1992).
13. V. A. Ageev, I. N. Vishnevskii, V. I. Gavriilyuk, *et al.*, Preprint No. IYaI-85-4 (Inst. for Nuclear Research, Academy of Sciences of Ukraine, Kiev, 1985).
14. J. Schiffer and R. Vandenbosch, *Phys. Lett.* **5**, 292 (1963).
15. O. D. Brill, N. I. Venikov, A. A. Kurashov, *et al.*, *Phys. Lett.* **12**, 51 (1964).
16. D. V. Aleksandrov, Yu. A. Glukhov, E. Yu. Nikol'skiĭ, *et al.*, *Yad. Fiz.* **47**, 3 (1988) [*Sov. J. Nucl. Phys.* **47**, 1 (1988)].
17. A. V. Belozyorov, C. Borcea, Z. Dlouhy, *et al.*, *Nucl. Phys. A* **477**, 1273 (1988).
18. F. M. Marqués, M. Labiche, N. A. Orr, *et al.*, *Phys. Rev. C* **65**, 044 006 (2002).
19. V. Bouchat, F. M. Marqués, F. Hanappe, *et al.*, in *Proceedings of International Symposium on Exotic Nuclei (EXON-2004)* (Peterhof, Lake Ladoga, Russia, 2004), p. 52.
20. D. Beaumel, E. Becheva, Y. Blumenfeld, *et al.*, in *Proceedings of International Symposium on Exotic Nuclei (EXON-2004)* (Peterhof, Lake Ladoga, Russia, 2004), p. 53.
21. V. V. Buranov, N. I. Venikov, A. M. Dobyichin, *et al.*, Preprint No. 4816/2, IAE (Inst. of Atomic Energy, Moscow, 1989).
22. J. Cerny, in *Proceedings of the International Conference on Reaction between Complex Nuclei* (North-Holland, Amsterdam, 1974), Vol. 2, p. 483.
23. S. B. Sakuta, Yu. A. Glukhov, A. T. Rudchik, *et al.*, *Nucl. Phys. A* **587**, 355 (1995).
24. D. R. Ober and O. E. Johnson, *Phys. Rev.* **170**, 924 (1968).

Translated by R. Tyapaev

Exact Results on Spin Dynamics and Multiple Quantum NMR Dynamics in Alternating Spin-1/2 Chains with XY Hamiltonian at High Temperatures[†]

E. B. Fel'dman* and M. G. Rudavets

Institute of Problems of Chemical Physics, Russian Academy of Sciences, Chernogolovka, Moscow region, 142432 Russia

*e-mail: feldman@icp.ac.ru

Received December 7, 2004

We extend the picture of a transfer of nuclear spin-1/2 polarization along a homogeneous one-dimensional chain with the XY Hamiltonian to the inhomogeneous chain with alternating nearest neighbor couplings and alternating Larmor frequencies. To this end, we exactly calculate the spectrum of the spin-1/2 XY Hamiltonian of the alternating chain with an odd number of sites. The exact spectrum of the XY Hamiltonian is also applied to study the multiple quantum (MQ) NMR dynamics of the alternating spin-1/2 chain. MQ NMR spectra are shown to have the MQ coherences of zero and \pm second orders just as in the case of a homogeneous chain. The intensities of the MQ coherences are calculated. © 2005 Pleiades Publishing, Inc.

PACS numbers: 05.30.-d; 76.20.+q

1. INTRODUCTION

The discovery of the exact solution of spin-1/2 homogeneous one-dimensional chains with the XY Hamiltonian [1, 2] gives the observable and measurable features unraveling the NMR dynamics of spin-1/2 homogeneous one-dimensional chains [3]. Although most of the NMR experiments for one-dimensional spin chains appear to be well-explained by means of the nuclear spin dynamics on the homogeneous spin chains, NMR spin dynamics beyond the homogeneous chains has attracted the attention of researchers recently. For example, the experiments in [4] demonstrate the propagation of spin wave excitations along the inhomogeneous spin chains, and the mesoscopic echo has been observed [5] due to the reflections of the spin waves at the boundaries of the chain.

The paper presented is aimed at exploring the key differences of the NMR of the homogeneous spin-1/2 chain from the inhomogeneous spin-1/2 chain. It may be difficult, however, to calculate the NMR responses for an inhomogeneous spin chain with a random variation of the nearest neighbor (NN) dipolar coupling. Thus, as a first step to unravel the inhomogeneous effects, we treat the one-dimensional chain with an alternating spin-1/2 NN dipolar coupling and alternating Larmor frequencies.

In the approach in [1, 2], the basic tool in exploring the 1D spin-1/2 XY Hamiltonian is the Jordan–Wigner transformation of the original spin-1/2 XY Hamiltonian to the Hamiltonian of the free fermions. In this way, the exact thermodynamics for alternating infinite chains

with the spin-1/2 XY Hamiltonian were explored in [6]. In [7], the exact spectrum of the XY Hamiltonian with alternating couplings on the finite rings is presented. However, to our knowledge, the spectrum of the XY Hamiltonian with alternating couplings on the open chains is lacking now. This is what will be addressed in Section 2. The derived exact spectrum of the spin-1/2 XY Hamiltonian of the alternating open chains permits one to explain the transfer of the nuclear polarization along the alternating chains in Section 3 and to calculate the MQ intensities of the alternating spin-1/2 chains in Section 4. The concluding section, Section 5, draws a distinction between the NMR dynamics on alternating chains and those on homogeneous ones.

2. EXACT SPECTRUM OF THE SPIN-1/2 XY HAMILTONIAN WITH ALTERNATING COUPLINGS ON OPEN CHAINS

In this section, we derive the exact spectrum of the spin-1/2 XY Hamiltonian

$$H = \sum_{n=1}^N \omega_n I_{nz} + \sum_{n=1}^{N-1} D_{n,n+1} (I_{n,x} I_{n+1,x} + I_{n,y} I_{n+1,y}) \quad (1)$$

of the open chain of the odd number N of sites with the alternating NN coupling constants D_1 and D_2 and alternating Larmor frequencies ω_1 and ω_2 , see Fig. 1.

[†]This article was submitted by the authors in English.

The nuclear spins are specified by the spin-1/2 operators $I_{n\alpha}$ at the sites $n = 1, \dots, N$ with the projections $\alpha = x, y, z$. The Jordan–Wigner transformation [1]

$$I_{n,-} = I_{n,x} - iI_{n,y} = (-2)^{n-1} \left(\prod_{l=1}^{l=n-1} I_{l,z} \right) c_n,$$

$$I_{n,+} = I_{n,x} + iI_{n,y} = (-2)^{n-1} \left(\prod_{l=1}^{l=n-1} I_{l,z} \right) c_n^+, \quad (2)$$

$$I_{n,z} = c_n^+ c_n - 1/2,$$

from the spin-1/2 operators $I_{n\alpha}$ to the creation (annihilation) operators c_n^+ (c_n) of the spinless fermions takes the Hamiltonian (1) into the Hamiltonian

$$H = \sum_{n=1}^N \omega_n (c_n^+ c_n - 1/2) + \frac{1}{2} \sum_{n=1}^{N-1} D_{n,n+1} \{c_n^+ c_{n+1} + c_{n+1}^+ c_n\}, \quad (3)$$

or in the matrix notations as

$$H = \frac{1}{2} \mathbf{c}^+ (D + 2\Omega) \mathbf{c} - \frac{1}{2} \sum_{n=1}^N \omega_n. \quad (4)$$

In Eq. (4), we denote the row vector $\mathbf{c}^+ = (c_1^+, \dots, c_N^+)$, the column vector $\mathbf{c} = (c_1, \dots, c_N)^t$ (the superscript t represents the transpose), and specify the matrices Ω and D as

$$\Omega = \begin{bmatrix} \omega_1 & 0 & 0 & \dots & 0 & 0 \\ 0 & \omega_2 & 0 & \dots & 0 & 0 \\ 0 & 0 & \omega_1 & \dots & 0 & 0 \\ \vdots & \vdots & \vdots & \vdots & \vdots & \vdots \\ 0 & 0 & 0 & \dots & \omega_2 & 0 \\ 0 & 0 & 0 & \dots & 0 & \omega_1 \end{bmatrix}, \quad (5)$$

$$D = \begin{bmatrix} 0 & D_1 & 0 & \dots & 0 & 0 \\ D_1 & 0 & D_2 & \dots & 0 & 0 \\ 0 & D_2 & 0 & \dots & 0 & 0 \\ \vdots & \vdots & \vdots & \vdots & \vdots & \vdots \\ 0 & 0 & 0 & \dots & 0 & D_2 \\ 0 & 0 & 0 & \dots & D_2 & 0 \end{bmatrix}.$$

Diagonalization of the matrix $D + 2\Omega$ is performed by the unitary transformation

$$D + 2\Omega = U \Lambda U^+, \quad \Lambda = \text{diag}\{\lambda_1, \dots, \lambda_N\}, \quad (6)$$

so that the new fermion operators γ_k^+ and γ_k introduced by the relations

$$c_n^+ = \sum_{k=1}^N u_{n,k}^* \gamma_k^+, \quad c_n = \sum_{k=1}^N u_{n,k} \gamma_k \quad (7)$$

bring Hamiltonian (4) into the Hamiltonian

$$H = \frac{1}{2} \sum_{k=1}^N \lambda_k \gamma_k^+ \gamma_k - \frac{1}{2} \sum_{n=1}^N \omega_n \quad (8)$$

with energies $1/2\lambda_v$ of the free fermion waves.

To go further in the explicit calculations, it is necessary to find the eigenvalues λ_v and eigenvectors $|u_v\rangle = (u_{1v}, u_{2v}, \dots, u_{Nv})^t$ of the matrix $D + 2\Omega$,

$$(D + 2\Omega)|u_v\rangle = \lambda_v |u_v\rangle. \quad (9)$$

In Eq. (9), the components $u_{n,v}$ at the even sites $n = 2, 4, \dots, N-1$ obey the equations

$$D_1 u_{2k-1,v} + 2\omega_2 u_{2k,v} + D_2 u_{2k+1,v} = \lambda_v u_{2k,v}, \quad (10)$$

$$k = 1, 2, \dots, (N-1)/2.$$

We now fix the indices k and v in Eq. (10) and eliminate from Eq. (10) the components $u_{2k-1,v}$ and $u_{2k+1,v}$ at the odd sites $(2k-1)$ and $(2k+1)$ by writing down the equations for the $u_{2k-1,v}$, $u_{2k+1,v}$ from Eq. (9) as

$$D_2 u_{2k-2,v} + 2\omega_1 u_{2k-1,v} + D_1 u_{2k,v} = \lambda_v u_{2k-1,v}, \quad (11)$$

$$D_2 u_{2k,v} + 2\omega_1 u_{2k+1,v} + D_1 u_{2k+2,v} = \lambda_v u_{2k+1,v}.$$

Substituting (11) into (10), we get the relations for the amplitudes $u_{n,v}$ at the even sites,

$$g u_{2k-2,v} + g u_{2k+2,v} = u_{2k,v}, \quad (12)$$

$$k = 1, 2, \dots, (N-1)/2,$$

with the spatially independent coupling constant

$$g = \frac{D_1 D_2}{(\lambda_v - 2\omega_1)(\lambda_v - 2\omega_2) - D_1^2 - D_2^2}. \quad (13)$$

The derivation of (12), (13) is a characteristic approach in the theory of the real space renormalization [8], which eliminates the half of the degrees of freedom belonging to the odd sites yielding the field equations on the (even) lattice sites with doubled lattice constants. Equations (12) and (13) govern the amplitudes $u_{2,v}$, $u_{4,v}, \dots, u_{N-1,v}$ (including the amplitudes $u_{2,v}$, $u_{N-1,v}$ at the border sites 2 and $N-1$) if we introduce the additional sites $n = 0$ and $n = N+1$ and put there

$$u_{0,v} = 0, \quad u_{N+1,v} = 0. \quad (14)$$

Equation (14) implies cutting off the lattice at the sites 1 and N , thus, preventing the fermions from escaping

the lattice shown on Fig. 1. The solution of Eq. (12) conditioned by Eq. (14) reads

$$u_{2k,v} = A_v \sin\left(\frac{2\pi k v}{N+1}\right), \quad k, v = 1, 2, \dots, \frac{N-1}{2}, \quad (15)$$

with the eigenvalues

$$\lambda_v^{(\pm)} = \omega_1 + \omega_2 \pm \sqrt{(\omega_1 - \omega_2)^2 + D_1^2 \Delta_v},$$

$$v = 1, 2, \dots, \frac{N-1}{2}, \quad (16)$$

$$\Delta_v = 1 + 2\delta \cos\left(\frac{2\pi v}{N+1}\right) + \delta^2, \quad \delta = D_2/D_1.$$

Equation (16) gives $2[(N-1)/2] = N-1$ eigenvalues λ_v since for each index $v = 1, 2, \dots, N$ and for each superscript (+) and (-) the relationship $\lambda_v^{(\pm)} = \lambda_{N+1-v}^{(\pm)}$ holds. It is convenient to arrange $(N-1)$ distinct eigenvalues λ_v as

$$\lambda_v = \begin{cases} \lambda_v^{(+)}, & \text{for } v = 1, 2, \dots, (N-1)/2 \\ \lambda_v^{(-)}, & \text{for } v = (N+3)/2, (N+5)/2, \dots, N. \end{cases} \quad (17)$$

In accord with the enumeration of the eigenvalues λ_v in Eq. (17), the missed N th eigenvalue λ_v stands for the index $v = (N-1)/2 + 1 = (N+1)/2$ (recall that N is odd). To find the eigenvalue $\lambda_{(N+1)/2}$ and the eigenvector $u_{n, (N+1)/2}$ at the even sites n , use is made of the properties (see Eq. (15))

$$u_{n, (N+1)/2} = 0, \quad n = 0, 2, 4, \dots, N-1, N+1. \quad (18)$$

According to the condition $u_{N-1, (N+1)/2} = 0$, the N th equation from Eq. (9) immediately gives the sought eigenvalue

$$\lambda_{(N+1)/2} = 2\omega_1. \quad (19)$$

It remains to find the amplitudes $u_{k, (N+1)/2}$ at the odd sites. The sought amplitudes obey the relations

$$D_1 u_{2k-1, v} + D_2 u_{2k+1, v} = 0,$$

$$v = \frac{N+1}{2}, \quad k = 1, 2, \dots, \frac{N-1}{2}. \quad (20)$$

Equation (20) gives the components of the eigenvector $u_{n, (N+1)/2}$ belonging to the odd sites n (up to the normalization coefficient B),

$$u_{n, (N+1)/2} = B(-\delta)^{(N-n)/2}, \quad n = 1, 3, \dots, N. \quad (21)$$

Calculating the normalization coefficients A_v in Eq. (15) and the coefficient B in Eq. (21), one finds all

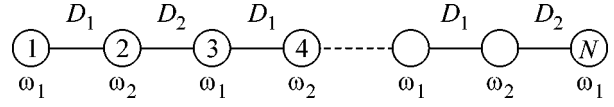


Fig. 1. An open chain of the odd number N of spins with the alternating NN coupling constants D_1 and D_2 and alternating Larmor frequencies ω_1, ω_2 .

the N eigenvectors $|u_v\rangle$ and all the N eigenvalues λ_v of Hamiltonian (8),

$$\lambda_v = \begin{cases} \omega_1 + \omega_2 + \sqrt{(\omega_1 - \omega_2)^2 + D_1^2 \Delta_v}, & v = 1, 2, \dots, \frac{N-1}{2} \\ 2\omega_1, & v = \frac{N+1}{2} \\ \omega_1 + \omega_2 - \sqrt{(\omega_1 - \omega_2)^2 + D_1^2 \Delta_v}, & v = \frac{N+3}{2}, \frac{N+5}{2}, \dots, N. \end{cases} \quad (22)$$

For all the indices $v = 1, \dots, N$ except the index $v = (N+1)/2$, the eigenvector $|u_v\rangle$ has the elements

$$u_{j,v} = \begin{cases} A_v \frac{D_1}{\lambda_v - 2\omega_1} \left[\delta \sin\left(\frac{\pi v(j-1)}{N+1}\right) + \sin\left(\frac{\pi v(j+1)}{N+1}\right) \right], & j = 1, 3, 5, \dots, N \\ A_v \sin\left(\frac{\pi v j}{N+1}\right), & j = 2, 4, \dots, N-1 \end{cases} \quad (23)$$

and the normalization coefficient

$$A_v = \frac{2|\lambda_v - 2\omega_1|}{\sqrt{N+1}} \frac{1}{\sqrt{(\lambda_v - 2\omega_1)^2 + D_1^2 \Delta_v}}. \quad (24)$$

By Eq. (21), the elements of the eigenvector $|u_{(N+1)/2}\rangle$ read

$$u_{j, (N+1)/2} = \begin{cases} B(-\delta)^{(N-j)/2}, & j = 1, 3, 5, \dots, N \\ 0, & j = 2, 4, \dots, N-1 \end{cases} \quad (25)$$

with the normalization coefficient

$$B = \left(\frac{\delta^2 - 1}{\delta^{N+1} - 1} \right)^{1/2}. \quad (26)$$

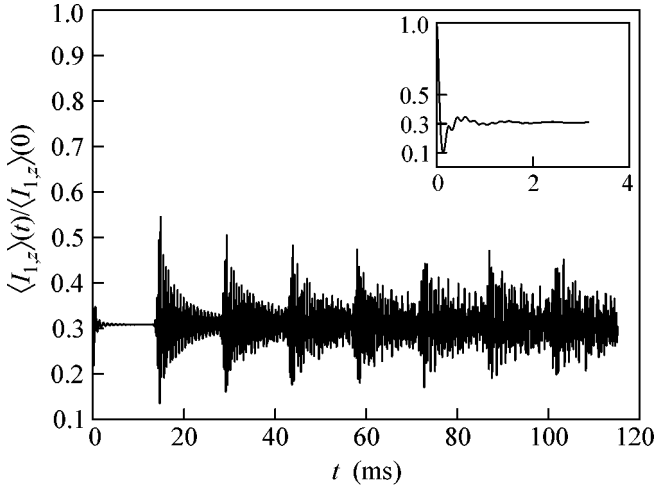


Fig. 2. Time course of the polarization $\langle I_{1,z} \rangle(t) / \langle I_{1,z} \rangle(0)$ of the first spin (Eq. (30)) for the chain of 201 spins interacting with the coupling coefficients $D_1 = 2\pi \cdot 4444 \text{ s}^{-1}$ and $D_2 = 2\pi \cdot 6666 \text{ s}^{-1}$ and equal Larmor frequencies. The initial polarization is on the first spin. The inset shows the time course of the polarization on an earlier time interval $0 \leq t < 4 \text{ ms}$.

3. SPIN-WAVE PROPAGATION IN OPEN CHAINS WITH ALTERNATING COUPLINGS

The spectrum of Eqs. (22)–(26) of the XY Hamiltonian (8) can now be applied to describe how the polarization at a single site of the alternating chain with equal Larmor frequencies ω_n changes over the time.

Let the initial polarization be on the single site j ; hence, the spin dependent part of the initial density matrix at the high temperature approximation is (see [9])

$$\rho(0) = I_{j,z} = c_j^+ c_j - 1/2. \quad (27)$$

Given the initial density matrix (27) and the Hamiltonian H (8), the Liouville–von Neumann equation ($\hbar = 1$)

$$i \frac{\partial \rho}{\partial t} = [H, \rho], \quad (28)$$

is solved in terms of the fermion operators (7) as follows:

$$\begin{aligned} \rho(t) &= e^{-iHt} I_{j,z} e^{iHt} \\ &= -\frac{1}{2} + \sum_{1 \leq l, m \leq N} u_{j,l}^* u_{j,m} e^{-\frac{i}{2}(\lambda_l - \lambda_m)t} \Upsilon_l^+ \Upsilon_m. \end{aligned} \quad (29)$$

Denoting the polarization at the j 'th spin at the time moment t by $\langle I_{j,z} \rangle(t)$ and invoking Eq. (27), we get

$$\frac{\langle I_{j,z} \rangle(t)}{\langle I_{j,z} \rangle(0)} = \frac{\text{tr}\{\rho(t) I_{j,z}\}}{\text{tr}\{I_{j,z}^2\}} = \left| \sum_{1 \leq \nu \leq N} u_{j,\nu}^* u_{j,\nu} e^{-\frac{i}{2}\lambda_\nu t} \right|^2. \quad (30)$$

Figure 2 shows the time course of the polarization $\langle I_{1,z} \rangle(t) / \langle I_{1,z} \rangle(0)$ at the site $j = 1$ when the initial polarization is also at site 1 and $D_2 = \frac{3}{2} D_1$. Just as in the case

of the polarization dynamics on the homogeneous chain with equal couplings, $D_2 = D_1$, [3] the dynamics of the polarization of the alternating chain can be regarded as the propagation of the spin wave packet starting at site 1 and bouncing back and forth at the chain ends. To calculate the return time t_R for the wave packet to reappear at site 1, we first determine the group velocity of the waves described by the Hamiltonian H (8) with the dispersion law $1/2\lambda_\nu$ (16) and the equal Larmor frequencies $\omega_1 = \omega_2$. By specifying the wave vector $p = 2\pi\nu/(N+1)$, $\nu = 1, 2, \dots, (N-1)/2$, the dispersion law of Eq. (16) written down as $\frac{1}{2}\lambda_\nu =$

$\frac{1}{2} D_1 \sqrt{1 + 2\delta \cos(p) + \delta^2}$ allows one to calculate the sought group velocity

$$v = \max_p \left\{ a \frac{d\lambda(p)}{2dp} \right\} = \frac{aD_1}{2}, \quad (31)$$

where a is the lattice constant and the coupling constant D_1 is the minimal coupling constant among the two coupling constants D_1 and D_2 . Thus, for $N = 201$ -chain with the coupling constants $D_1 = 2\pi \cdot 4444 \text{ s}^{-1}$ and $D_2 = 2\pi \cdot 6666 \text{ s}^{-1}$, the time of the first returning of the wave packet to site 1 becomes (see Fig. 2)

$$t_R = \frac{2(N-1)}{D_1} \approx 14.5 \text{ ms}. \quad (32)$$

The traveling waves of the spin polarization $\langle I_{j,z} \rangle(t) / \langle I_{1,z} \rangle(0)$ are shown in Fig. 3.

4. INTENSITIES OF MQ COHERENCES IN OPEN CHAINS WITH ALTERNATING COUPLINGS

The exact spectrum of Eqs. (22)–(26) of the Hamiltonian H (8) provides us with a technique for determining the multiquantum dynamics in an alternating open chain. Again, we take the initial density matrix $\rho(0)$ (27) and calculate how the MQ coherences develop in the spin system of the alternating spin-1/2 chain. The MQ NMR dynamics of the nuclear spins coupled by the nearest neighbor dipolar interactions are described by the Hamiltonian [10, 11]

$$H_{\text{MQ}} = \frac{1}{2} \sum_{n=1}^{N-1} D_{n,n+1} \{ I_{n,+} I_{n+1,+} + I_{n,-} I_{n+1,-} \}. \quad (33)$$

The Hamiltonian H (33) takes the form of the exactly solvable Hamiltonian H (1) (with the Larmor frequen-

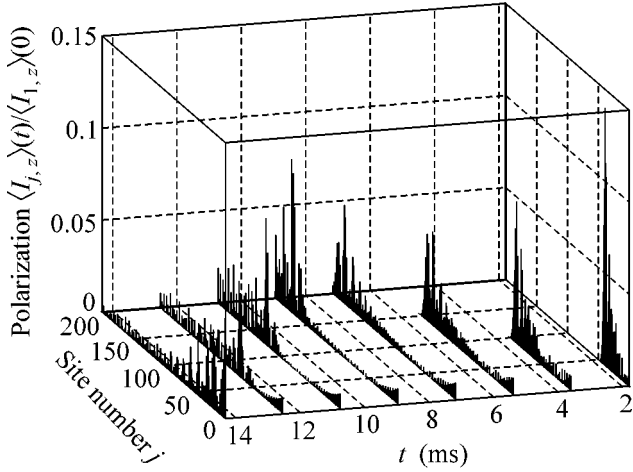


Fig. 3. Propagation of the spin-wave packet along the 201-site open chain. The packet starts at the boundary site $j = 1$.

cies $\omega_n = 0$ for all the sites) by making use of the unitary transformation [11] acting on the even sites

$$Y = \exp(-i\pi I_{2,x}) \exp(-i\pi I_{4,x}) \dots \exp(-i\pi I_{N-1,x}), \quad (34)$$

so that $YH_{\text{MQ}}Y^+ = H$ (Eq. (1); $\{\omega_n = 0\}$). In addition, the transformation Y brings the initial density matrix (27) to the form

$$\bar{\rho}(0) = YI_zY^+ = \sum_{n=1}^N (-1)^{n-1} I_{n,z}, \quad (35)$$

where we introduce the total polarization $I_z = \sum_{n=1}^N I_{n,z}$. The Liouville–von Neumann Eq. (28) with the Hamiltonian H (33) and the initial density matrix (27) gives the intensities $G_n(t)$ of $n = 0$ and $n = \pm 2$ orders, just as in the case of the homogeneous chain with the conservation condition [11, 12]

$$G_0(t) + G_2(t) + G_{-2}(t) = 1, \quad (36)$$

and

$$\begin{aligned} G_0(t) &= \frac{1}{N} \sum_{n=1}^N \cos^2(\lambda_n t), \\ G_{\pm 2}(t) &= \frac{1}{2N} \sum_{n=1}^N \sin^2(\lambda_n t). \end{aligned} \quad (37)$$

Figure 4 demonstrates the development of the 2Q coherence on the alternating $N = 201$ -chain with the couplings $D_1 = 2\pi \cdot 4444 \text{ s}^{-1}$ and $D_2 = 2\pi \cdot 6666 \text{ s}^{-1}$; thus, $\delta = D_2/D_1 = 1.5$. As time proceeds, the regular course of the intensities $G_{\pm 2}(t)$ is transformed to the erratic temporary behavior just as in the case of the homogeneous lattice with $D_1 = D_2$ [13]. For $D_1 = D_2$,

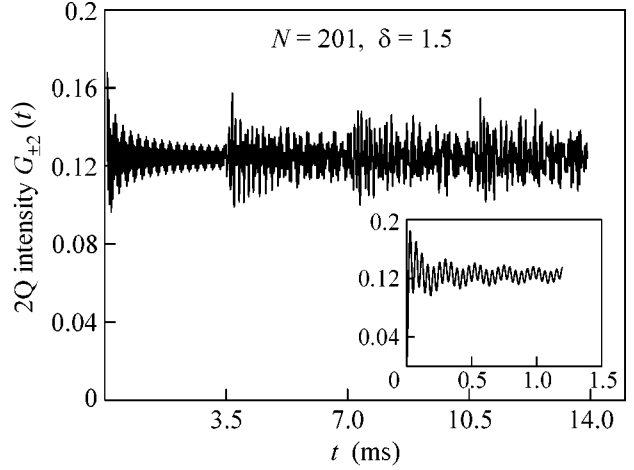


Fig. 4. Time course of the intensities of the 2Q coherence (Eq. (37)) in the chain of $N = 201$ spins interacting with the coupling constants $D_1 = 2\pi \cdot 4444 \text{ s}^{-1}$ and $D_2 = 2\pi \cdot 6666 \text{ s}^{-1}$ and zero Larmor frequencies. The insert shows an early development of 2Q coherence over the times $t < 1.5$ ms.

Eq. (37) exactly reproduces the results for the intensities of the 2Q coherence of [11].

5. CONCLUSIONS

The sensitivity of the NMR spin polarization dynamics to the spatially periodic short-distance inhomogeneity of the lattice was explored in the previous sections relying on the exact spectrum of the spin-1/2 XY Hamiltonian on the alternating open chain with an odd number of sites.

If the spin polarization is prepared initially on the single site, the spin dynamics on the nonhomogeneous lattice are represented as the propagation of the spin wave packet. The velocity of the wave packet on the nonhomogeneous lattice is controlled by the minimal coupling constant $\min\{D_1, D_2\}$. In the extreme situation $D_1 \ll D_2$ ($D_1, D_2 \neq 0$), the spin polarization stays fixed on the initial site.

As time proceeds, the regular spin propagation along the alternating chain is transformed to the erratic one.

The time scale of the regular behavior of the 2Q intensities $G_{\pm 2}(t)$ is 4 times shorter than the time scale of the regular behavior of the polarization $\langle I_{j,z} \rangle(t) / \langle I_{1,z} \rangle(0)$, as can be seen by a comparison of Fig. 4 with Fig. 2. The same effect occurs in the case of the spin dynamics on the homogeneous chain [13]. The effect is caused by two reasons. First, the velocity of the propagation of the 2Q coherence is doubled as compared with the velocity of the propagation of the spin polarization, as is obvious from the comparison of the dispersion law in Eq. (37) with the dispersion law in Eq. (30). Secondly, the two-spin local excitations of the 2Q coherence travel the path N before the two-spin

excitations return back on the N -site chain. The path N should be compared with the path $2N$ traveled by the single local spin excitation before it reappears on the initial site of the chain.

ACKNOWLEDGMENTS

The authors thank A.A. Belavin, O.V. Derzhko, S.I. Doronin, A.I. Smirnov, and M.A. Yurishchev for discussions of the problems involved, as well as I.I. Maksimov for support in preparing the manuscript. This work was supported by the Russian Foundation for Basic Research (project no. 04-03-32528).

REFERENCES

1. E. Lieb, T. Schultz, and D. Mattis, *Ann. Phys. (N.Y.)* **16**, 407 (1969).
2. H. B. Cruz and L. L. Gonsalves, *J. Phys. C* **14**, 2785 (1981).
3. E. B. Fel'dman, R. Brüschweiler, and R. R. Ernst, *Chem. Phys. Lett.* **294**, 297 (1998).
4. Z. L. Madi, B. Brutscher, T. Schulte-Herbrüggen, *et al.*, *Chem. Phys. Lett.* **268**, 300 (1997).
5. H. M. Pastawski, P. R. Levstein, and G. Usaj, *Phys. Rev. Lett.* **75**, 4310 (1995).
6. O. Derzhko and J. Richter, *Phys. Rev. B* **55**, 14298 (1997).
7. F. Ye, G.-H. Ding, and B.-W. Xu, cond-mat/0105584.
8. J. Machta, *Phys. Rev. B* **24**, 5260 (1981); R. B. Stinchcomb, *J. Phys. A* **18**, L591 (1985).
9. A. Abragam, *The Principles of Nuclear Magnetism* (Clarendon, Oxford, 1961; Inostrannaya Literatura, Moscow, 1963).
10. J. Baum, M. Munowitz, A. N. Garroway, and A. Pines, *J. Chem. Phys.* **83**, 2015 (1985).
11. S. I. Doronin, I. I. Maksimov, and E. B. Fel'dman, *JETP* **91**, 597 (2000).
12. D. A. Lathrop, E. S. Handy, and K. K. Gleason, *J. Magn. Reson. A* **111**, 161 (1994).
13. S. I. Doronin, E. B. Fel'dman, and S. Lacelle, *Chem. Phys. Lett.* **353**, 226 (2002).

Real-Time Instantons and Suppression of Collision-Induced Tunneling[¶]

D. Levkov^{1,2} and S. Sibiryakov¹

¹ Institute for Nuclear Research, Russian Academy of Sciences, Moscow, 117312 Russia
e-mail: levkov@ms2.inr.ac.ru

² Department of Physics, Moscow State University, Moscow, 119899 Russia
Received December 22, 2004

We consider tunneling processes in QFT induced by collisions of elementary particles. We propose a semiclassical method for estimating the probability of these processes in the limit of very high collision energy. As an illustration, we evaluate the maximum probability of induced tunneling between different vacua in a $(1+1)$ -dimensional scalar model with boundary interaction. © 2005 Pleiades Publishing, Inc.

PACS numbers: 03.65.Sq; 03.70.+k; and 11.15.Kc

In many models of field theory one encounters tunneling transitions between states separated by an energy barrier of finite height E_s . The famous examples are false vacuum decay in scalar theories [1] and topology-changing transitions in gauge–Higgs theory [2, 3]. In the weak coupling regime, the rate of tunneling at zero energy is exponentially small [1, 2], but one suspects the suppression to vanish once energy exceeding the height of the barrier is injected into the system. A particular way of inducing the tunneling process is a collision of two highly energetic particles. It was conjectured some time ago [4] that the collision-induced tunneling processes may become unsuppressed at high collision energies. Semiclassical study of scalar and gauge–Higgs theories [5, 6] showed, however, that this is not the case: the tunneling probability remains exponentially small even if the collision energy E considerably exceeds the barrier height E_s . Furthermore, analyses of toy models [7, 8] and unitarity arguments [9] suggest that the collision-induced transitions should remain exponentially suppressed even if E tends to infinity. In other words, it was proposed that (contrary to the initial conjecture) the probability of the process has the form

$$\mathcal{P}(E) \propto e^{-F(E)/g^2}, \quad (1)$$

where g^2 is a small coupling constant and the suppression exponent $F(E)$ remains positive at all energies. This has been confirmed recently by direct calculation [10] of the suppression exponent in the whole range of energies in a toy two-dimensional model. In addition, it was found in [10] that the suppression exponent reaches its minimum F_m at a certain optimal energy E_o and remains constant above this energy

$$F(E) = F_m, \quad E > E_o. \quad (2)$$

One may ask whether or not the formulas (1), (2) are valid for other models with model-dependent values of F_m , E_o .

In this letter, we give a general semiclassical method for evaluating the minimum value F_m of the suppression exponent and the energy E_o at which this minimum is achieved. Our procedure is essentially an adaptation of the method of [11], but it is more straightforward and technically simpler. We consider the case in which, after the appropriate rescaling of the fields, the action S takes the form $S = \tilde{S}/g^2$, where \tilde{S} does not explicitly depend on the small coupling constant g . One observes that g^2 effectively plays the role of the Planck constant, and the limit $g \rightarrow 0$, which we consider below, corresponds to a semiclassical situation.

Our starting point is the inclusive probability of tunneling from states with a given number of incoming particles and any energy

$$\mathcal{P}_m(N) = \sum_{i,f} |\langle f | \hat{\mathcal{U}}(T_f, T_i) \hat{P}_N | i \rangle|^2. \quad (3)$$

Here $\hat{\mathcal{U}}(T_f, T_i)$ is the evolution operator, and \hat{P}_N denotes the projector onto states with N particles. The initial and final states, $|i\rangle$ and $|f\rangle$, respectively, are at different sides of the potential barrier. Here and below the limit, $T_f \rightarrow +\infty$, $T_i \rightarrow -\infty$ is assumed. As we will shortly see, the quantity (3) can be evaluated semiclassically provided the initial number of particles is parametrically large, $N = \tilde{N}/g^2$. We will see that the result has a typical exponential form,

$$\mathcal{P}_m(N) \propto e^{-F_m(\tilde{N})/g^2}. \quad (4)$$

[¶]This article was submitted by the authors in English.

We use the result (4) as a source of information on the probability of collision-induced tunneling. It is clear that the inclusive multiparticle probability $\mathcal{P}_m(N)$ sets an upper bound on the two-particle probability of interest, $\mathcal{P}(E)$, at arbitrarily high energies E . Indeed, the energy of the initial state in (3) can be arbitrarily high, while any initial two-particle state can be promoted to the multiparticle one by adding a number of ‘‘spectator’’ particles that do not interfere with the tunneling process. Hence, the exponential suppression of $\mathcal{P}_m(N)$ entails the exponential suppression of $\mathcal{P}(E)$, and the inequality

$$F_m(\tilde{N}) \leq F_m \quad (5)$$

holds. Following [11], we conjecture that

$$\lim_{\tilde{N} \rightarrow 0} F_m(\tilde{N}) = F_m. \quad (6)$$

The conjecture (6) is based on the observation that, in the leading semiclassical approximation, the probability of tunneling does not depend on the details of the initial state provided the initial number of particles is much smaller than $1/g^2$. The analogs of the formula (6) have been checked in various situations [12–14].

Now, we proceed to the semiclassical evaluation of the multiparticle exponent $F_m(\tilde{N})$. Our strategy is to represent the inclusive probability $\mathcal{P}_m(N)$ in the form of a path integral and evaluate the latter making use of the saddle-point technique. Taking into account that $\hat{P}_N \cdot \hat{P}_N = \hat{P}_N$, one recasts Eq. (3) in the form

$$\begin{aligned} \mathcal{P}_m(N) &= \sum_{i, i', f} \langle f | \hat{\mathcal{U}} | i' \rangle \langle i' | \hat{P}_N | i \rangle \langle i | \hat{\mathcal{U}} | f \rangle \\ &= \int \mathcal{D}[\phi_f, a, a^*, b, b^*] e^{-\frac{1}{g^2} \int d\mathbf{k} [a_{\mathbf{k}} a_{\mathbf{k}}^* + b_{\mathbf{k}} b_{\mathbf{k}}^*]} \\ &\quad \times \langle \phi_f | \hat{\mathcal{U}} | a \rangle \langle a | \hat{P}_N | b \rangle [\langle \phi_f | \hat{\mathcal{U}} | b \rangle]^*, \end{aligned} \quad (7)$$

where $|\phi_f\rangle$ are eigenstates of the field operators, which we denote collectively by $\hat{\phi}$, while $|a\rangle, |b\rangle$ are the coherent states

$$\hat{\phi}(\mathbf{x})|a\rangle = \frac{\phi(\mathbf{x})}{g}|a\rangle, \quad \hat{a}_{\mathbf{k}}|a\rangle = \frac{a_{\mathbf{k}}}{g}|a\rangle.$$

Hereafter, we use the shorthand notation $\hat{\mathcal{U}} \equiv \hat{\mathcal{U}}(T_f, T_i)$. Making use of the standard path integral for the transition amplitude in the ϕ representation, one writes

$$\langle \phi_f | \hat{\mathcal{U}} | a \rangle = \int_{\phi(T_f) = \phi_f} \mathcal{D}\phi \exp \left\{ \frac{1}{g^2} (i\tilde{S}[\phi] + B_i(\phi_i, a)) \right\}, \quad (8)$$

where the boundary term B_i comes from the initial matrix element $\langle \phi | a \rangle$,

$$\begin{aligned} B_i(\phi_i, a) \\ = \int d\mathbf{k} \left\{ -\frac{1}{2} a_{\mathbf{k}} a_{-\mathbf{k}} - \frac{\omega_{\mathbf{k}}}{2} \phi_i(\mathbf{k}) \phi_i(-\mathbf{k}) + \sqrt{2\omega_{\mathbf{k}}} a_{\mathbf{k}} \phi_i(\mathbf{k}) \right\}. \end{aligned}$$

In this expression, $\phi_i(\mathbf{k})$ stands for the spatial Fourier transform of the fields at $t = T_i$. For the matrix element of the projector \hat{P}_N one obtains (see e.g., [15, 16])

$$\langle a | \hat{P}_N | b \rangle = \int_{-i\infty}^{i\infty} d\theta \exp \left\{ \frac{1}{g^2} (\tilde{N}\theta + \int d\mathbf{k} a_{\mathbf{k}}^* b_{\mathbf{k}} e^{-\theta}) \right\}. \quad (9)$$

Substituting Eqs. (8) and (9) into expression (7) and performing integration over the variables b, b^* , one obtains the desired path integral representation

$$\mathcal{P}_m(N) = \int_{\phi(T_f) = \phi'(T_f)} \mathcal{D}[\phi, \phi', a, a^*] d\theta e^{-F/g^2}, \quad (10)$$

where

$$\begin{aligned} F &= -\tilde{N}\theta - i\tilde{S}[\phi] + i\tilde{S}[\phi'] \\ &\quad - B_i(\phi_i, a) - B_i^*(\phi'_i, a) + \int d\mathbf{k} a_{\mathbf{k}}^* a_{\mathbf{k}} e^{\theta}. \end{aligned} \quad (11)$$

Note that the integration over ϕ' in (10) comes from the path integral representation for the complex conjugate amplitude $[\langle \phi_f | \hat{\mathcal{U}} | b \rangle]^*$.

The functional F defined in Eq. (11) is independent of the coupling constant g . Hence, at weak coupling, the integral (10) is saturated by its saddle point. The saddle-point equations are as follows. Extremization with respect to ϕ and ϕ' gives the classical field equations

$$\frac{\delta \tilde{S}}{\delta \phi} = \frac{\delta \tilde{S}}{\delta \phi'} = 0. \quad (12a)$$

The boundary conditions for these equations are obtained by varying the expression (11) with respect to the initial and final values of the fields. Using the relation $\delta S / \delta \phi(T_f, \mathbf{x}) = \dot{\phi}(T_f, \mathbf{x})$ and taking into account the constraint (see. Eq. (10))

$$\phi(T_f, \mathbf{x}) = \phi'(T_f, \mathbf{x}), \quad (12b)$$

one obtains

$$\dot{\phi}(T_f, \mathbf{x}) = \dot{\phi}'(T_f, \mathbf{x}). \quad (12c)$$

In the initial asymptotic region $T_i \rightarrow -\infty$, the evolution of the fields ϕ, ϕ' is linear and one writes¹

¹ For concreteness we assume that the initial state is an excitation above the vacuum $\phi = 0$.

$$\phi_i = \int \frac{d\mathbf{k}}{(2\pi)^{1/2} \sqrt{2\omega_{\mathbf{k}}}} (f_{\mathbf{k}} e^{-i\omega_{\mathbf{k}} T_i} + g_{-\mathbf{k}}^* e^{i\omega_{\mathbf{k}} T_i}) e^{i\mathbf{k}\mathbf{x}},$$

$$\phi_i' = \int \frac{d\mathbf{k}}{(2\pi)^{1/2} \sqrt{2\omega_{\mathbf{k}}}} (f_{\mathbf{k}}' e^{-i\omega_{\mathbf{k}} T_i} + g_{-\mathbf{k}}'^* e^{i\omega_{\mathbf{k}} T_i}) e^{i\mathbf{k}\mathbf{x}}.$$

The variation of the functional F with respect to ϕ_i , ϕ_i' , a , a^* yields the following relations between the frequency components:

$$f_{\mathbf{k}}' = f_{\mathbf{k}} e^{\theta}, \quad g_{-\mathbf{k}}'^* = g_{-\mathbf{k}}^* e^{-\theta}. \quad (12d)$$

The set of saddle-point equations (12) can be simplified if we recall that the configurations ϕ and ϕ' saturate the amplitude and its complex conjugate, respectively. This suggests the Ansatz equation $\phi'(t, \mathbf{x}) = [\phi(t, \mathbf{x})]^*$, which is compatible with the boundary value problem (12) provided the saddle-point value of θ is real. Then, the boundary value problem is formulated in terms of a single set of fields $\phi(t, \mathbf{x})$. The conditions (12b), (12c) imply the reality of the fields in the asymptotic future

$$\text{Im}\phi(t, \mathbf{x}) \longrightarrow 0, \quad \text{Im}\dot{\phi}(t, \mathbf{x}) \longrightarrow 0 \quad \text{as } t \longrightarrow +\infty, \quad (13a)$$

while Eqs. (12d) read

$$f_{\mathbf{k}} = e^{-\theta} g_{\mathbf{k}}. \quad (13b)$$

The boundary condition in the asymptotic past, Eq. (13b), can be understood as follows. In the limit $\theta \longrightarrow +\infty$, it coincides with the Feynman boundary condition and thus corresponds to the initial state with a semiclassically small number of particles $\tilde{N} \longrightarrow 0$; finite θ picks up the most favorable state with nonzero \tilde{N} .

The number of equations in the boundary value problem (12a), (13) is equal to the number of unknowns. Generically, for a given value of θ , this problem has a unique solution $\phi_{rr}(t, \mathbf{x})$. We call this solution a ‘‘real-time instanton,’’ as it lives on the real time axis, in contrast to the ordinary instanton, which is defined in Euclidean time. Note that the boundary condition (13b) implies that the real-time instanton is complex-valued. On the other hand, its imaginary part should vanish in the asymptotic future due to condition (13a). Let us discuss the consequences of this property. Assume that, at large (but finite) times, the solution gets linearized about some real static configuration, $\phi_{rr}(t, \mathbf{x}) = \phi_s(\mathbf{x}) + \delta\phi(t, \mathbf{x})$. Then, Eq. (12a) implies that $\text{Im}\delta\phi \longrightarrow 0$ as $t \longrightarrow +\infty$. This amounts to requiring that the configuration ϕ_s is unstable; consequently, $\text{Im}\delta\phi$ evolves along its negative mode, $\text{Im}\delta\phi \propto e^{-\text{const} \cdot t}$. The natural candidate for $\phi_s(\mathbf{x})$ is the static solution ‘‘sitting’’ on top of the potential barrier separating the sectors of the initial and final states. Accepting the terminology of

gauge–Higgs theories [3], we call this solution ‘‘sphaleron.’’²

We arrive at the conclusion that the real-time instantons describe the formation of the sphaleron as $t \longrightarrow +\infty$. This is, in fact, a common property of solutions relevant for collision-induced tunneling at energies higher than E_S [14, 6, 10]. The transition is completed by the decay of the sphaleron into the states of interest, which proceeds with probability of order one.

The last saddle-point equation obtained by varying the functional (11) with respect to the parameter θ relates the value of θ to the initial number of particles,

$$\tilde{N} = \int d\mathbf{k} f_{\mathbf{k}} g_{\mathbf{k}}^*. \quad (14)$$

Substituting the solution into Eq. (11), one obtains the formula (4) with the suppression exponent

$$F_m(\tilde{N}) = -\tilde{N}\theta + 2\text{Im} \left\{ \tilde{S}[\phi_{rr}] + \frac{1}{2} \int d\mathbf{x} \phi_{rr} \dot{\phi}_{rr} \Big|_{t=T_i} \right\}. \quad (15)$$

Note that the term in braces is the action of the real-time instanton integrated by parts with respect to time.

At finite value of the parameter θ (the nonzero value of \tilde{N}), the real-time instanton is by construction a smooth solution to the equations of motion and has a well-defined classical energy $E_o(\tilde{N})$. At $t \longrightarrow +\infty$, the real-time instanton describes semiclassical evolution in the final state. Thus, $E_o(\tilde{N})$ coincides with the energy of the final state saturating the probability (3). This means that, if we restrict the sum in (3) to the states with the *fixed* energy $E = E_o(\tilde{N})$ (cf. [11]), we obtain the same result (4). One concludes that $E_o(\tilde{N})$ is the optimal energy for tunneling from the states with the given number of particles $N = \tilde{N}/g^2$. The limit

$$E_o = \lim_{\tilde{N} \rightarrow 0} E_o(\tilde{N}) \quad (16)$$

determines the optimal energy for collision-induced tunneling.³ It is easy to understand the most favorable transition at higher energies. The system releases the energy excess $(E - E_o)$ by a perturbative emission of a few particles (which costs only a power suppression in g^2) and tunnels at the optimal energy E_o [7, 10]. Due to this process, $F(E)$ stays constant at $E > E_o$, i.e., formula (2) holds.

Let us illustrate our method by considering a simple example. We consider a free massless scalar field $\phi(t, x)$ living in (1 + 1) dimensions on a half-line $x > 0$ with

² In the case of scalar theories, such a solution is known as a ‘‘critical bubble’’ [1].

³ In general, we cannot exclude the situation when $E_o(\tilde{N}) \longrightarrow \infty$ as $\tilde{N} \longrightarrow 0$. In the example below, E_o is finite.

self-interaction localized at the boundary point $x = 0$. The action of the model is⁴

$$S = \frac{1}{g^2} \int dt \left\{ \frac{1}{2} \int_0^\infty dx (\partial_\mu \phi)^2 - \mu [1 - \cos(\phi(t, 0))] \right\}, \quad (17)$$

where the parameter μ sets the characteristic energy scale of the boundary interaction. Model (17) is used in solid state physics to describe the transport in quantum wires [17] and Josephson chains with defects [18]. A detailed semiclassical treatment of model (17) is given in [10].

Model (17) has a number of vacua $\phi_n = 2\pi n$, $n = 0, \pm 1, \dots$, which are separated by the potential barriers of the height $E_S = 2\mu/g^2$ determined by the maximum of the boundary potential. One also finds an unstable static solution $\phi_s = \pi$, sphaleron, which ‘‘sits’’ on the top of the ‘‘first’’ potential barrier. The process we are interested in is the tunneling between the vacua $\phi = 0$ and $\phi = 2\pi$ induced by highly energetic particle scattering off the boundary. To calculate the minimum suppression exponent and the optimal energy of this collision-induced tunneling process, one finds the family of real-time instantons by solving the boundary value problem (12a), (13).

Since the bulk evolution of $\phi(t, x)$ is that of a free massless scalar field, we represent the general solution in the form

$$\phi(t, x) = \varphi_{\text{in}}(t+x) + \varphi_{\text{out}}(t-x), \quad (18)$$

where φ_{in} and φ_{out} are the incoming and outgoing waves. The boundary interaction leads to the nonlinear equation at $x = 0$,

$$\partial_x \phi = \mu \sin \phi, \quad x = 0. \quad (19)$$

Due to condition (13a), the outgoing wave φ_{out} is real. Introducing the real and imaginary parts of the incoming wave, $\varphi_{\text{in}}(\xi) = a(\xi) + ib(\xi)$, one rewrites Eq. (19) as a set of two real equations

$$b' = \mu \sinh b \cos u, \quad (20)$$

$$u' = 2a' - \mu \cosh b \sin u, \quad (21)$$

where $u(\xi) = a(\xi) + \varphi_{\text{out}}(\xi)$. The remaining conditions in the asymptotic past, Eq. (13b), should be imposed on the frequency components of the incoming wave φ_{in} . To this end, one performs a Fourier expansion of φ_{in} ,

$$\varphi_{\text{in}}(t+x) = \int dk \varphi_{\text{in}}(k) e^{ik(t+x)}, \quad (22)$$

and finds that the positive and negative frequency components of the solution, f_{-k} and g_{-k}^* , are proportional to $\varphi_{\text{in}}(-k)$ and $\varphi_{\text{in}}(k)$, $k > 0$, respectively. Thus, Eq. (13b)

⁴ Normally, one should use some infrared regularization for the massless scalar model in $(1+1)$ dimensions. However, the specifics of the regularization turn out to be irrelevant for our purposes.

takes the form $\varphi_{\text{in}}(-k) = e^{-\theta} [\varphi_{\text{in}}(k)]^*$, where $k > 0$. It is straightforward to check using the Cauchy formula that the latter condition is equivalent in its turn to the following relation between the real and imaginary parts of the initial wave (see [10])

$$a'(\xi) = \frac{1 + e^{-\theta}}{1 - e^{-\theta}} \frac{1}{\pi \xi} \mathcal{P} \int d\xi_1 \frac{\xi_1 b'(\xi_1)}{\xi_1 - \xi}, \quad (23)$$

where the integral is understood in the sense of principal value. We use Eq. (23) as an alternative formulation of condition (13b) in our model.

It is also required that the functions φ_{in} , φ_{out} have appropriate asymptotics. To ensure a finite number of particles in the initial state, we require the incoming wave to be well localized, $\varphi_{\text{in}}(\xi) \rightarrow 0$ as $\xi \rightarrow \pm\infty$. In addition, as the initial state is an excitation above the vacuum $\phi = 0$, we write $\varphi_{\text{out}}(\xi) \rightarrow 0$ at $\xi \rightarrow -\infty$. On the other hand, as we have already discussed, the relevant solution contains the sphaleron at $t \rightarrow +\infty$. Thus, $\varphi_{\text{out}}(\xi) \rightarrow \pi$ as $\xi \rightarrow +\infty$.

Problem (20), (21), (23) can be solved numerically by the following iterative method. At each cycle of iterations, one starts from the function⁵ $u = u^{(0)}(\xi)$ and solves Eq. (20) explicitly

$$b(\xi) = \ln \tanh \left(-\frac{\mu}{2} \int_0^\xi \cos u^{(0)}(\xi_1) d\xi_1 + \kappa \right), \quad (24)$$

where κ is an integration constant. Then, integrating numerically Eqs. (23), (21), one finds $a(\xi)$ and $u(\xi)$ for a given value of κ . Finally, one picks up the value of κ such that the function $u(\xi)$ has correct asymptotics as $\xi \rightarrow \pm\infty$. In this way, the improved approximation for $u(\xi)$ is obtained and a new cycle of iterations begins. After 30 cycles, one obtains the solution with precision of order 10^{-6} .

Given the family of real-time instantons, one calculates numerically the suppression exponent $F_m(\theta)$ via Eq. (15) and also the energy $E_o(\theta)$. To calculate the number of particles, it is convenient to recast Eq. (14) in the form

$$\tilde{N} \equiv g^2 N = -\frac{2}{\sinh \theta} \int d\xi a'(\xi) b(\xi). \quad (25)$$

The functions $F_m(\theta)$, $E_o(\theta)$, and $\tilde{N}(\theta)$ determine the dependence of the suppression exponent and the energy on \tilde{N} . These are plotted in Fig. 1. Taking the limit $\tilde{N} \rightarrow 0$, one obtains $F_m = 10.27$, $E_o = 2.65E_S$. Thus, the semiclassical suppression factor is $\exp(-10.27/g^2)$ at all energies exceeding $E_o = 2.65E_S$, and the suppression is even stronger at lower energies.

⁵ At the very first cycle, one takes, e.g., $u^{(0)}(\xi) = \pi/2 + \arctan(\mu\xi)$.

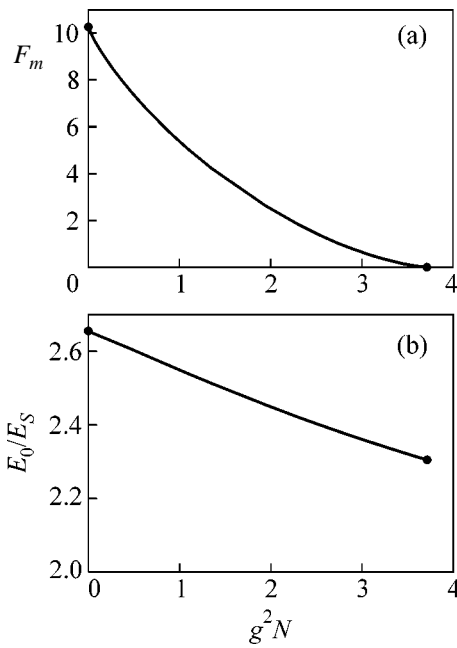


Fig. 1. Suppression exponent (a) and energy of real-time instantons (b) versus the number of incoming particles in the model (17).

In conclusion, we summarize our method. To calculate the minimum suppression exponent F_m and the optimal energy E_o of a collision-induced tunneling process, one finds the family of complex classical solutions and real-time instantons satisfying boundary conditions (13). Given the real-time instantons, one calculates the number of particles \tilde{N} ; the suppression exponent $F_m(\tilde{N})$; Eqs. (14), (15); and the energy $E_o(\tilde{N})$. By itself, the quantity $F_m(\tilde{N})$ provides the lower bound on F_m , Eq. (5); the limit $\tilde{N} \rightarrow 0$ yields F_m and E_o according to Eqs. (6), (16).

ACKNOWLEDGMENTS

We are grateful to S. Dubovsky, V. Rubakov, P. Tinyakov, and F. Bezrukov for helpful suggestions. This work was supported in part by the Russian Foundation

for Basic Research (project nos. 02-02-17398 and NS-2184.2003.2) and by fellowships of the ‘‘Dynasty’’ foundation (awarded by the Scientific Board of ICFPM). The work of D.L. was supported by the CRDF (award no. RPI-2364-MO-02) and INTAS (grant no. YS03-55-2362). D.L. is grateful to the Universite Libre de Bruxelles for hospitality.

REFERENCES

1. S. R. Coleman, Phys. Rev. D **15**, 2929 (1977); **16**, 1248(E) (1977); *Lecture Delivered at 1977 International School of Subnuclear Physics* (Erice, Italy, 1977), HUTP-78/A004.
2. A. A. Belavin, A. M. Polyakov, A. S. Schwartz, and Y. S. Tyupkin, Phys. Lett. B **59**, 85 (1975).
3. N. S. Manton, Phys. Rev. D **28**, 2019 (1983); F. R. Klinkhamer and N. S. Manton, Phys. Rev. D **30**, 2212 (1984).
4. A. Ringwald, Nucl. Phys. B **330**, 1 (1990); O. Espinosa, Nucl. Phys. B **343**, 310 (1990).
5. A. N. Kuznetsov and P. G. Tinyakov, Phys. Rev. D **56**, 1156 (1997).
6. F. Bezrukov, D. Levkov, C. Rebbi, *et al.*, Phys. Rev. D **68**, 036005 (2003); Phys. Lett. B **574**, 75 (2003).
7. M. B. Voloshin, Phys. Rev. D **49**, 2014 (1994).
8. V. A. Rubakov and D. T. Son, Nucl. Phys. B **424**, 55 (1994).
9. V. I. Zakharov, Nucl. Phys. B **353**, 683 (1991); G. Veneziano, Mod. Phys. Lett. A **7**, 1661 (1992); M. Maggiore and M. A. Shifman, Nucl. Phys. B **371**, 177 (1992).
10. D. G. Levkov and S. M. Sibiryakov, hep-th/0410198.
11. V. A. Rubakov, D. T. Son, and P. G. Tinyakov, Phys. Lett. B **287**, 342 (1992).
12. P. G. Tinyakov, Phys. Lett. B **284**, 410 (1992); A. H. Mueller, Nucl. Phys. B **401**, 93 (1993).
13. G. F. Bonini, A. G. Cohen, C. Rebbi, and V. A. Rubakov, Phys. Rev. D **60**, 076004 (1999).
14. F. Bezrukov and D. Levkov, Zh. Éksp. Teor. Fiz. **125**, 938 (2004) [JETP **98**, 820 (2004)].
15. P. G. Tinyakov, Int. J. Mod. Phys. A **8**, 1823 (1993).
16. C. Rebbi and R. J. Singleton, hep-ph/9706424.
17. C. L. Kane and M. P. A. Fisher, Phys. Rev. Lett. **68**, 1220 (1992).
18. R. Fazio, K. H. Wagenblast, C. Winkelholz, and G. Schön, Physica B (Amsterdam) **222**, 364 (1996).

Self-Compression of Subgigawatt Femtosecond Laser Pulses in a Hollow Photonic-Crystal Fiber

S. O. Konorov¹, E. E. Serebryannikov¹, A. A. Ivanov², D. A. Akimov¹,
M. V. Alfimov², M. Scalora³, and A. M. Zheltikov^{1,4}

¹ Faculty of Physics, Moscow State University, Vorob'evy gory, 119992 Moscow, Russia

² Center of Photochemistry, Russian Academy of Sciences, ul. Novatorov 7a, 117421 Moscow, Russia

³ AMCOM Research Office, Huntsville, AL 35898-5000, USA

⁴ International Laser Center, Moscow State University, Vorob'evy gory, 119992 Moscow, Russia

e-mail: zheltikov@phys.msu.ru

Received November 30, 2004; in final form, December 8, 2004

We report experimental evidence of waveguide self-compression for high-power Cr: forsterite-laser femtosecond pulses in a hollow photonic-crystal fiber. Dispersion spreading typical of low-intensity laser pulses is replaced by nonuniform compression for pulses with high power (above 100 MW) with the compression efficiency reaching its maximum around the peak of the laser pulse. © 2005 Pleiades Publishing, Inc.

PACS numbers: 42.65.Wi; 42.81.Qb

Transmission and control of high-power ultrashort laser pulses are the key problems of high-field physics and laser technologies. Self-focusing and optical breakdown limit the use of standard optical fibers for these applications. Hollow fibers with a solid cladding [1] radically enhance nonlinear-optical interactions [2], allowing the formation of ultrashort light pulses [3, 4] and providing high efficiencies of high-order harmonic generation [5, 6]. Such fibers are, however, intrinsically multimode and offer only limiting options for broadband dispersion control.

Hollow-core photonic-crystal fibers (PCFs) [7–9] can support isolated truly guided modes of high-power laser radiation [10], thus, suggesting unique possibilities of dispersion tailoring [8]. Recent experiments demonstrate that hollow PCFs substantially enhance a broad class of nonlinear-optical processes, including stimulated Raman scattering [11], off-resonance four-wave mixing [12, 13], coherent anti-Stokes Raman scattering [14], and self-phase modulation [15]. Temporal and spatial self-action of high-power laser pulses in hollow PCFs gives rise to temporal solitons [16, 17] and self-channeling of laser radiation [18]—interesting new propagation regimes of ultrashort intense-field pulses.

Earlier studies [19] revealed the high potential of hollow PCFs for linear compression of prechirped high-power laser pulses, allowing the creation of all-fiber-optic chirped-pulse amplifiers. The idea of this work is to use a gas-filled hollow PCF to integrate a nonlinear-optical phase modulator and a chirp compensator with a special dispersion profile. Our experiments on the temporal self-action of multimewatt femtosec-

ond Cr: forsterite-laser pulses in a hollow PCF indicate guided-wave self-compression of laser pulses of this class.

The hollow-core PCFs designed for the transmission and nonlinear-optical transformation of high-power ultrashort laser pulses had a period of the photonic-crystal cladding of about 5 μm and a core diameter of approximately 50 μm (Fig. 1). The basic waveguiding properties of such fibers have been discussed elsewhere [20]. The transmission spectra of these fibers dis-

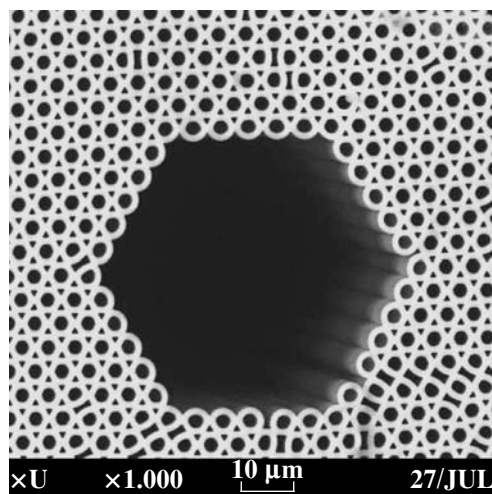


Fig. 1. An SEM cross-section image of the hollow photonic-crystal fiber.

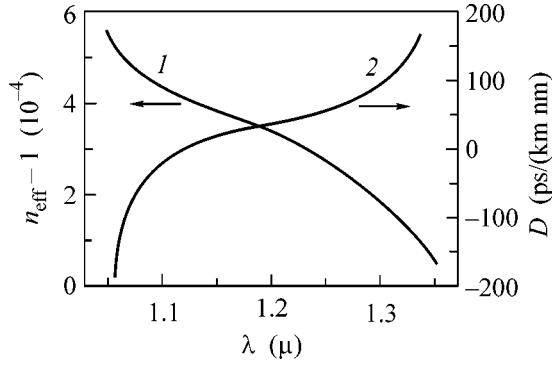


Fig. 2. The effective mode index $n_{\text{eff}} - 1$ and the group-velocity dispersion D as functions of the radiation wavelength for the fundamental mode of the hollow PCF with the cross-section structure shown in Fig. 1.

play characteristic well-pronounced isolated passbands, which are related to the photonic band gaps of the periodically structured cladding. The passbands in the PCF transmission were tuned by changing the structure of the fiber cladding [21].

To model the guided modes and transmission spectra of hollow PCFs, we numerically solved the wave equations for the transverse components of the electric field using a modification of the technique developed by Poladian *et al.* [22]. We consider a waveguide where a central cylindrical part with a radius R and a complicated refractive index profile is surrounded by a solid uniform cladding with the refractive index n_{cl} . The two-dimensional refractive index profile $n(r, \varphi)$ in cylindrical coordinates r and φ in the central part of the structure is represented as an expansion in polynomials and periodic functions in such a way as to provide the best fit for the hollow core and the photonic-crystal cladding of the PCF (examples of such expansions can be found in [13, 23]). The wave equations for the transverse components $\psi = \psi(r, \varphi)$ of the electromagnetic field are written as

$$\frac{\partial^2 \psi}{\partial r^2} + \frac{1}{r} \frac{\partial \psi}{\partial r} + \frac{1}{r^2} \frac{\partial^2 \psi}{\partial \varphi^2} + V^2(r, \varphi) \psi = W^2 \psi, \quad (1)$$

where $V^2(r, \varphi) = k^2 R^2 (n^2(r, \varphi) - n_{\text{cl}}^2)$, k is the wave number, $W^2 = k^2 R^2 (n_{\text{eff}}^2 - n_{\text{cl}}^2)$, $n_{\text{eff}} = \beta/k$ is the effective mode index, and β is the propagation constant for the waveguide mode defined as an eigenvalue of Eq. (1).

Inside the central cylindrical domain with the radius R , the field is represented, according to Poladian *et al.* [22], as an expansion

$$\psi(r, \varphi) = \sum_{mn} A_{mn} \Psi_{mn}(r, \varphi) \quad (2)$$

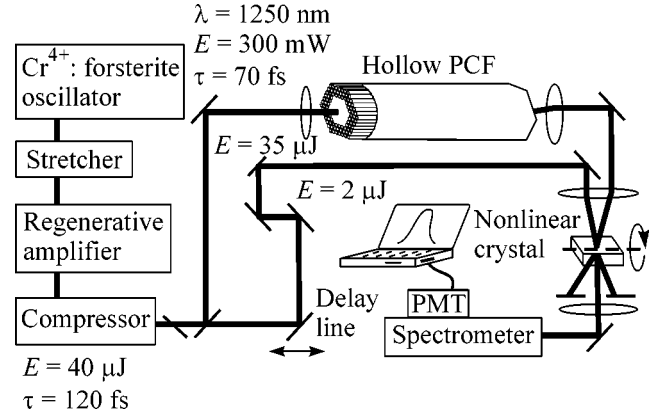


Fig. 3. Diagram of the experimental setup.

in the set of basis functions

$$\Psi_{mn}(r, \varphi) = e^{im\varphi} \left(\frac{\sin(n\pi r)}{\pi r} + \alpha_{mn}(W) + \beta_{mn}(W)r \right), \quad (3)$$

where

$$\alpha_{mn}(W) = n\delta_{m,0} \left(1 + K_0(W) \frac{(-1)^n - 1}{WK'_0(W)} \right), \quad (4)$$

$$\beta_{mn}(W) = n \left(-\delta_{m,0} + (1 - \delta_{m,0}) K_m(W) \frac{(-1)^n}{WK'_m(W) - K_m(W)} \right), \quad (5)$$

and $K_m(x)$ is the modified Bessel function of the m th order.

Outside the inner domain with the radius R , the solution to Eq. (1) is represented as

$$\psi(r, \varphi) = \sum_m B_m e^{im\varphi} K_m(Wr). \quad (6)$$

Substitution of Eqs. (2) and (6) into Eq. (1) yields an eigenfunction and eigenvalue problem for a matrix equation with eigenfunctions and eigenvalues identified as field intensity profiles and propagation constants of waveguide modes, respectively.

The group-velocity dispersion (GVD) $D = -2\pi c \lambda^{-2} d^2 \beta / d\omega^2$ (where β is the propagation constant of the waveguide mode; λ and ω are the radiation wavelength and frequency, respectively; and c is the speed of light) is the key parameter of a fiber controlling the pulse lengthening rate for ultrashort light-field waveforms. Lines 1 and 2 in Fig. 2 represent the effective mode index $n_{\text{eff}} - 1$ and the GVD as functions of the radiation wavelength for the fundamental mode of a hollow PCF with the cross-section structure shown in Fig. 1. The results of the calculations presented in Fig. 2 show that the hollow PCF designed for this study provides anomalous GVD ($D > 0$) within a broad spec-

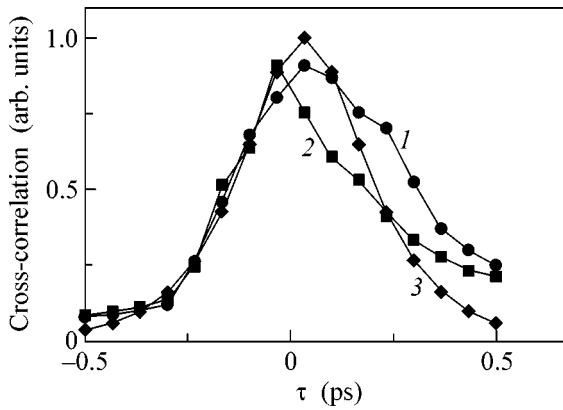


Fig. 4. Cross-correlation traces for Cr: forsterite-laser pulses at the output of the hollow PCF (1, 2) and at the output of the laser system (3). The energy of the laser pulse at the input of the PCF is (1) 50 nJ and (2) 35 μ J.

tral range, including the fundamental wavelength of Cr: forsterite-laser radiation (1.25 μ m). Such a fiber allows self-compression of Cr: forsterite-laser pulses due to the GVD compensation of the chirp of these pulses induced by self-phase modulation in the hollow-core of the PCF filled with a gas having a nonlinear refractive index $n_2 > 0$.

The laser system employed in our experiments (Fig. 3) consisted of a Cr⁴⁺: forsterite master oscillator, a stretcher, an optical isolator, a regenerative amplifier, a compressor, and a crystal for frequency doubling. The master oscillator, pumped with a fiber ytterbium laser, generated 50–70-fs light pulses with a repetition rate of 120 MHz, a central wavelength of 1250 nm, and a mean power of about 300 mW. These pulses were then transmitted through a stretcher and an isolator to be amplified in an Nd: YLF-laser-pumped amplifier. Amplified pulses with an energy up to 100 μ J were recompressed to a 100–200-fs pulse duration in a grating compressor. Approximately 50% of the radiation energy was lost at this stage.

A cross-correlation technique was used to measure the temporal envelope and the duration of the laser pulses transmitted through the hollow PCF. The signal coming out of the PCF was mixed with a fundamental-wavelength reference Cr: forsterite-laser pulse in a BBO crystal with a thickness of about 1 mm (Fig. 3). The resulting sum-frequency signal was measured as a function of the delay time between the signal and the reference pulse to give the cross-correlation trace.

A standard micro-objective served to couple the amplified Cr: forsterite-laser pulses into a hollow PCF filled with atmospheric air and placed on a three-dimensional translation stage. Beam coupling was optimized to provide the maximum efficiency of the fundamental-mode excitation in the PCF. The input laser pulses had an initial duration of about 270 fs (curve 3 in Fig. 4) and energy ranging from 10 nJ up to 50 μ J.

The results of the cross-correlation measurements are presented in Fig. 4. In the regime of low intensities, the laser pulses increase their pulse width as they propagate through the PCF. Pulses with an initial duration of about 270 fs and an energy of 50 nJ lengthen up to approximately 350 fs as they reach the output of the fiber with a length of 9 cm (curve 1 in Fig. 4). The high-intensity laser pulses experience self-phase modulation due to the Kerr nonlinearity of the gas filling the hollow core of the PCF. The characteristic length for this nonlinear-optical process L_{nl} is determined by the nonlinear coefficient $\gamma = n_2\omega/cS_{eff}$, where S_{eff} is the effective area of the waveguide mode, and the power of the laser pulse P : $L_{nl} = (\gamma P)^{-1}$. For laser pulses of 1.25- μ m radiation with an initial duration of 270 fs and an energy of 35 μ J, the characteristic length of the self-phase modulation in a hollow PCF filled with atmospheric air at the pressure $p = 1$ atm ($n_2 \approx 5 \times 10^{-19}$ cm²/W), $L_{nl} \approx 6.3$ cm, is less than the chosen PCF length. The optical nonlinearity of the gas in the fiber core under these conditions gives rise to a noticeable chirp of the laser pulse.

In the regime of anomalous dispersion provided by the hollow PCF, laser pulses experience nonuniform frequency deviation and their duration decreases. A typical duration of a laser pulse with a power $P \approx 130$ MW at the output of the PCF is about 210 fs (curve 2 in Fig. 4). High-order dispersion noticeably distorts the output pulse. Comparison of curves 1 and 2 in Fig. 4 shows that the highest efficiency of the pulse compression is achieved around the peak of the laser pulse, where the laser intensity reaches its maximum. Off the laser pulse peak, the radiation intensity is lower and the optical nonlinearity is smaller. As a result, the pulse edges virtually coincide for low- and high-intensity pulses (see Fig. 4). A further increase in the input energy of the laser pulses gave rise to a considerable distortion of the output pulses. This tendency can be attributed to the ionization nonlinearity of the gas filling the fiber core, as well as to the solitonic effects.

The experiments presented in this paper show that hollow PCFs with a special dispersion profile can efficiently control the duration and the waveform of high-power ultrashort laser pulses. We have experimentally demonstrated a waveguide self-compression of ultrashort pulses with a power exceeding 100 MW. We expect that dispersion optimization of hollow PCFs, extended to include high-order dispersion terms, multi-soliton interactions, and ionization nonlinearity, should allow the creation of efficient fiber-optic compressors and transmission lines for high-power ultrashort laser pulses.

We are grateful to A.V. Shcherbakov and L.A. Mel'nikov for the fabrication of waveguide structures and A.B. Fedotov and D.A. Sidorov-Biryukov for their help and useful discussions. This study was supported in part by the Grant of the President of the Russian Federation (grant no. MD-42.2003.02), the Russian Foundation for Basic Research (project nos. 03-02-16929,

03-02-20002-BNTS, 04-02-39002-GFEN2004, and 04-02-81036-Bel2004), and INTAS (grant nos. 03-51-5037 and 03-51-5288). The research described in this publication was made possible in part by Award no. RP2-2558 of the U.S. Civilian Research & Development Foundation for the Independent States of the Former Soviet Union (CRDF). This material is also based upon work supported by the European Research Office of the US Army under Contract No. 62558-04-P-6043.

REFERENCES

1. E. A. J. Marcatili and R. A. Schmelzter, *Bell Syst. Tech. J.* **43**, 1783 (1964).
2. A. M. Zheltikov, *Usp. Fiz. Nauk* **172**, 743 (2002) [*Phys. Usp.* **45**, 687 (2002)].
3. M. Nisoli, S. De Silvestri, and O. Svelto, *Appl. Phys. Lett.* **68**, 2793 (1996).
4. N. Zhavoronkov and G. Korn, *Phys. Rev. Lett.* **88**, 203901 (2002).
5. E. Constant, D. Garzella, P. Breger, *et al.*, *Phys. Rev. Lett.* **82**, 1668 (1999).
6. A. Paul, R. A. Bartels, R. Tobey, *et al.*, *Nature* **421**, 51 (2003).
7. R. F. Cregan, B. J. Mangan, J. C. Knight, *et al.*, *Science* **285**, 1537 (1999).
8. P. St. J. Russell, *Science* **299**, 358 (2003).
9. C. M. Smith, N. Venkataraman, M. T. Gallagher, *et al.*, *Nature* **424**, 657 (2003).
10. A. M. Zheltikov, *Usp. Fiz. Nauk* **174**, 1301 (2004) [*Phys. Usp.* **47** (12) (2004) (in press)].
11. F. Benabid, J. C. Knight, G. Antonopoulos, and P. St. J. Russell, *Science* **298**, 399 (2002).
12. S. O. Konorov, A. B. Fedotov, and A. M. Zheltikov, *Opt. Lett.* **28**, 1448 (2003).
13. S. O. Konorov, E. E. Serebryannikov, D. A. Akimov, *et al.*, *Phys. Rev. E* (in press).
14. A. B. Fedotov, S. O. Konorov, V. P. Mitrokhin, *et al.*, *Phys. Rev. A* **70**, 045802 (2004).
15. S. O. Konorov, D. A. Sidorov-Biryukov, I. Bugar, *et al.*, *Phys. Rev. A* **70**, 023807 (2004).
16. D. G. Ouzounov, F. R. Ahmad, D. Muller, *et al.*, *Science* **301**, 1702 (2003).
17. F. Luan, J. C. Knight, P. St. J. Russell, *et al.*, *Opt. Express* **12**, 835 (2004).
18. S. O. Konorov, A. M. Zheltikov, Ping Zhou, *et al.*, *Opt. Lett.* **29**, 1521 (2004).
19. J. Limpert, T. Schreiber, S. Nolte, *et al.*, *Opt. Express* **11**, 3332 (2003).
20. S. O. Konorov, A. B. Fedotov, L. A. Mel'nikov, *et al.*, *Laser Phys. Lett.* **1**, 548 (2004).
21. A. M. Zheltikov, *Optics of Microstructure Fibers* (Nauka, Moscow, 2004) [in Russian].
22. L. Poladian, N. A. Issa, and T. M. Monroe, *Opt. Express* **10**, 449 (2002).
23. E. E. Serebryannikov, D. von der Linde, and A. M. Zheltikov, *Phys. Rev. E* **70**, 061412 (2004).

Translated by A. Zheltikov

Photoluminescence Kinetics of Wurtzite GaN Quantum Dots in an AlN Matrix

D. D. Ri¹, V. G. Mansurov¹, A. Yu. Nikitin¹, A. K. Gutakovskii¹,
K. S. Zhuravlev¹, and P. Tronc²

¹ *Institute of Semiconductor Physics, Siberian Division, Russian Academy of Sciences, Novosibirsk, 630090 Russia*
e-mail: redim@gorodok.net

² *Laboratoire d'Optique Physique, Ecole Supérieure de Physique et Chimie Industrielles, 75005 Paris, France*
Received December 7, 2004

The photoluminescence (PL) of GaN quantum dots in an AlN matrix is studied. It is found that the maximum of the PL line does not shift when the laser excitation power varies. The transient PL spectra indicate that the quenching kinetics is nonexponential and the quenching law depends on the spectral range. The experimental data are explained in the framework of a model taking into account the strong built-in electric field in wurtzite structures and the transport of charge carriers between them. © 2005 Pleiades Publishing, Inc.

PACS numbers: 78.55.Cr; 78.67.Hc

In recent years, quantum wells (QWs) and quantum dots (QDs) based on group III nitrides have been intensively studied. The structures grown in the wurtzite phase are of special interest. This is due to the occurrence of a built-in electric field along the (0001) axis induced by the spontaneous and piezoelectric polarization of the QW (or QD) material and the barrier. The values of the electric field strength reported in the literature for GaN QDs in an AlN matrix vary from 3.8 MV/cm [1] to 7 MV/cm [2]. Such a strong field substantially affects the optical properties of structures with QDs.

The main manifestation of the internal electric field is the quantum dimensional Stark effect: the energy of the recombination emission is less than the bandgap energy of bulk unstrained GaN in large-size QDs (the height of the dots is larger than 3 nm at the average field of 5 MV/cm [3]). The energy of dimensional quantization in small-size QDs is sufficiently large; therefore, the energy of recombination emission exceeds the bandgap energy of bulk GaN. As a result, the energy of recombination emission varies in a wide range from 2.3 to 4.2 eV upon variation of the QD sizes [3–6]. Moreover, oppositely charged carriers are spatially separated by the electric field, resulting in an increase in their lifetime.

Screening the built-in electric field with nonequilibrium charge carriers can change the QD energy spectrum and hence the spectrum of the emitted light and the lifetime of the nonequilibrium charge carriers [3]. The theoretical calculations performed in [1] demonstrate that the screening of the built-in electric field by two pairs of free charge carriers leads to a shift of the GaN/AlN QD photoluminescence (PL) line by several tens of millielectronvolts. The line shift of the transient

PL of QDs found experimentally at room temperature [7] and at liquid helium temperature [8] makes up almost 1 eV. As far as we know, this energy shift is the largest for semiconductors and semiconductor structures. It is evident that such a large shift cannot be explained only by the screening of the built-in electric field. Estimates show that each QD must contain several tens of electron–hole pairs for the observed shift to be provided by the screening of the electric field; this will inevitably cause fast (from 0.1 to 1 ns) Auger recombination. However, the PL shift is observed within several milliseconds after the excitation pulse.

In this work, the steady-state and transient PL of QDs was studied to elucidate the mechanisms determining the recombination emission spectrum of GaN QDs in an AlN matrix under various excitation levels.

The structures with self-organized GaN/AlN QDs were grown by molecular beam epitaxy on a sapphire substrate in the (0001) direction. NH₃ was used as the source of active nitrogen. The given sequence of layers was accomplished as follows: a buffer AlN layer (100 nm) was grown first, and then 3D islands of GaN were formed on the AlN surface. It was found by reflection electron diffraction that the islands were formed at extremely thin coatings corresponding to two GaN monolayers without the formation of a two-dimensional GaN layer. These data were confirmed in studying the samples by high-resolution transmission electron microscopy. The height (4–6 nm) and the diameter (15–20 nm) of the QDs were also determined (see the inset in Fig. 1b). The density of the QDs did not exceed 10¹¹ cm⁻². The layer of GaN QDs was covered by a 10-nm AlN layer. To increase the emission intensity, this procedure was repeated ten times. Nevertheless, the number of layers with QDs was sufficiently small to

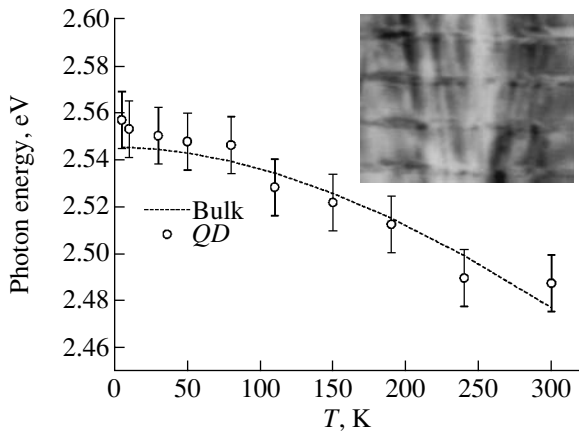
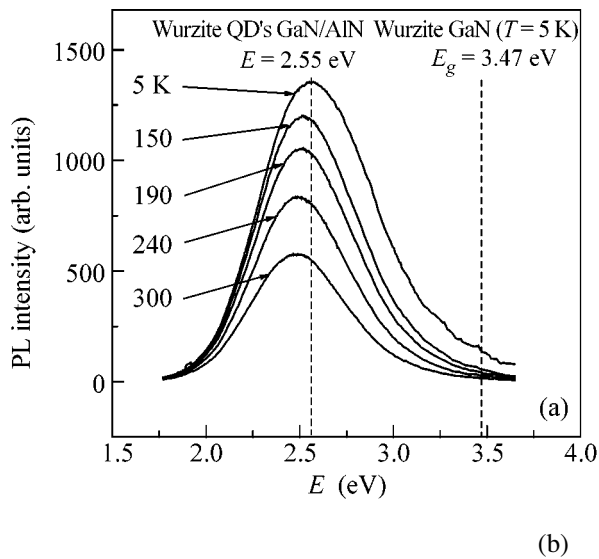


Fig. 1. Steady-state PL spectra: (a) spectra measured at various temperatures and (b) temperature dependence of the PL line maximum. The inset in the figure shows an image of GaN QDs in an AlN matrix obtained with a transmission electron microscope (TEM).

minimize the effects associated with the nonuniformity of QD excitation, which were discussed in [9].

The excitation of the steady-state photoluminescence was carried out by a He–Cd laser with a wavelength of 325 nm (3.81 eV) and by the second harmonic of an Ar⁺ laser with a wavelength of 244 nm (5.08 eV). The diameter of the excitation light spot on a sample was approximately 0.25 μm. The transient PL was excited by pulsed nitrogen laser radiation (a wavelength of 337 nm and a half-height pulse duration of 7 ns) with a pulse repetition frequency of 1 kHz. The energy density in a laser radiation pulse was 0.02 mJ/cm², and the beam diameter was about 5 mm. Note that the radiation energy of all the lasers used in this work was lower than the AlN bandgap (6.2 eV).

Figure 1 presents the steady-state PL spectra measured at various temperatures and the temperature dependence of the position of the PL peak. It is evident

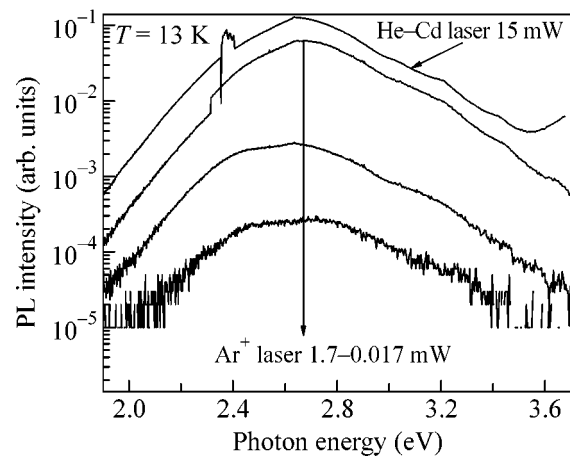


Fig. 2. Steady-state PL spectra measured with various pump powers at 13 K.

that the PL maximum at 5 K lies at 2.55 eV, which is approximately 0.9 eV lower than the bandgap width of bulk unstrained GaN (3.47 eV). The PL line width at half-height comprises about 0.7 meV. This line was not observed in the GaN and AlN films. With increasing the temperature from 5 to 300 K, the PL intensity drops approximately by a factor of 2.5, which is insignificant; the line shape and half-width remain virtually unchanged (Fig. 1a); and the PL maximum shifts toward the region of low energies by approximately 80 meV in accordance with the decrease in the bandgap width of bulk GaN (Fig. 1b). The data obtained indicate that the radiative recombination of nonequilibrium charge carriers occurs in GaN QDs.

The emission of GaN QDs below the bandgap width of bulk GaN is due to the quantum Stark effect [10]. The dependence of the optical transition energy on the QD height at different values of the electric field was reported in [3]. According to this dependence, the emission with energy at 2.55 eV observed in QDs 5 nm in height (which equals the average height of the QDs studied in this work) corresponds to an electric field of 5.5 MV/cm. The broadening of the PL line is related to fluctuations of QD sizes. In the structures grown with QDs, the height varied from 4 to 6 nm. This corresponds to the recombination emission energy in the range from 2.2 to 3.0 eV at the above field value. The weak drop in the PL intensity with temperature confirms the occurrence of strong charge carrier localization in QDs. In fact, under the action of the built-in field, electrons and holes shift toward the vertex and base of the QD, respectively, because of which the carriers undergo additional localization at barriers. With increasing temperature, the degree of localization decreases, resulting in an increase in the probability of the capture of charge carriers by radiationless sites, which occur in QDs.

Figure 2 presents the spectra of steady-state PL measured at 13 K and various laser excitation powers.

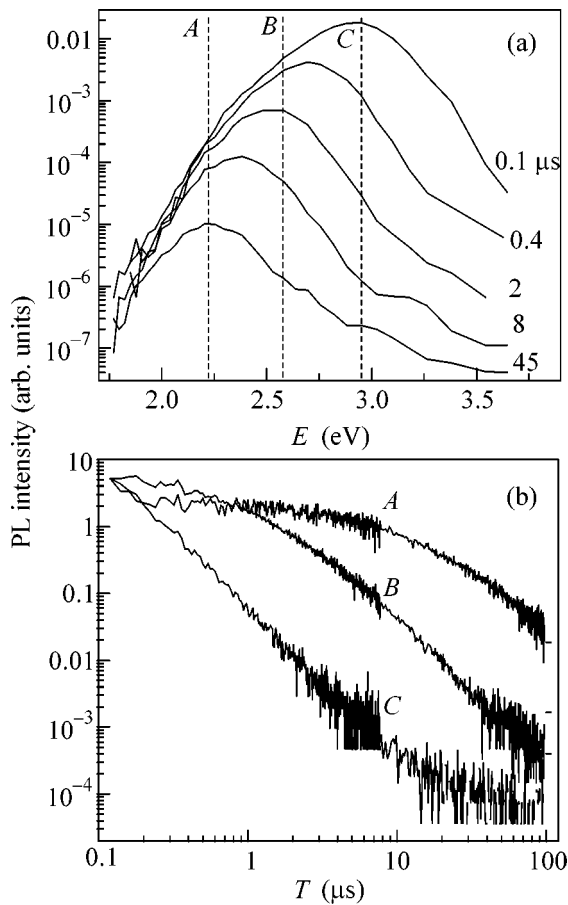


Fig. 3. Transient PL spectra: (a) spectra measured at different instants of time after an excitation pulse; (b) PL decay curves at different points of the spectrum.

The figure demonstrates that the QD PL spectrum covers the entire range of visible radiation. The appreciable luminescence in the range of photon energies $h\nu > 3$ eV is associated with recombination in small-size QDs, which also occur in the studied samples according to electron microscopy data. The PL spectrum varies insignificantly upon varying the pump power. It should be noted that the relative PL intensity in the low-energy spectral region increases upon decreasing the pump power. Such a relative increase in the PL intensity in the red spectral region was more pronounced at room temperature, and the PL spectrum shifted toward the red side approximately by 200 meV upon decreasing the pump power from 10 to 0.01 mW.

The transient PL spectra of QDs at $T = 5$ K are shown in Fig. 3a. This figure demonstrates that the PL spectrum at small delay times after the excitation pulse is broad and spans the entire visible range. In the course of time after the excitation pulse, the PL line becomes narrower and the maximum shifts toward the low-energy side from 3.0 to 2.2 eV. The main shift of the PL line takes place in the first 10 μ s after the excitation pulse. The decrease in the width of the PL spectrum

points to the fact that the recombination of nonequilibrium charge carriers in small-size QDs is faster than that in large-size QDs.

The PL decay law at different points of the spectrum is presented in Fig. 3b. It is evident that this law is non-exponential at all spectral lines and strongly varies along the spectrum. The decay law in the high-energy part of the spectrum is well approximated by the $1/t^\gamma$ law with $\gamma = 2$, indicating that the lifetime dispersion of nonequilibrium charge carriers in QDs is significant. The most interesting experimental observation is the constancy of the PL intensity within about 10 μ s after the excitation pulse in the low-energy wing of the PL line (curve A in Fig. 3b). The QD PL decay law remains virtually constant upon increasing the measurement temperature up to 300 K. The QD PL decay law measured in this work differs from the data reported in [2]. In this work, it was inferred from measurements of PL kinetics in a narrow time range up to 1 ns that the QD PL decay is exponential. Nevertheless, an increase in the PL decay time in the red spectral region was also noted in this work. The relatively long absence of the decay of red PL found in our work means that the concentration of nonequilibrium charge carriers in large QDs remains constant during this time. Hence, the loss of nonequilibrium charge carriers in large QDs due to recombination is replenished by the external supply of charge carriers. It should be noted that the PL intensity in the high-energy line wing almost completely decays in the same time (curve C in Fig. 3b); that is, nonequilibrium charge carriers virtually do not remain in small QDs.

The experimental data presented above indicate that the huge shift of the transient PL line toward the red side within some time after the excitation pulse is primarily associated with the dependence of the lifetime of nonequilibrium charge carriers in QDs on their height. This dependence appears because of the occurrence of the built-in electric field in wurtzite structures with QDs. This conclusion is in agreement with the data of theoretical calculations [1], from which it follows that the lifetime of nonequilibrium charge carriers in QDs changes by more than one order of magnitude upon changing the QD height by 1 nm, and also with the experimental data on the lifetime in QDs obtained by other authors [7].

The unusual PL decay law in the red spectral region is evidently related to the transition of charge carriers from small-size QDs to larger QDs. The rather high density of QDs in our structures gives grounds for such a suggestion. Correlation between the onset time of PL decay in large QDs and the time required for the complete depletion of small QDs also provides evidence in favor of this suggestion. The invariability of the PL decay law with increasing temperature points to a tunneling mechanism of exciton transfer between QDs. At the same time, the supply of charge carriers from some local centers in the AlN matrix would lead to approxi-

mately the same increase in the PL decay time of large-size and small-size QDs. It should be noted that exciton transfer between QDs was observed previously in QDs of other types, for example, between InAs QDs in an AlAs matrix [11].

Thus, the PL of self-organized GaN QDs was studied in this work. A PL line below the GaN bandgap width related to recombination in QDs was found. The line maximum in the transient spectrum shifts to the red side by approximately 1 eV for several tens of microseconds. This shift is associated with the dependence of the recombination rate of charge carriers on the dot size in the strong internal electric field. The long decay of the low-energy region of the transient spectrum is also caused by the transfer of nonequilibrium carriers from small to large GaN QDs.

REFERENCES

1. V. Ranjan, G. Allan, C. Priester, *et al.*, Phys. Rev. B **68**, 115305 (2003).
2. J. Simon, N. T. Pelekanos, C. Adelman, *et al.*, Phys. Rev. B **68**, 035312 (2003).
3. F. Widmann, J. Simon, B. Daudin, *et al.*, Phys. Rev. B **58**, R15989 (1998).
4. B. Damilano, N. Grandjean, F. Semond, *et al.*, Appl. Phys. Lett. **75**, 962 (1999).
5. P. Ramvall, S. Tanaka, S. Nomura, *et al.*, Appl. Phys. Lett. **73**, 1104 (1998).
6. C. Adelman, E. Sarigiannidou, D. Jalabert, *et al.*, Appl. Phys. Lett. **82**, 4154 (2003).
7. S. Kalliakos, T. Bretagnon, P. Lefebvre, *et al.*, J. Appl. Phys. **96**, 180 (2004).
8. K. S. Zhuravlev *et al.*, in *Proceedings of the 27th International Conference on Physics of Semiconductors* (Flagstaff, USA, 2004) (in press).
9. S. Kalliakos, *These Effects de Fortes Photo-excitations sur les Puits et Boites Quantiques a Base de Nitrures d'Elements III (Phase Wurtzite)* (2003), p. 77.
10. G. Bastard, *Wave Mechanics Applied to Semiconductor Heterostructures* (Halsted Press, New York, 1991), p. 308.
11. T. S. Shamirzaev, A. M. Gilinskiĭ, A. K. Bakarov, *et al.*, Pis'ma Zh. Éksp. Teor. Fiz. **77**, 459 (2003) [JETP Lett. **77**, 389 (2003)].

Translated by A. Bagatur'yants

Anomalies in Transport Properties in a Magnetically Ordered Region on a Kondo Lattice

S. S. Aplesnin

Kirenskiĭ Institute of Physics, Siberian Division, Russian Academy of Sciences,
Akademgorodok, Krasnoyarsk, 660036 Russia

Siberian State Aerospace Academy, Krasnoyarsk, 660036 Russia

e-mail: apl@iph.krasn.ru

Received December 3, 2004; in final form, December 13, 2004

The temperature dependences of resistivity and thermal emf on a Kondo lattice are calculated using the spin-polaron approximation. The peaks and sign reversal points of thermal emf as a function of temperature and concentration below the temperature of the transition to the paramagnetic state are determined. The concentration region containing the metal–insulator transition below the Curie temperature and the shift of the upper spin-polaron band are calculated. © 2005 Pleiades Publishing, Inc.

PACS numbers: 72.15.Qm; 72.20.–i

Intensive studies of manganites are stimulated by both the existence of the giant magnetoresistance effect and the possibility of application of these materials in spintronics. The magnetic ordering changes from the antiferromagnetic to ferromagnetic (FM) type, and the semiconductor–metal transition occurs at the critical concentration of the substitution of bivalent Ca^{2+} and Sr^{2+} ions for trivalent lanthanum ions [1–3]. Above the critical concentration ($x > x_c$), the resistivity in the FM region below the Curie temperature drops abruptly and is correctly described in the double exchange model [4]. In the vicinity of a concentration of $x \sim 0.5$, the metal–insulator transition is observed in $\text{La}_{0.5}\text{Ca}_{0.5-x}\text{Ba}_x\text{MnO}_3$ [5] below the Curie temperature $T_M/T_c = (x = 0) 0.87$, ($x = 0.1$) 0.78, and ($x = 0.2$) 0.6. This transition can be interpreted using the phase-separation model. In other words, regions with the metal- and semiconductor-type conductivity exist due to small-radius polarons. However, the values of the activation energy calculated from the temperature dependences of the Seebeck coefficient $S(T)$ and resistivity differ from each other by an order of magnitude.

Available theories cannot explain an increase in the absolute value of thermal emf in double-layer manganites $\text{RSr}_2\text{Mn}_2\text{O}_7$ ($R = \text{La}, \text{Pr}$) in the helium temperature range [6]. The minimum observed in the $S(T)$ dependence for $\text{La}_{1.4}(\text{Sr}_{1-y}\text{Ca}_y)\text{Mn}_2\text{O}_7$ in the temperature interval $60 \text{ K} < T < 150 \text{ K}$ can be interpreted as a complex contribution from phonons and electrons to $S(T) = A/T + BT$. The sign reversal of the thermoelectric coefficient as a function of the temperature and concentration in manganites is explained by the presence of two types of carriers (electrons and holes) with different activation energies.

In this study, the above-mentioned effects are described in the Kondo-lattice model using spin polarons as charge carriers. The temperature and concentration ranges in which the Seebeck coefficient changes its sign and the metal–insulator transition occurs below the temperature of the transition to the magnetically ordered state are determined as functions of the spin-polaron band population and the Hund interaction parameter. The model proposed here differs from the double-exchange model, in which the hopping of Mn ions over e_g levels leads to the formation of ferromagnetic exchange, while hopping over t_{2g} states leads to the antiferromagnetic exchange between localized electrons. We assume that the motion of charged carriers takes place in the oxygen system and that the electron spin is polarized by the ordered arrangement of manganese spins due to the hybridization of oxygen and manganese ions. According to the x-ray diffraction data [7], the weights of the $3d^5L^1$ and $3d^6L^2$ states are approximately equal to 41 and 9%, which corresponds to one- and two-hole states. These states are located in the gap, and they can be treated as impurity bands near the chemical potential and described in the model of nearly free electrons. As applied to manganites, our model presumes that the substitution of the bivalent ion Sr^{2+} or Ca^{2+} for the trivalent La^{3+} ion leads to an increase in the concentration of holes on oxygen ions. Oxygen nonstoichiometry also forms the hole states on oxygen.

Spin-polaron excitations can be calculated in the framework of the Kondo-lattice model using the method proposed by Barabanov *et al.* [8]. The Hamiltonian has the form

$$H = H_0 + H_1 + H_2,$$

$$H_0 = \sum_{\mathbf{r}, \mathbf{g}} t_{\mathbf{g}} a_{\mathbf{r}+\mathbf{g}, \sigma}^+ a_{\mathbf{r}, \sigma} = \sum_{\mathbf{k}} \varepsilon_{\mathbf{k}} a_{\mathbf{k}, \sigma}^+ a_{\mathbf{k}, \sigma}, \quad (1)$$

$$H_1 = J \sum_{\mathbf{r}, \sigma_1, \sigma_2} a_{\mathbf{r}, \sigma_1}^+ S_{\mathbf{r}}^\alpha \hat{\sigma}_{\sigma_1, \sigma_2}^\alpha a_{\mathbf{r}, \sigma_2},$$

$$H_2 = -\frac{1}{2} \sum_{\mathbf{r}, \mathbf{g}} (I_1 S_{\mathbf{r}+\mathbf{g}1}^\alpha S_{\mathbf{r}}^\alpha + I_2 S_{\mathbf{r}+\mathbf{g}2}^\alpha S_{\mathbf{r}}^\alpha),$$

where summation is carried out over the cubic lattice sites, I_1 and I_2 are the exchange interactions between the nearest and next-to-nearest neighbors, $a_{\mathbf{k}, \sigma}^+$ is the creation operator for an electron with the spin index $\sigma = \pm 1$, H_1 is the Hamiltonian of the s - d interaction, and $\hat{\sigma}^\alpha$ are the Pauli matrices with $\alpha = x, y, z$.

Let us write the equations of motion for the Green's functions describing the motion of the electron over oxygen ions. The electron spin interacts with the magnetically ordered spins of manganese ions. Using the random phase approximation, we close the system of equations for the Green's functions $\langle\langle a_{\mathbf{r}, \sigma} | a_{\mathbf{r}, \sigma}^+ \rangle\rangle$ and $\langle\langle b_{\mathbf{r}, \sigma} | a_{\mathbf{r}, \sigma}^+ \rangle\rangle$, where $b_{\mathbf{r}\sigma} = S_{\mathbf{r}}^\alpha \hat{\sigma}_{\sigma, \sigma_1}^\alpha a_{\mathbf{r}, \sigma_1}$ and $\alpha = x, y$. These equations have the form

$$\begin{aligned} (\omega - \varepsilon_{\mathbf{k}}) G_{\mathbf{k}}^1 &= 1 + \frac{J}{2} G_{\mathbf{k}}^2, \\ (\omega - e_{\mathbf{k}}) G_{\mathbf{k}}^2 &= J(1 + m - 2nm) G_{\mathbf{k}}^1, \\ G_{\mathbf{k}}^1 &= \langle\langle a_{\mathbf{k}, \sigma} | a_{\mathbf{k}, \sigma}^+ \rangle\rangle; \quad G_{\mathbf{k}}^2 = \langle\langle b_{\mathbf{k}, \sigma} | a_{\mathbf{k}, \sigma}^+ \rangle\rangle, \\ \varepsilon_{\mathbf{k}} &= \varepsilon_{\mathbf{k}}^0 + \frac{Jm}{4} - \mu, \\ \varepsilon_{\mathbf{k}}^0 &= -2(t_{xy}(\cos k_x + \cos k_y) + t_z \cos k_z), \\ e_{\mathbf{k}} &= 2(z_1 c_1 + z_2 c_2) \varepsilon_{\mathbf{k}}^0 + J \left(\frac{m}{2} + n \right) \\ &\quad + m \left(\frac{z_1}{2} I_1 + \frac{z_2}{2} I_2 \right) - \mu, \\ n &= \langle a_{\uparrow}^+ a_{\uparrow} + a_{\downarrow}^+ a_{\downarrow} \rangle. \end{aligned} \quad (2)$$

Here, $b_{\mathbf{k}, \sigma}$, $a_{\mathbf{k}, \sigma}$, and $G_{\mathbf{k}}$ are the Fourier transforms of the corresponding single-node operators and Green's functions, respectively, $c_{1,2} = \langle S_{\mathbf{r}}^x S_{\mathbf{r}+\mathbf{g}1,2}^x + S_{\mathbf{r}}^y S_{\mathbf{r}+\mathbf{g}1,2}^y \rangle$ is the spin-spin correlation function for transverse spin components, and z_1 and z_2 are the numbers of the nearest and next-to-nearest neighbors. All energies are mea-

sured from the chemical potential μ . The excitation spectrum has the form

$$\begin{aligned} &\omega_{1,2}(\mathbf{k}) \\ &= \frac{1}{2} \left[\varepsilon_{\mathbf{k}} + e_{\mathbf{k}} \pm \sqrt{(\varepsilon_{\mathbf{k}} - e_{\mathbf{k}})^2 + J^2 \left(\frac{1+m}{2} - nm \right)} \right]. \end{aligned} \quad (3)$$

The chemical potential is calculated self-consistently for a given electron concentration n ,

$$n = \frac{1}{N} \sum_{\mathbf{k}} \int d\omega f(\omega) \frac{1}{\pi} \text{Im} G^1, \quad (4)$$

where $f(\omega) = (\exp(\omega/T) + 1)^{-1}$. Summation is carried out over 8×10^6 points in the first Brillouin zone. Here, we analyze the effect of magnetic ordering on the transport properties. For this reason, we consider the magnetic system in the adiabatic approximation to simplify the problem. The free energy expansion gives a power dependence for magnetization $m = m_0 \sqrt{1 - T/T_c}$, where m_0 varies from $m_0 = 3.8 \mu_B$ in LaMnO₃ [9] to $m_0 = 2.8 \mu_B$ in CaMnO₃ [10]. The spin-spin correlation for the transverse spin components in the phase-transition region is about $c_{c1} \sim 0.1 m_0$ for $r = 1$ in accordance with Monte Carlo calculations in the classical Heisenberg model [11]. For $r = \sqrt{2}$, we have $c_{c2} \sim c_{c1} / \sqrt{2}$. The temperature dependence of c_1 and c_2 was described by the power function $c_{1,2} = c_{c1,2} (T/T_c)^2$ for $T < T_c$ and $c_{1,2} = c_{c1,2} (2 - T/T_c)^2$ for $T > T_c$. The typical values of exchange integrals, $I_1 \sim 1$ meV and $I_2 \sim 0.2$ meV [12], are three orders of magnitude smaller than the hopping integral and practically do not affect conductivity. The temperature of the transition from the magnetically ordered state to the paramagnetic phase in manganites varies in the interval $150 \text{ K} < T_c < 300 \text{ K}$, and we used the normalized quantity $T_c/t = 0.15$ in our calculations. The dynamic conductivity σ and the thermoelectric coefficient S were calculated using the Kubo-Greenwood formula [13]

$$\begin{aligned} \sigma &= \frac{e^2}{T} L^{11}, \\ S &= \frac{1}{eT} \frac{L^{12}}{L^{11}}, \end{aligned} \quad (5)$$

$$L^{11} = T \sum_{\sigma} \sum_{\mathbf{k}} \int d\omega \left(-\frac{\partial f(\omega)}{\partial \omega} \right) A_{\sigma}^2(\mathbf{k}, \omega),$$

$$L^{12} = T \sum_{\sigma} \sum_{\mathbf{k}} \int d\omega \left(-\frac{\partial f(\omega)}{\partial \omega} \right) A_{\sigma}^2(\mathbf{k}, \omega) \omega,$$

where $A_{\sigma}(\mathbf{k}, \omega) = -(1/\pi) \text{Im} G_{\sigma}(\mathbf{k}, \omega)$ is the spectral Green's function.

According to the calculations of the electron density functional $LDTA + U$, the gap width for the Mn-O

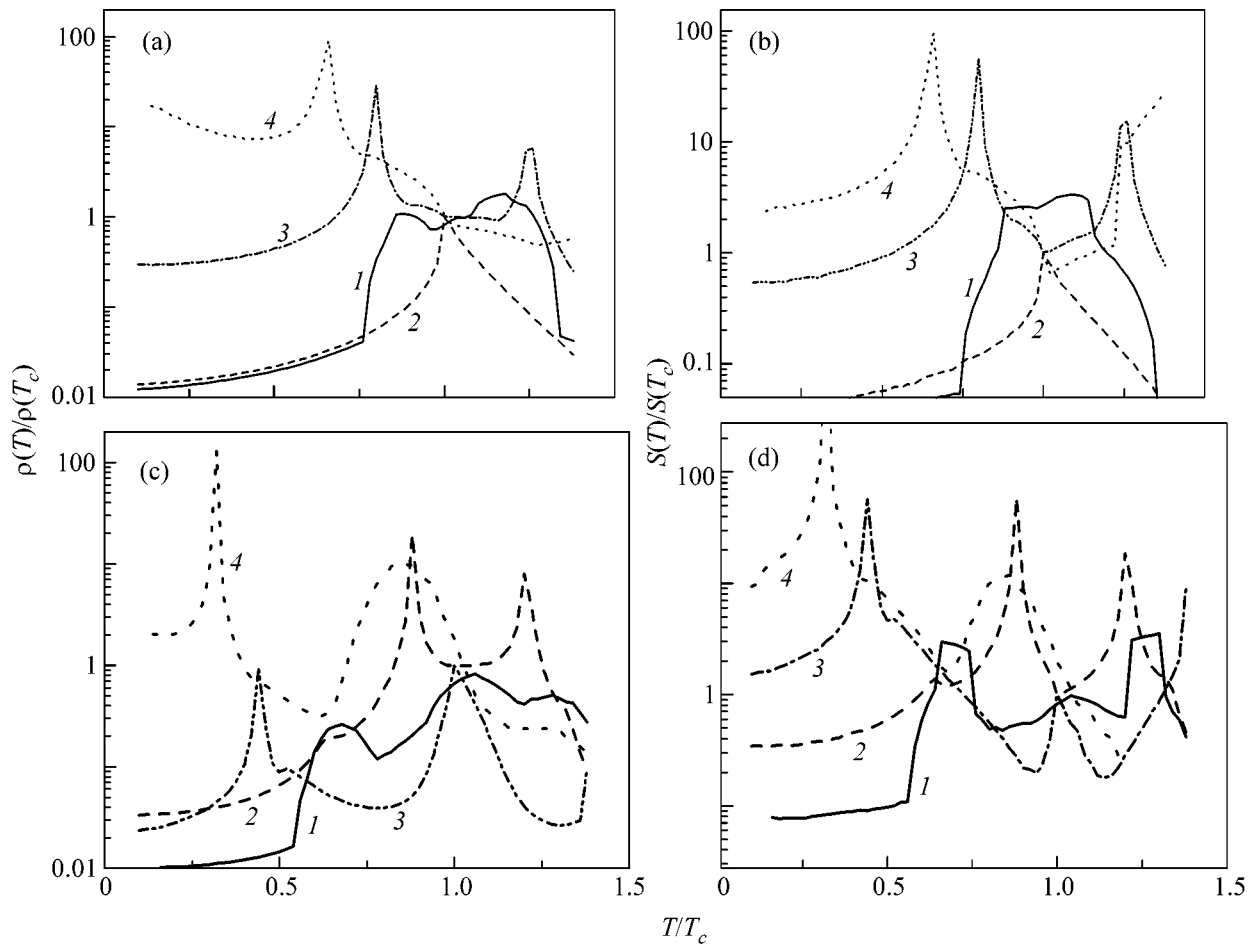


Fig. 1. (a, c) Resistivity $\rho(T)/\rho(T_c)$ and (b, d) thermal emf $S(T)/S(T_c)$ vs. the normalized temperature for $J/t =$ (a, b) 8 and (c, d) 3 and $x =$ (1) 0.1, (2) 0.3, (3) 0.5, and (4) 0.65.

charge transfer in LaMnO_3 is $(\epsilon_p - \epsilon_d) \sim 3.2$ eV [14] and the upper edge of the electron excitation band for oxygen lies below the chemical potential level by ~ 1 eV. The Mn–Mn electron orbitals do not overlap directly; the overlap integral of the wave functions between the Mn and O ions is $t(pd\sigma) = -1.99$ eV and $t(pd\pi) = 1.1$ eV, and $t(pp\sigma) = 0.7$ eV and $t(pp\pi) = -0.16$ eV for the O–O overlapping [15]. Electron excitations are localized on the manganese ions due to the large charge gap and Coulomb interaction, and nonstoichiometry facilitates the formation of holes with a higher mobility in the oxygen subsystem. The exchange interaction of hole spins on the oxygen ions with the spins on the manganese ions leads to the splitting of the hole band.

Numerical calculations of the transport coefficients by formulas (5) give two main temperature dependences of resistivity: a sharp decrease in the resistivity at a temperature of $T^* \leq T_c$, $x < x_{c1}$ and at the metal–insulator transition at $T_{MI} < T_c$, $x > x_{c1}$. The corresponding $\rho(T)$ dependences are shown in Fig. 1. This behavior becomes clear from analysis of the spectrum of spin-polaron excitations and the density of states $g(\omega)$.

In the vicinity of the Curie temperature, the two subbands overlap and form a peak of $g(\omega)$ in the overlap region. For low concentrations $x < x_{c1}$, the chemical potential lies at the bottom of the band. Upon cooling, the bands split and the chemical potential level gets into the van Hove region in the lower band. Since the conductivity is proportional to the density of states $N(0)$ at the chemical potential level, this behavior gives rise to a singularity in the $\rho(T)$ dependence. In the concentration range $x_{c1} < x$, the density $N(0)$ of spin-polaron excitations decreases sharply during the formation of long-range magnetic order, which corresponds to semiconductor-type conductivity. The transition temperature T_{MI} depends on the s – d interaction parameter and the band population and is determined by the shift of the chemical potential level from the upper subband to the lower one upon an increase in magnetization. The electron group velocity decreases sharply in this case, $v_k = \nabla\omega(k)$, and the conductivity is of the semiconductor type, because $\sigma \sim v_\mu^2 N(0)^2$, with a peak of $\rho_{\max}(T_{MI})$ at the temperature at which the chemical potential level exactly coincides with the bottom of the upper subband.

Figure 2a shows the dispersion curves in the [111] direction for two temperatures: $T < T_{MI}$ and $T > T_{MI}$. The density of states remains virtually unchanged at these temperatures (Fig. 2b). Band splitting increases with the s - d interaction parameter, and higher electron concentrations are required for the chemical potential to lie in the upper band. This leads to an increase in the metal-insulator transition temperature T_{MI} , which is observed in Fig. 1.

The calculated temperature dependences of thermal emf are in qualitative agreement with the conductivity type. Namely, the Seebeck coefficient for $\rho(T)$ of the metal and semiconductor types increases and decreases, respectively, with increasing temperature (see Fig. 1). In the quasi-two-dimensional case, this correlation is violated. Figure 3 shows the $\rho(T)$ and $S(T)$ curves for the anisotropic hopping parameters $t_z/t_{xy} = 0.1$, which are typical of double manganites $\text{LaSr}_2\text{Mn}_2\text{O}_7$ [16]. The thermal emf attains its minimum in the region of the transition to the paramagnetic state and changes its sign from positive to negative both in temperature and in concentration for $x_c < x$. The sign reversal of $S(T)$ is due to the specific behavior of the density of states in the vicinity of the chemical potential, which is shown in Fig. 2. For example, the densities of states for $\omega > 0$ and $\omega < 0$ in the energy range close to the Curie temperature differ from each other by several times, while the density of states $g(\omega)$ in the low-temperature range for constant parameters x and J is practically symmetric with respect to the chemical potential in the interval $\Delta\omega \approx 2T_c$. Doped manganites are semimetals in accordance with the spin-resolution photoemission data [17]. The calculated $\rho(T)$ and $S(T)$ dependences qualitatively explain two peaks in the temperature dependence of the thermal emf with a minimum in the vicinity of the Curie temperature in $\text{La}_{1.2}\text{Sr}_{1.8}\text{Mn}_2\text{O}_7$ [18] and the sign reversal of the thermal emf as a function of the temperature in $\text{La}_{1-x}\text{Ca}_x\text{MnO}_3$ for $x = 0.32$ [19]. The region in which the thermal emf changes its sign in the magnetically ordered state at $T < T_c$ strongly depends on the dimensionality of the space and is shown on the x - J phase diagram in Fig. 4a.

The conductivity calculated using the dynamical mean field method disregarding the dependence of the electron self-energy on the quasimomentum [4] decreases rapidly with increasing magnetization $\rho(m)/\rho(m=0) = 1 - Cm^2$. In this approximation, it is impossible to obtain a metal-insulator transition in temperature for $T_{MI} < T_c$.

In our model, we assume that conduction is realized over oxygen ions and that the upper edge of the band shifts towards high frequencies at $T < T_c$, where $t_z = t_{xy}$ and the shift increases with concentration (see Fig. 4). The intrinsic absorption edge corresponding to a gap of approximately 1 eV is determined from the diffuse reflection spectra for $\text{La}_{0.9}\text{Sr}_{0.1}\text{MnO}_3$ [20]. In the tem-

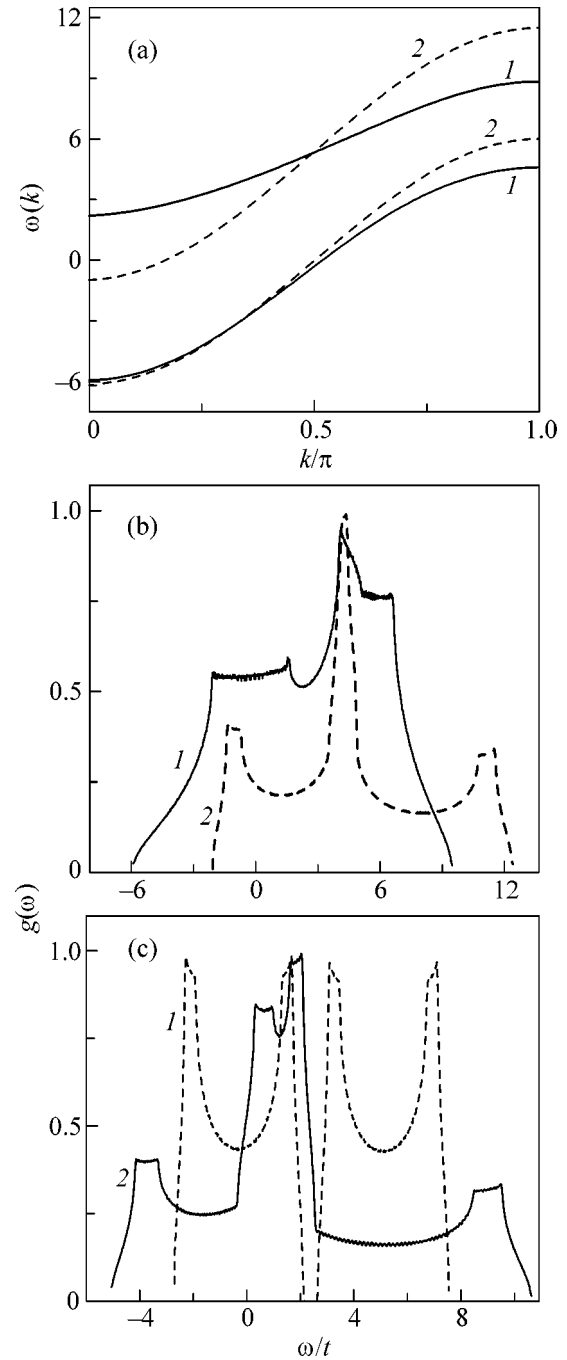


Fig. 2. (a) Spectrum of spin-polaron excitations $w_{[111]}(k)$ at temperatures $T/T_c =$ (solid curves) 1/3 and (dashed curves) 0.47 for $J/t = 3$ and $x = 0.5$. (b, c) Density of states of spin-polaron excitations for $J/t = 3$ and (b) $x =$ (1) 0.5 and (2) 0.25, $T/T_c =$ (1) 0.4 and (2) 0.8, and $t_z/t_{xy} =$ (1) 1 and (2) 0.1; and (c) $x = 0.5$, $t_z/t_{xy} = 0.1$, and $T/T_c =$ (1) 0.55 and (2) 0.88.

perature range from $T_c = 155$ K to 140 K, the intrinsic absorption edge shifts by a giant value of about 0.4 eV [20]. Figure 4 shows the theoretical and experimental results, which are in satisfactory agreement. According

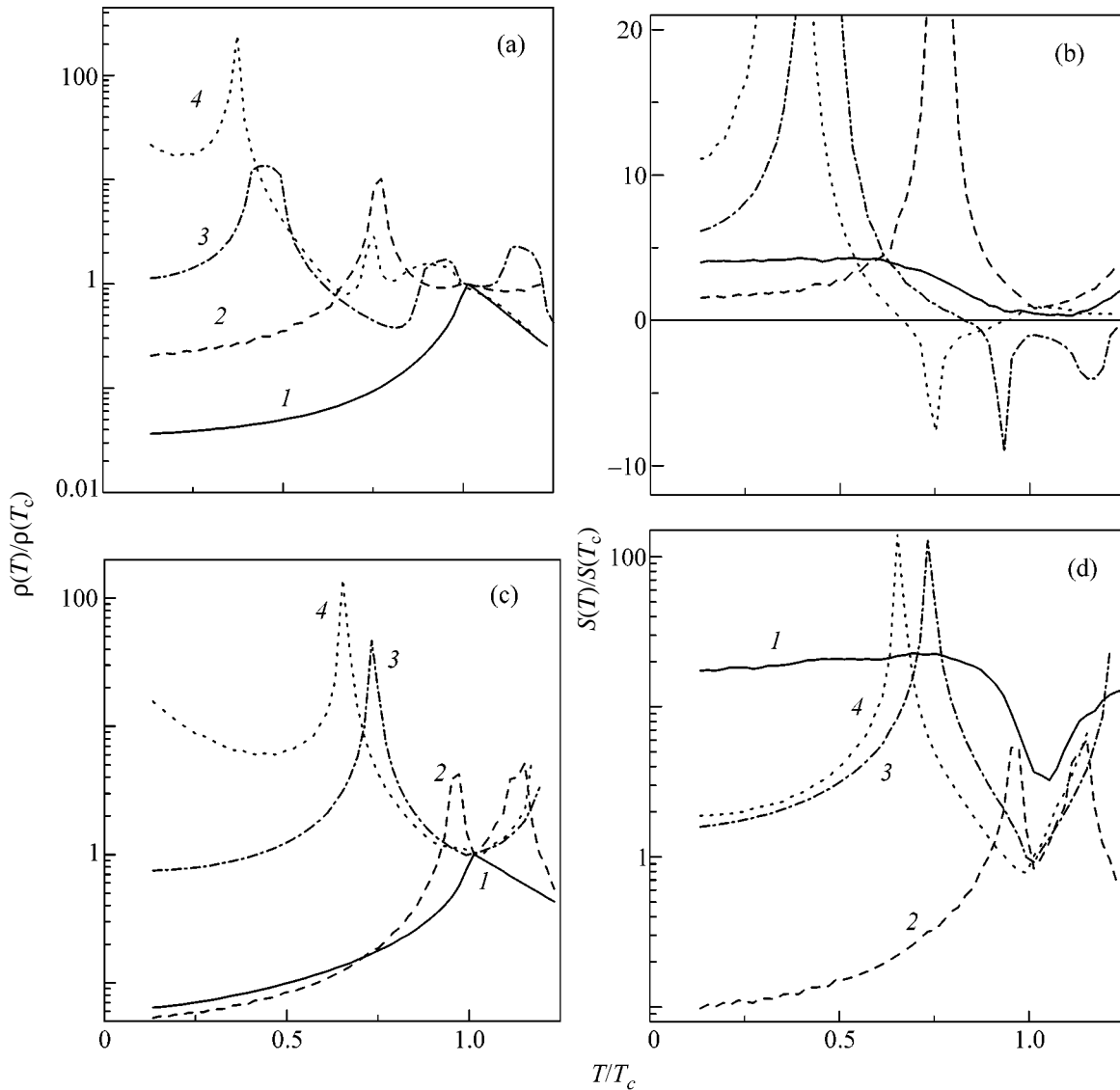


Fig. 3. (a, c) Resistivity and (b, d) thermal emf in a quasi-two-dimensional system vs. the normalized temperature for $t_z/t_{xy} = 0.1$, $J/t =$ (a, b) 3 and (c, d) 6, and $x =$ (1) 0.1, (2) 0.3, (3) 0.5, and (4) 0.65.

to Demin *et al.* [20], the red shift of the gap is associated with the shift of the top of the valence band and rules out the electron-phonon interaction mechanism in view of its smallness, because the isotopic effect is small in this band [21].

The application of our spin-polaron model for describing the transport properties of manganites is restricted to metallic compounds with a long-range or short-range ferromagnetic order in the vicinity of the Curie temperature. In the framework of this model, it is impossible to obtain the temperature dependence of resistivity for nonferromagnetic doped manganites. The temperature and magnetic-field dependences of resistivity in these compounds are described in the inhomogeneous-state model [22], in which a ferromagnetic polaron is pinned at an impurity center or moves

very slowly in the insulator matrix. The main contribution to transport in this case comes from electron hopping from one stationary ferron to a neighboring one. The resistivity in the phase-separated region is governed by the Mott law $\rho(T) \sim T \exp(A/2k_B T)$, where the energy barrier height $A \sim e^2/\epsilon_0 R_f$ depends on the ferron radius R_f . Our model can be used in the concentration range $0.18 < x < 0.5$ for $\text{La}_{1-x}\text{A}_x\text{MnO}_3$, $\text{A} = \text{Ca}, \text{Sr}$ [23] and in the range $0.2 < x < 1$ for $\text{La}_{2-2x}\text{Sr}_{1+2x}\text{Mn}_2\text{O}_7$ [16] and other ferromagnetic compounds exhibiting the metal-insulator transition in temperature.

Thus, the interaction of free charge carriers with localized spins in the range of high concentrations leads to a resistivity peak below the Curie temperature. The peak observed in the $\rho(T)$ dependence for manganites with the FM ordering is also successfully explained in

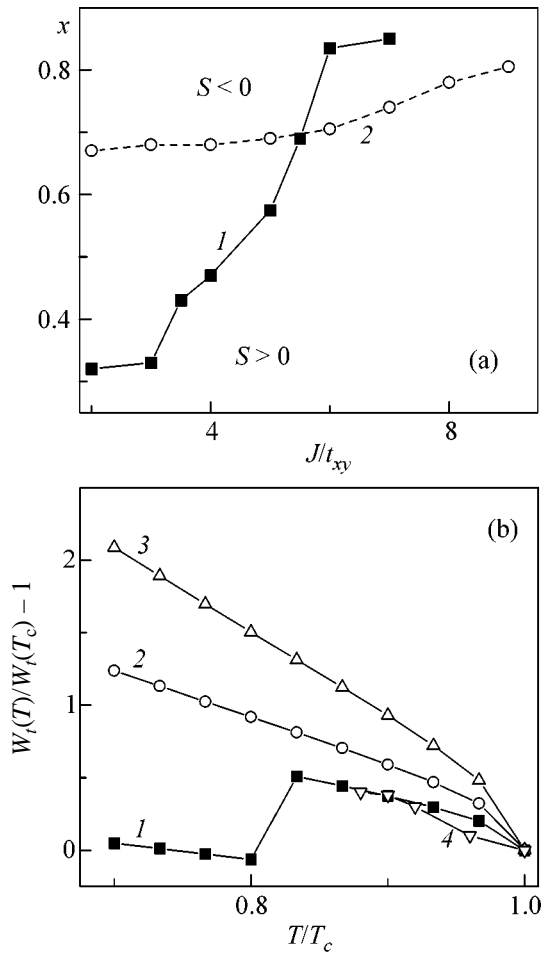


Fig. 4. (a) Lines on the x - J phase diagram separate the upper region with the sign reversal of thermal emf at $T < T_c$ from the lower region with $S(T) > 0$ for $t_z/t_{xy} = (1)$ 0.1 and (2) 1. (b) Normalized shift of the upper edge of the spin-polaron excitation band $W_u(T)/W_u(T_c) - 1$ as a function of the normalized temperature T/T_c for $J/t = 8$, $x = (1)$ 0.15, (2) 0.25, (3) 0.35, and (4) $\text{La}_{0.9}\text{Sr}_{0.1}\text{MnO}_3$ [20].

the spin polaron model as in the case of lower concentrations. The sign reversal in the temperature dependence of the Seebeck coefficient, as well as in its concentration dependence, also fits the spin-polaron excitation model without including the phonon mechanism or phase separation. The splitting and shift of the spin-polaron band satisfactorily correlate with the shift of the top of the valence band determined from the diffuse scattering data for manganites.

REFERENCES

1. É. L. Nagaev, Usp. Fiz. Nauk **166**, 833 (1996) [Phys. Usp. **39**, 781 (1996)].

2. L. P. Gor'kov, Usp. Fiz. Nauk **168**, 666 (1998) [Phys. Usp. **41**, 589 (1998)]; M. Yu. Kagan and K. I. Kugel', Usp. Fiz. Nauk **171**, 577 (2001) [Phys. Usp. **44**, 553 (2001)].
3. Yu. A. Izyumov and Yu. N. Skryabin, Usp. Fiz. Nauk **171**, 121 (2001) [Phys. Usp. **44**, 109 (2001)].
4. N. Furukawa and K. Hirota, Physica B (Amsterdam) **241-243**, 780 (1997).
5. H. Wakai, J. Phys.: Condens. Matter **13**, 1627 (2001).
6. S. Chatterjee, P. H. Chou, C. F. Chang, *et al.*, Phys. Rev. B **61**, 6106 (2000).
7. D. D. Sarma, O. Rader, T. Kachel, *et al.*, Phys. Rev. B **49**, 14238 (1994).
8. A. F. Barabanov, L. A. Maksimov, and A. V. Mikheenkoy, Pis'ma Zh. Éksp. Teor. Fiz. **74**, 362 (2001) [JETP Lett. **74**, 328 (2001)].
9. M. B. Salamon and M. Jaime, Rev. Mod. Phys. **73**, 583 (2001).
10. W. E. Pickett and D. J. Singh, Phys. Rev. B **53**, 1146 (1996).
11. S. S. Aplesnin, Fiz. Met. Metalloved. **63**, 190 (1987).
12. D. Feinberg, P. Germain, M. Grilli, and G. Seibold, Phys. Rev. B **57**, R5583 (1998).
13. K. Nagai, T. Momoi, and K. Kubo, J. Phys. Soc. Jpn. **69**, 1837 (2000).
14. A. Chainani, M. Mathew, and D. D. Sarma, Phys. Rev. B **47**, 15397 (1993).
15. P. Mahadevan, N. Shanthi, and D. D. Sarma, Phys. Rev. B **54**, 11199 (1996).
16. Y. Liu, L. Sheng, D. Y. Xing, and J. Dong, J. Phys.: Condens. Matter **10**, 9747 (1998).
17. V. Yu. Irkhin and M. I. Katsnel'son, Usp. Fiz. Nauk **164**, 705 (1994) [Phys. Usp. **37**, 659 (1994)].
18. J. S. Zhou, J. B. Goodenough, and J. F. Mitchell, Phys. Rev. B **58**, R579 (1998).
19. A. Asamitsu, Y. Moritomo, and Y. Tokura, Phys. Rev. B **53**, R2952 (1996); K. M. Kojima, Y. Fudamoto, M. Larkin, *et al.*, Phys. Rev. Lett. **78**, 1787 (1997).
20. R. V. Demin, L. I. Koroleva, and A. M. Balbashov, Pis'ma Zh. Éksp. Teor. Fiz. **70**, 303 (1999) [JETP Lett. **70**, 314 (1999)].
21. G. M. Zhao, K. Conder, H. Keller, and K. A. Müller, Nature **381**, 676 (1996).
22. A. L. Rakhmanov, K. I. Kugel, Ya. M. Blanter, and M. Yu. Kagan, Phys. Rev. B **63**, 174424 (2001); K. I. Kugel', A. L. Rakhmanov, A. O. Sbořchakov, *et al.*, Zh. Éksp. Teor. Fiz. **125**, 648 (2004) [JETP **98**, 572 (2004)].
23. J. Hemberger, A. Krimmel, T. Kurz, *et al.*, Phys. Rev. B **66**, 094410 (2002).

Translated by N. Wadhwa

Experimental Evidence of the Hybridization of the Electron States of an Impurity and the Conduction Band in the HgSe:Fe System

V. I. Okulov¹, L. D. Sabirzyanova¹, É. Z. Kurmaev¹, L. D. Finkel'shtein¹,
R. F. Karimov², A. Moewes³, and S. Yu. Paranchich⁴

¹ Institute of Metal Physics, Ural Division, Russian Academy of Sciences,
ul. S. Kovalevskoi 18, Yekaterinburg, 620219 Russia

e-mail: okulov@imp.uran.ru

² Department of Materials Science and Engineering, Kyoto University, Yoshidahonmachi,
Sakyo-ku, Kyoto 606-8501, Japan

³ University of Saskatchewan, Department of Physics and Engineering Physics, Saskatoon, SK, S7N 5E2, Canada

⁴ Chernovtsy National University, Chernovtsy, 58012 Ukraine

Received December 13, 2004

X-ray absorption spectra from iron donor impurities in mercury selenide have been analyzed in a concentration range where the Fermi energy of conduction electrons is close to the energy of the donor d level. At high impurity concentrations, the resulting spectrum corresponds to the completely filled donor state and coincides with the spectrum of a bivalent iron ion. A transition to an intermediate-filling state is observed with decreasing the concentration. The spectra are quantitatively analyzed in a model implying the existence of a mixture of ions that contain and do not contain a donor electron in a bound state. It has been found that such a model is significantly inconsistent with the experimental data. It has been shown that the concentration dependence of the x-ray spectra corresponds to the manifestation of the significant hybridization of localized and delocalized donor electron states in the conduction band. © 2005 Pleiades Publishing, Inc.

PACS numbers: 71.55.Gs; 78.70.Dm

The aim of this work is to demonstrate the manifestation of the effects of the hybridization of electron states on an impurity of a transition d element with the states of the conduction band of a semiconductor in x-ray absorption spectra. The problem of revealing a role of such a hybridization arises when interpreting certain dependences in electron phenomena observed when impurity energy levels lie in the conduction band, which can be realized in narrow-gap and gapless semiconductors. Mercury selenide with iron impurities is a remarkable object of investigations in this field. It has been found that Fe²⁺ ions in the HgSe gapless semiconductor have a donor level at an energy of about 0.2 eV above the conduction band edge [1–3]. When, with increasing the impurity concentration n_i , the Fermi energy of conduction electrons reaches this level (at $n_i \sim 5 \times 10^{18} \text{ cm}^{-3}$), phenomena associated with such a resonance are observed. Among these phenomena are the stabilization of the electron concentration and the maximum of electron mobility with increasing the concentration of impurities above the resonance level. In many works reviewed in [4, 5], the hybridization of electron states was thought to be immaterial when explaining such phenomena. Accordingly, it was assumed that impurity ions Fe³⁺ and Fe²⁺ that respec-

tively give and do not give an electron to the conduction band coexist near the resonance. In the framework of this concept, to explain the observed dependences, one must accept an assumption that the impurity electron density is ordered [6] and other assumptions whose strict justification is difficult. At the same time, it has been shown recently [7, 8] that the main resonance effects can be consistently explained by the hybridization of electron states, which is described by the theory of the resonance scattering of conduction electrons on donor impurities. For this reason, it appears necessary to obtain or justify the absence of direct experimental evidence of hybridization. X-ray spectra of absorption on impurities can provide such evidence. It is evident that the solution to this problem concerns a wide range of systems with impurity energy levels in the conduction band.

Experiments on Fe L_3 x-ray absorption spectra were carried out at the Berkeley synchrotron (ALS) on mercury selenide with iron impurities with concentrations beginning with the resonance concentration. Iron L_3 ($2p_{3/2} \rightarrow 3d_4s$ transition) absorption spectra have been measured with an energy resolution of 0.8 eV in the total-electron yield mode.

The figure shows the resulting spectra. We first discuss the data for the maximum concentration 10^{21} cm^{-3} .

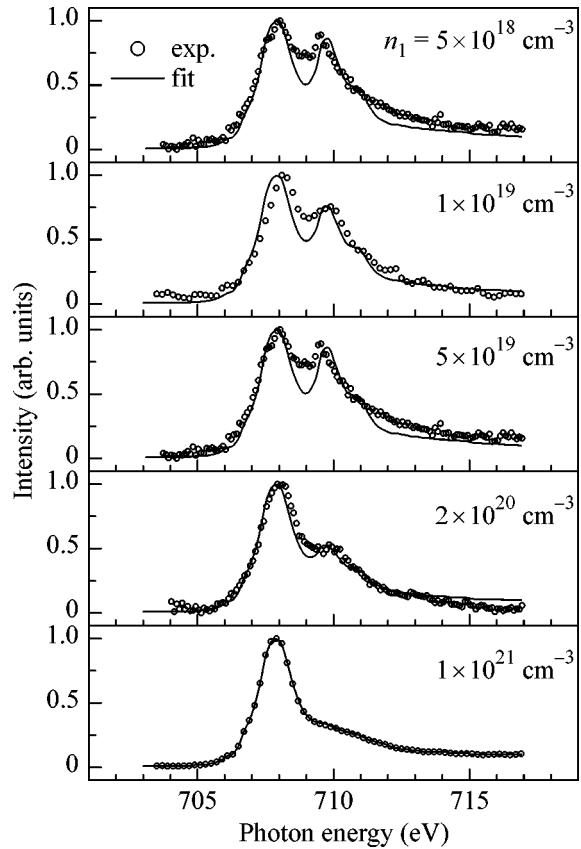
Such a concentration is two orders of magnitude higher than the resonance value. In this case, one should expect that the manifestations of electron states on impurities nearly coincide with the manifestations of bound electrons. Therefore, the spectrum observed for this concentration apparently corresponds to the Fe^{2+} ion at any possible types of states in the resonance concentration range. Such an interpretation of this spectrum is corroborated by analyzing the data of the same experiment specially carried out for the x-ray absorption on zinc selenide crystals with iron impurities with a concentration of $6 \times 10^{20} \text{ cm}^{-3}$. According to the current concepts, iron impurity ions are in the Fe^{2+} state in zinc selenide and the d energy level is located in an energy gap; i.e., it corresponds to a bound state [9].

The change in the spectrum with decreasing the impurity concentration is associated with a transition to incomplete occupation of electron states localized on impurities. If the donor state is thought to be bound, it is necessary to assume that it becomes unfilled for some impurities and remains completely filled for the remaining impurities. Therefore, the manifestations of the mixture of Fe^{2+} and Fe^{3+} ions must be observed. At the same time, the thermal ionization of impurities is insignificant at this temperature, because the stabilization of the electron concentration is manifested. In this case, the absorption intensity I for this model in the n_i impurity concentration range under consideration must be described by the formula

$$I = i_0 n_{0i} + i_1 (n_i - n_{0i}). \quad (1)$$

Here, i_0 and i_1 characterize absorption by the Fe^{3+} and Fe^{2+} ions, respectively, and n_{0i} is the Fe^{3+} ion concentration, which is equal to the conduction electron concentration n_e . The value n_e for the given samples was determined in [7] and is presented in the table (second row) with the correction made for room temperature. The relative concentration of the Fe^{3+} ions, which is determined in the bound-state model as n_{0i}/n_i , is presented in the sixth row of the table. The second term in Eq. (1) is the contribution to I from Fe^{2+} ions, the number of which is determined by the difference between n_i and n_{0i} (i.e., between the first and second rows of table).

Our aim is to determine whether the Fe^{3+} ion concentration corresponding to the observed intensity of the x-ray absorption spectra agree with the values that



Fe L_3 x-ray absorption spectra in the HgSe:Fe system. The solid lines are fitting curves. The iron impurity concentrations are given on the plots.

are predicted in the bound-state model and presented in the fifth and sixth rows of the table. To find the relative contributions of the Fe^{3+} and Fe^{2+} ions to the total absorption spectrum, we decompose the spectrum into two components thus, involving the absorption spectra of the standards for the bound states of Fe^{3+} and Fe^{2+} into the description of the shape and energy position of the partial intensities i_0 and i_1 . The aforementioned Fe L_3 absorption spectrum from the ZnSe:Fe sample with an iron concentration of $6 \times 10^{20} \text{ cm}^{-3}$ is used as the standard for Fe^{2+} . The calculated multiplet of the Fe^{3+} L_3 absorption spectrum in a tetrahedral field [10] is used as the standard for Fe^{3+} . Such a field is realized in the HgSe:Fe system. We emphasize that, if the experimen-

Table

Impurity concentration n_i , 10^{18} cm^{-3}	5	10	50	200
Conduction electron concentration n_e , 10^{18} cm^{-3}	2	2.5	3.9	5
Fe^{3+} ion concentration n_{0i} , 10^{18} cm^{-3} (experiment)	2	3.3	12.5	36
Relative Fe^{3+} ion concentration n_{0i}/n_i (experiment)	0.38	0.33	0.25	0.18
Fe^{3+} ion concentration n_{0i} , 10^{18} cm^{-3} (bound-state model)	2	2.5	3.9	5
Relative Fe^{3+} ion concentration n_{0i}/n_i (bound-state model)	0.4	0.25	0.08	0.025

tal Fe L_3 absorption spectrum from Fe_2O_3 is used instead of the calculated Fe^{3+} spectrum, the results change only slightly. Therefore, the final conclusions are insignificantly sensitive to the choice of the Fe^{3+} spectrum standard. The relative intensities of the standard contributions from the Fe^{3+} and Fe^{2+} ions vary to achieve the best approximation of the envelope of the synthesized spectrum to the experimental absorption curve. The ratio of the area under the Fe^{3+} contribution to the area of the entire spectrum is then determined from the synthesized spectrum for each concentration and presented in the table as the relative concentration of Fe^{3+} ions n_{0i}/n_i (fourth row).

The comparison of the third row with the fifth row and the fourth row with the sixth row shows that the experimental values of both the absolute and relative concentrations of the Fe^{3+} ions are inconsistent with the respective values predicted in the bound-state model. Significant excess of the absolute and relative concentrations of the Fe^{3+} ions is observed for all the intermediate compositions, and the ratio n_{0i}/n_i varies more slowly than the respective ratio predicted by the bound state model. This difference can be treated as evidence of electron localization that arises due to the hybridization of the states of the impurity and the conduction band. With the inclusion of hybridization, the formula

$$I/n_i = \alpha i_0 + (1 - \alpha) i_1 \quad (2)$$

can be written instead of Eq. (1). The right-hand side of Eq. (2) is a characteristic of the intermediate-valence state of each of the impurities that are equivalent to each other, and the coefficient α varying slowly with the concentration (the fourth row of the table) from unity (a donor electron is given to the conduction band) to zero (a donor electron is on an impurity) can be called the donor-electron hybridization coefficient. Thus, according to the data obtained in this work, the system of donor electron states of iron impurities in mercury selenide is inadequate to the set of bound states of two types and can be more adequately described as a set of states equivalent to each other. According to present knowledge, the formation of such unbound states should be treated as a result of the hybridization of electron states on impurity ions and in the conduction band.

Thus, in the experiments on x-ray absorption on iron impurities in mercury selenide crystals, we have observed a change in the electron state of the impurity with decreasing the concentration from neutral in the Fe^{2+} ion lattice to the state corresponding to the intermediate filling of the resonant donor level. Accepting the justified criterion of the existence of two types of electron bound states corresponding to the Fe^{2+} and Fe^{3+} ions near the resonance, we have demonstrated that this hypothesis contradicts the dependences observed experimentally and have thereby found evidence of the hybridization of bound and conduction states.

This work was supported by the Russian Foundation for Basic Research (project nos. 03-02-16246 and 05-02-16438) and by the Council of the President of the Russian Federation for Support of Young Russian Scientists and Leading Scientific Schools (project no. NSH-1026.2003.2).

REFERENCES

1. A. Mycielski, P. Dzwonkowski, B. Kowalski, *et al.*, *J. Phys. C: Solid State Phys.* **19**, 3605 (1986).
2. N. G. Gluzman, L. D. Sabirzyanova, I. M. Tsidil'kovskii, *et al.*, *Fiz. Tekh. Poluprovodn. (Leningrad)* **20**, 94 (1986) [*Sov. Phys. Semicond.* **20**, 55 (1986)]; *Fiz. Tekh. Poluprovodn. (Leningrad)* **20**, 1994 (1986) [*Sov. Phys. Semicond.* **20**, 1251 (1986)].
3. F. S. Pool, J. Kossut, U. Debska, and R. Reifenberger, *Phys. Rev. B* **35**, 3900 (1987).
4. Z. Wilamowski, *Acta Phys. Pol. A* **77**, 133 (1990).
5. I. M. Tsidil'kovskii, *Usp. Fiz. Nauk* **162**, 63 (1992) [*Sov. Phys. Usp.* **35**, 85 (1992)].
6. J. Mycielski, *Solid State Commun.* **60**, 165 (1986).
7. V. I. Okulov, L. D. Sabirzyanova, K. S. Sazonova, and S. Yu. Paranchich, *Fiz. Nizk. Temp.* **30**, 441 (2004) [*Low Temp. Phys.* **30**, 328 (2004)].
8. V. I. Okulov, *Fiz. Nizk. Temp.* **30**, 1194 (2004) [*Low Temp. Phys.* **30**, 897 (2004)].
9. K. I. Kikoin, *Electron Properties of Transition Element Impurities in Semiconductors* (Énergoatomizdat, Moscow, 1991) [in Russian].
10. J. P. Crocombette, M. Pollak, F. Jollet, *et al.*, *Phys. Rev. B* **52**, 3143 (1995).

Translated by R. Tyapaev

Rectification Effect in a Quantum Contact

V. A. Sablikov, V. I. Borisov, and A. I. Chmil'

*Institute of Radio Engineering and Electronics, Russian Academy of Sciences,
Fryazino, Moscow region, 141190 Russia*

e-mail: sablikov@gmail.com

Received November 4, 2004; in final form, December 22, 2004

The rectification of current has been observed in a quasi-one-dimensional ballistic quantum channel. The effect is explained by the asymmetry of the potential profile in the channel. The dependence of the rectified current on the height of the potential barrier in the channel exhibits sharp maxima, which are associated with conductance quantization steps. A model of the rectification is proposed. © 2005 Pleiades Publishing, Inc.

PACS numbers: 73.23.Ad; 73.40.Ei; 73.63.Nm

Quantum structures with asymmetric conductance (ratchets) have attracted considerable interest in recent years. One of the properties of such systems is the rectification of an alternating current [1]. The magnitude and sign of the rectified current (or voltage) and its dependence on the chemical potential are determined by both the initial asymmetry of the structure and the symmetry breaking under nonequilibrium conditions. The rectification has been studied on multiterminal ballistic structures fabricated from semiconductor heterostructures [2–6], on arrays of asymmetric electron scatterers [7, 8], and on vortices in superconductors [9, 10]. The mechanism of rectification in ballistic semiconductor structures remains poorly understood despite the seeming simplicity of the basic idea that attributes the rectification to the asymmetry of electron scattering [2]. Experiments have revealed different dependences of the effect on the potential across the electrodes and even different signs of the rectified voltage. In view of these difficulties, the role of electron–electron interaction at the level of the self-consistent field of the excess charge arising in these structures under nonlinear transport conditions is discussed [11–13]. However, the electronic structure of multiterminal mesoscopic systems is still poorly understood, and, hence, the aforementioned important effect can be taken into account only within fairly rough estimates.

In this paper, we note that the rectification effect also occurs in a much simpler structure containing only one quantum contact. Multiterminal structures contain several such contacts, which can make a considerable contribution to the effect observed in the experiment. In principle, rectification is possible when electrons pass through an asymmetric potential barrier. Such a barrier can be implemented in a relatively short quasi-one-dimensional quantum wire connecting two electron reservoirs. The potential relief in the wire is not flat due either to the charge formed in the wire [14, 15] or simply to the charge of the nearby random impurities. In

any case, the potential relief has a maximum whose position is generally asymmetric with respect to the reservoirs. We have fabricated such structures and measured the dc current component arising in them when a low-frequency alternating voltage is applied. We have found that a rectified current is observed even at low voltages and that this current exhibits sharp maxima at certain values of the gate voltages governing the electron density. Below, we describe the experiment in more detail and propose a mechanism of this effect.

Structures with a quantum channel were fabricated on the basis of selectively doped GaAs/AlGaAs heterostructures with a two-dimensional (2D) electron gas characterized by an electron concentration of $\sim 1.4 \times 10^{11} \text{ cm}^{-2}$ and an electron mobility of $\sim 3 \times 10^5 \text{ cm}^2/\text{V s}$ at 10 K. Using electron beam lithography and ion etching by a low-energy Ar^+ ion beam with subsequent elimination of the damaged layer, we fabricated transistor structures with a quasi-one-dimensional channel and side gates lying in the 2D electron gas plane. An electron microscope image of such a structure is shown in Fig. 1. The length of the channel ($\sim 0.7 \mu\text{m}$) is several times smaller than the mean free path of electrons, which is estimated as $2 \mu\text{m}$. The geometric width of the channel obtained after etching is about $0.3 \mu\text{m}$. In the normal state, the channel is usually blocked likely due to the charge adsorbed on the surfaces. When a positive potential is applied to the gates, the channel is open. In this case, characteristic quantization plateaus appear in the dependence of conductance G on the gate voltage V_g (Fig. 2a). The conductance was measured using a small alternating voltage (with an amplitude of 50–150 μV and a frequency of 130 Hz), which was applied without any dc bias. In addition, the dc current component \bar{j} was measured. As is seen in Fig. 2b, the dc current exhibits sharp maxima at the points where V_g corresponds to the values of G close to a half-integer number of the quantum $2e^2/h$.

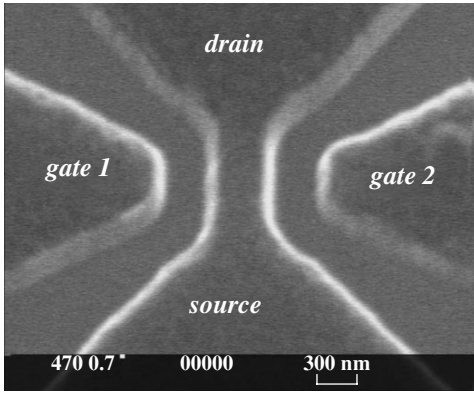


Fig. 1. Electron microscope image of a structure with a quantum channel and side gates. The light strips are the edges of the regions filled with the electron gas.

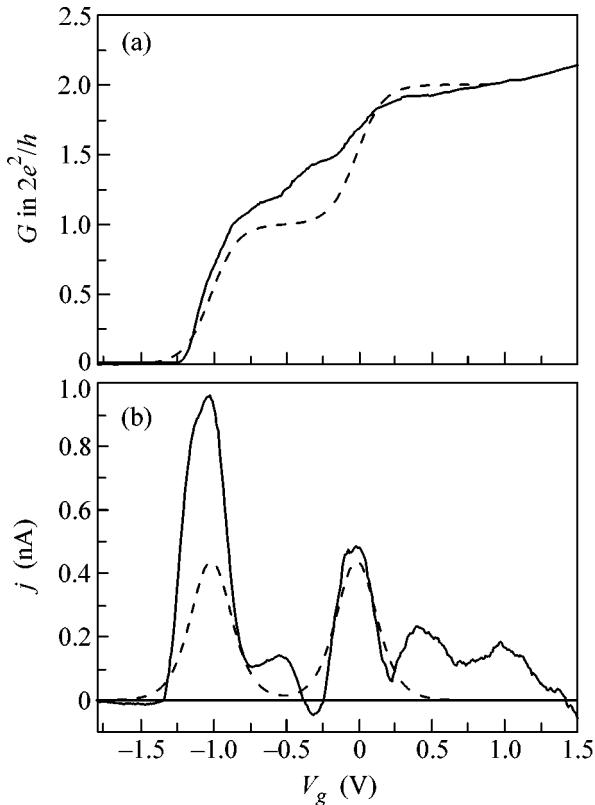


Fig. 2. (a) Conductance and (b) rectified current vs. the gate voltage at a temperature of 4.2 K. The solid lines represent the experimental data, and the dashed lines, the calculation according to the model with two subbands and with the use of the following parameters: $\beta = 0.8$, $\Delta = 0.05$ meV, $V = 0.3$ mV, and an intersubband energy of 4 meV.

The rectification effect can be explained as follows. We assume that the potential relief in the quantum channel is nonuniform and has a maximum whose position is asymmetric with respect to the electron reser-

voirs (Fig. 3). An alternating voltage $V(t) = V\sin(\omega t)$ is applied to the reservoirs. The potential of the left-hand reservoir is assumed to be fixed, and the potential of the right-hand reservoir oscillates with the amplitude V . The electrochemical potential μ_R in this reservoir varies similarly, while the barrier height varies with a smaller amplitude βeV , where β is the standard phenomenological parameter [16, 17], which ranges from 0 to 1 and indicates the applied-voltage fraction of the voltage that drops between the source and the maximum of the potential relief. If the equilibrium level of the chemical potential μ is close to the maximum of the unperturbed potential relief u_m within the band $\pm eV\max[\beta, (1 - \beta)]$, there is an asymmetry in the electron transport from left to right and vice versa. If $\beta \neq 1/2$, the electrons from one reservoir (the left-hand one in Fig. 3) are blocked by the barrier for a longer time as compared to the electrons from the other reservoir. This is the case where the rectification of current occurs.

The quantity β is determined by both the geometric asymmetry of the structure [16] (when the bottleneck of the quantum constriction is closer to one of the reservoirs) and the charge arising in the quantum channel under dc bias. Owing to this charge, the maximum of the potential relief is shifted to one of the reservoirs even in a symmetric structure [14, 18].

Let us find the magnitude of the rectified current using the standard Landauer–Büttiker approach disregarding the effects of electron–electron interaction. This approach gives a qualitatively correct description of conductance quantization [19, 20] but does not explain the fine structure of the conductance quantization steps such as $0.7(2e^2/h)$ feature, which is associated with electron–electron interaction. The calculation on the basis of the Landauer–Büttiker approach is useful to demonstrate the rectification effect and to determine the behavior of the current as a function of the chemical potential, temperature, and barrier shape. The deviation from these dependences in the experiment would be an instrument for studying the shape of the potential relief in the structure and the effect of the electron–electron interaction.

The current through the barrier is determined by the partial currents from the left-hand and right-hand reservoirs:

$$j(t) = \frac{2e}{h} \sum_n \int_0^\infty d\varepsilon f(\varepsilon) \{ T_n[\varepsilon - u_n^{(m)} + \beta eV(t)] - T_n[\varepsilon - u_n^{(m)} - (1 - \beta)eV(t)] \}, \quad (1)$$

where ε is the electron energy measured from the bottom of the conduction band in the left-hand reservoir for the electrons moving rightwards and in the right-hand reservoir for the electrons moving leftwards, $f(\varepsilon)$ is the Fermi distribution function, and $T_n(\varepsilon - u)$ is the electron transmission coefficient through the barrier in

the n th subband. The quantity T_n is considered as a function of the energy measured from the maximum potential in the respective subband. In the case of the parabolic approximation of the barrier shape $u(x) \sim [u_n^{(m)} - m\omega_x^2(x - x_n)^2/2]$, the electron transmission coefficient is given by

$$T_n(\varepsilon - u) = [1 + \exp\{-(\varepsilon - u)/\Delta\}]^{-1},$$

where $\Delta = \hbar\omega_x/2\pi$.

For simplicity, the following consideration is performed for the current in a single subband. The rectified current

$$\bar{j} = \int_0^{2\pi} \frac{d(\omega t)}{2\pi} j(t)$$

can be represented in the form

$$\begin{aligned} \bar{j} = & \frac{2e^2V^2}{\pi h} \int_0^\infty d\varepsilon \left(-\frac{\partial f}{\partial \varepsilon} \right) \int_0^1 d\xi q(\xi) \\ & \times \{ \beta^2 [T_n'(\varepsilon - u_n^{(m)} + \beta V\xi) + T_n'(\varepsilon - u_n^{(m)} - \beta V\xi)] \\ & - (1 - \beta)^2 [T_n'(\varepsilon - u_n^{(m)} + (1 - \beta)V\xi) \\ & + T_n'(\varepsilon - u_n^{(m)} - (1 - \beta)V\xi)] \}, \end{aligned} \quad (2)$$

where $q(\xi) = \sqrt{1 - \xi^2} - \xi \arccos(\xi)$ and $T_n'(\varepsilon) = dT_n/d\varepsilon$.

The simplest result is obtained for zero temperature and an extremely smooth barrier ($T = \Delta = 0$) when the distribution function and the tunnel transparency are step functions of the energy. Then, Eq. (2) yields

$$\bar{j} = \frac{2e^2V}{\pi h}$$

$$\times \{ \beta [q(\xi_1)\theta(\xi_1)\theta(1 - \xi_1) + q(-\xi_1)\theta(-\xi_1)\theta(1 + \xi_1)] \quad (3)$$

$$- (1 - \beta) [q(\xi_2)\theta(\xi_2)\theta(1 - \xi_2) + q(-\xi_2)\theta(-\xi_2)\theta(1 + \xi_2)] \},$$

where $\xi_1 = (\mu - u_n^{(m)})/\beta V$ and $\xi_2 = (\mu - u_n^{(m)})/(1 - \beta)V$. The resulting dependence of the rectified current on the chemical potential is shown in Fig. 4a. The current $\bar{j}(\mu)$ is nonzero within the band $|\mu - u_n^{(m)}| \leq eV \max[\beta, (1 - \beta)]$. The maximum current $\bar{j} = (2e^2V/h)(2\beta - 1)/\pi$ is reached at $\mu = u_n^{(m)}$, and the shape of the peak is described by the function $q(\xi)$.

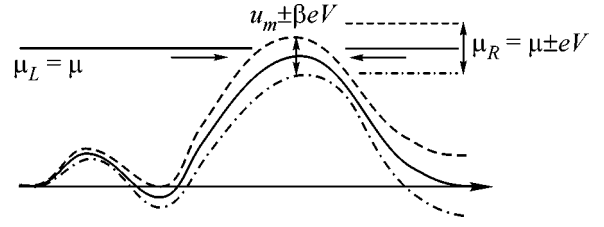


Fig. 3. Potential relief in the quantum channel for the cases of (solid line) zero, (dashed line) negative, and (dot-dashed line) positive bias applied to the right-hand reservoir. In the case of a negative bias, the electrons of the left-hand reservoir are blocked by the barrier and the electrons from the right-hand reservoir pass over the barrier.

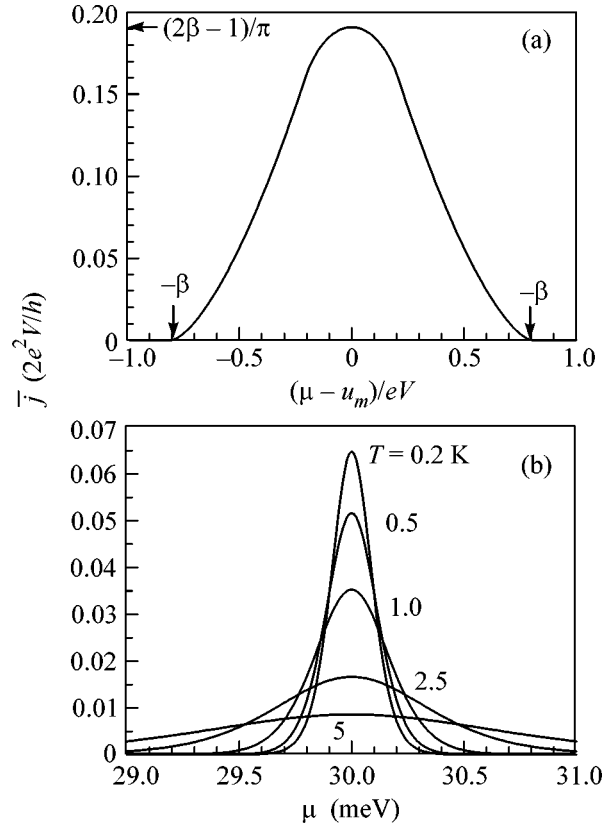


Fig. 4. Rectified current vs. μ calculated for (a) zero temperature and a sharp tunnel edge, $\Delta = T = 0$ and $\beta = 0.8$, and (b) temperatures from 0.2 to 5 K at $V = 0.1$ mV, $\Delta = 0.05$ meV, $u_n^{(m)} = 30$ meV, and $\beta = 0.8$.

At a finite temperature and $\Delta \neq 0$, the peak of the function $\bar{j}(\mu)$ is broadened to a width of about $\max[T, \Delta]$ and decreases in height. The maximum value of \bar{j} is reached at $\mu = u_n^{(m)}$ as before. The results of calculating the rectified current by Eq. (2) for different temperatures are presented in Fig. 4b.

If $\Delta \ll T$, the dependence of the maximum current on the voltage amplitude and temperature is described by the expressions

$$\bar{j}_m \approx \frac{2e^2(2\beta - 1)V}{\pi h} \times \begin{cases} \frac{eV}{T} - \frac{\beta^2 + (1 - \beta)^2}{32} \left(\frac{eV}{T}\right)^3 + \dots, & \frac{eV}{T} \ll 1; \\ 1 - \frac{\pi^2}{6\beta(1 - \beta)} \left(\frac{T}{eV}\right)^2 + \dots, & \frac{T}{eV} \ll 1. \end{cases}$$

Hence, when the voltage is low ($eV \ll T$), the rectified current is proportional to the voltage squared, and when $eV \gg T$, the rectification effect is linear in V . The maximum rectified current is of the same order of magnitude as the alternating current. An increase in temperature leads to a decrease in the rectified current asymptotically as $\sim T^{-1}$.

The current decreases similarly with an increase in the tunneling parameter Δ in the other limiting case of $\Delta \gg T$.

The direction of the current depends on the position of the maximum of the potential relief: electrons are transferred to the reservoir that is farthest from this maximum. The aforementioned peaks of the rectified current as a function of μ must evidently arise when the chemical potential level approaches the bottoms of the dimensional quantization subbands in the transverse direction.

The rectification mechanism is closely associated with the nonlinear current–voltage characteristic, which is strongest when the chemical potential level is close to the maximum of the potential relief. The parameters that determine the nonlinearity of the current–voltage characteristic are T and Δ . For a small voltage $eV \ll \max[T, \Delta]$, the expression for the rectified current can be obtained from Eq. (1) by expanding it in voltage:

$$j \approx V \frac{2e^2}{h} \int d\varepsilon f(\varepsilon) T'(\varepsilon - u) + \frac{(eV)^2 2e}{2h} (2\beta - 1) \int d\varepsilon f(\varepsilon) T''(\varepsilon - u) + \dots$$

Averaging over time and taking into account that the maximum of the potential relief u depends on the gate voltage V_g , we arrive at the following relation between \bar{j} and the conductance G :

$$\bar{j} \approx eV^2 \frac{2\beta - 1}{2} \frac{dG}{dV_g} \frac{du}{dV_g}. \quad (4)$$

From this expression, one can see that the current \bar{j} as a function of the gate voltage becomes maximal when V_g takes the values corresponding to the fastest growth of conductance with V_g . In the regime described by Eq. (4), the rectification effect is quadratic in voltage V .

If the applied voltage V is not small compared to $\max[T, \Delta]$, the expansion in V is impossible and the rectified current is described by more general formulas (2) and (3). In this case, \bar{j} varies linearly with V .

These laws describing the rectification of current agree qualitatively with the experiment. As the gate voltage is varied, a sequence of peaks of current are observed. The positions of the peaks correlate with changes in the conductance. At the points of the maximum current, the conductance is close to half-integer numbers multiplied by $2e^2/h$, which corresponds to the points where the subband bottoms intersect the chemical potential level [21]. With increasing temperature, the height of the peaks of the current decreases rapidly. Figure 2 shows the results of the calculations for the conductance and the rectified current. As is seen, they agree well with the experiment. A detailed quantitative comparison between the theory and experiment was impossible, because the quality of the samples under investigation was insufficient: the mobility of the electrons and their density in the 2D electron gas were relatively low. These causes gave rise to mesoscopic fluctuations distorting the conductance quantization pattern. Such a distortion is stronger for longer quantum wires. For structures with parameters close to those of our samples, the critical channel length distorting the quantization is estimated as $\sim 0.5 \mu\text{m}$ [22]. A channel with a length of $\sim 0.7 \mu\text{m}$ is used in our study because an asymmetric barrier is easily realized (randomly) in a sufficiently long channel.

As one can see from Fig. 2, the parameters of the model used by us can be chosen so as to obtain a qualitatively correct description of the two main sharp maxima of the current $\bar{j}(V_g)$ observed experimentally. However, it is difficult to fit the maximum value of the current to the experiment. In the experiment, the current proves to be much higher than in the theory (the theoretical curves twofold overestimate the voltage amplitude). The discrepancy between the theory and experiment for the first maximum is noticeably greater than the corresponding discrepancy for the second maximum.

The deviation of the current observed in the experiment from the calculated values may be attributed to the disregarded effects of the electron–electron interaction, which are strongest before the first plateau of the quantum wire conductance quantization, where the electron density is small. At present, these effects are being intensively investigated, and their study with the use of the rectification effect seems to be rather promising. In view of these circumstances, it is necessary to carry out measurements on higher-quality structures. In

addition, the rectification effect provides information on asymmetry that is initially present in the structure or appears under highly nonequilibrium conditions. The presence of the rectified current (and voltage) component may be important for analyzing the conductance quantization steps when the contact resistance is considerable.

This work was supported by the Russian Foundation of Basic Research (project no. 02-02-16953); the programs “Low-Dimensional Quantum Structures” and “Strongly Correlated Electrons in Semiconductors, Metals, Superconductors, and Magnetic Materials,” Russian Academy of Sciences; the programs of the Ministry of Education and Science of the Russian Federation; and the program “Integration” (grant no. I02908/1040). We are grateful to A.I. Toropov for placing heterostructures containing 2D electron gas at our disposal. The low-temperature measurements were performed at the Institute of Solid State Physics, Russian Academy of Sciences.

REFERENCES

1. P. Reimann, *Phys. Rep.* **361**, 57 (2002).
2. A. M. Song, A. Lorke, A. Kriele, *et al.*, *Phys. Rev. Lett.* **80**, 3831 (1998).
3. A. M. Song, *Phys. Rev. B* **59**, 9806 (1999).
4. A. Löfgren, C. A. Marlow, I. Shorubalko, *et al.*, *Phys. Rev. Lett.* **92**, 046803 (2004).
5. S. de Haan, A. Lorke, J. P. Kotthaus, *et al.*, *Phys. Rev. Lett.* **92**, 056806 (2004).
6. M. G. Vavilov, L. DiCarlo, and C. M. Marcus, *cond-mat/0410042* (2004).
7. H. Linke, T. E. Humphrey, A. Löfgren, *et al.*, *Science* **286**, 2314 (1999).
8. A. Löfgren, I. Shorubalko, P. Omling, *et al.*, *Phys. Rev. B* **67**, 195309 (2003).
9. J. B. Majer, J. Peguiron, M. Grifoni, *et al.*, *Phys. Rev. Lett.* **90**, 056802 (2003).
10. A. V. Ustinov, C. Coqui, A. Kemp, *et al.*, *Phys. Rev. Lett.* **93**, 087001 (2004).
11. R. Fleischmann and T. Geisel, *Phys. Rev. Lett.* **89**, 016804 (2002).
12. M. Büttiker and D. Sánchez, *Phys. Rev. Lett.* **90**, 119701 (2003).
13. T. Geisel and R. Fleischmann, *Phys. Rev. Lett.* **90**, 119702 (2003).
14. V. A. Sablikov, S. V. Polyakov, and M. Büttiker, *Phys. Rev. B* **61**, 13763 (2000).
15. V. A. Sablikov and B. S. Shchamkhalova, *Physica E (Amsterdam)* **17**, 189 (2003).
16. L. P. Kouwenhoven, B. J. van Wees, C. J. P. M. Harmans, *et al.*, *Phys. Rev. B* **39**, 8040 (1989).
17. L. Martín-Moreno, J. T. Nicholls, N. K. Patel, *et al.*, *J. Phys. C* **4**, 1323 (1992).
18. B. S. Shchamkhalova and V. A. Sablikov, *Physica E (Amsterdam)* (in press).
19. L. I. Glazman, G. B. Lesovik, D. E. Khmel'nitskiĭ, and R. I. Shekhter, *Pis'ma Zh. Éksp. Teor. Fiz.* **48**, 218 (1988) [*JETP Lett.* **48**, 238 (1988)].
20. L. I. Glazman and A. V. Khaetskiĭ, *Pis'ma Zh. Éksp. Teor. Fiz.* **48**, 546 (1988) [*JETP Lett.* **48**, 591 (1988)].
21. M. Büttiker, *Phys. Rev. B* **41**, 7906 (1990).
22. J. A. Nixon, J. H. Davies, and H. U. Baranger, *Phys. Rev. B* **43**, 12638 (1991).

Translated by E. Golyamina

Quantum Dimer Model for Trimerized Kagomé Antiferromagnet[†]

M. E. Zhitomirsky

Commissariat à l'Energie Atomique, DSM/DRFMC/SPSMS, 38054 Grenoble, France

e-mail: zhitomir@drfmc.ceng.cea.fr

Received December 22, 2004

Low-energy singlet states of a spin-1/2 trimerized kagomé antiferromagnet are mapped to an effective quantum dimer model on a triangular lattice. The mapping is done in the first-order of perturbation theory in a weaker coupling constant of the trimerized model. The derived quantum dimer model is dominated by kinetic energy terms (dimer resonances) on a few shortest loops of the triangular lattice. © 2005 Pleiades Publishing, Inc.

PACS numbers: 75.10.Jm; 75.50.Ee

The resonating valence bond (RVB) state introduced by Anderson and colleagues a long time ago [1] is nowadays a popular paradigm in condensed matter physics. Short-range RVB states are considered to be probable candidates for an elusive spin-liquid phase of magnetic insulators. On a quantitative level, the idea of short-range RVB states is formulated by so-called quantum dimer models (QDM) [2–4]. In QDMs, each dimer represents a singlet state (valence bond) between a pair of neighboring spins. The QD Hamiltonian is defined on the Hilbert space of close-packed dimer coverings of a lattice. The dimer states are assumed to be properly orthogonalized. The local dynamics of an RVB state are typically described using only the smallest plaquettes (\square), which are squares (square lattices) or rhombi (triangular lattices):

$$\hat{\mathcal{H}}_{\text{QD}} = \sum_{\square} [-t(|\square\rangle\langle|\square| + |\square\rangle\langle|\square|) + V(|\square\rangle\langle|\square| + |\square\rangle\langle|\square|)]. \quad (1)$$

The first term is the dimer kinetic energy, which flips a pair of parallel dimers around an arbitrary plaquette; the second term is the potential energy between such pairs. Rokhsar and Kivelson [3] have shown that a short-range RVB state given by a superposition of all dimer coverings of a square lattice is an exact eigenstate of the QD Hamiltonian for a special choice of the parameters $t = V$. On a bipartite square lattice, the RVB state at the Rokhsar–Kivelson (RK) point has long-range power law correlations and consequently describes a gapless spin-liquid state [3, 5]. The small perturbations away from the RK point will drive the system into one of the ordered crystalline dimer states. The QDM on a triangular lattice exhibits a quite differ-

ent behavior at the RK point [5–7]. The short-range RVB state has exponentially decaying correlators and, therefore, should be stable with respect to deviations from the RK point or on switching on extra perturbations to the QD Hamiltonian. Still, the question whether such states or Hamiltonians can describe realistic quantum spin systems remains to a large extent unsettled. In the present work we discuss a realization of QDM on a triangular lattice.

The most probable candidates for a singlet spin-liquid ground state are frustrated quantum antiferromagnets [8]. Numerical exact diagonalization studies of a spin-1/2 Heisenberg kagomé antiferromagnet have shown that this spin model has a nonmagnetic ground state with a large number of low-lying singlet excitations [9, 10]. The available cluster sizes do not allow us to draw a definite conclusion on the possible nature of the singlet ground state.

One of very few analytic approaches to such problems is a strong-coupling expansion from small clusters. The main motif of a kagomé lattice is a triangle. It is, therefore, natural to start from a trimerized kagomé lattice, which is shown in Fig. 1. Such a strong-coupling approach was pursued in relation to kagomé antiferromagnets in several theoretical works [11–14]. Recently, an experimental scheme to create a trimerized kagomé lattice was suggested for ultracold atomic gases in optical traps [15]. This opens a possibility for an experimental check of RVB physics in the corresponding spin model.

The Heisenberg model on a trimerized lattice

$$\hat{\mathcal{H}} = \sum_{\langle ij \rangle} J_{ij} \mathbf{S}_i \cdot \mathbf{S}_j \quad (2)$$

is described by two coupling constants: J_1 for a stronger interaction between spins in \triangle triangles and J_2 for a weaker interaction inside ∇ triangles. An array of iso-

[†]This article was submitted by the author in English.

lated \triangle triangles is a zeroth order Hamiltonian, which has a highly degenerate ground state. Interactions between \triangle triangles should lift such a degeneracy even in the first-order of perturbation theory.

In the beginning, let us derive the previous results on the effective first-order Hamiltonian [11–13] using somewhat different notations. One starts with an isolated triangle. Its Hamiltonian is

$$\begin{aligned}\hat{\mathcal{H}}_{\triangle} &= J_1(\mathbf{S}_1 \cdot \mathbf{S}_2 + \mathbf{S}_2 \cdot \mathbf{S}_3 + \mathbf{S}_3 \cdot \mathbf{S}_1) \\ &= \frac{J_1}{2}(\mathbf{S}_1 + \mathbf{S}_2 + \mathbf{S}_3)^2 - \frac{3}{2}J_1S(S+1).\end{aligned}\quad (3)$$

The energy levels are determined by the total spin. For $S = 1/2$, which is always assumed below, the levels are

(i) two doublets with $S = 1/2$ and $E = -\frac{3}{4}J_1$ and (ii) one

quartet with $S = 3/2$ and $E = \frac{3}{4}J_1$. In the lowest order of a perturbation expansion in J_2/J_1 , one can neglect states with $S = 3/2$, which are separated from the lowest doublets by a finite gap $\Delta E = \frac{3}{2}J_1$. The two degenerate states with $S = 1/2$ and $S^z = 1/2$ are

$$\begin{aligned}|d_{\uparrow}\rangle &= \frac{1}{\sqrt{2}}(\uparrow\uparrow\downarrow - \uparrow\downarrow\uparrow), \\ |p_{\uparrow}\rangle &= \frac{1}{\sqrt{6}}(2\downarrow\uparrow\uparrow - \uparrow\uparrow\downarrow - \uparrow\downarrow\uparrow),\end{aligned}\quad (4)$$

where $|d_{\uparrow}\rangle$ is a combination of the spin-up apex spin and a singlet bond between the two base spins (Fig. 1). Spin-down states $|d_{\downarrow}\rangle$ and $|p_{\downarrow}\rangle$ are obtained from the spin-up states (4) by acting with S^- operator. The choice of the basis is, of course, not unique. The apex spin can be instead put into a singlet state either with its right or left neighbor, which yields two other states $|d'_{\uparrow}\rangle = \frac{1}{\sqrt{2}}(\downarrow\uparrow\uparrow - \uparrow\uparrow\downarrow)$ and $|d''_{\uparrow}\rangle = \frac{1}{\sqrt{2}}(\uparrow\downarrow\uparrow - \downarrow\uparrow\uparrow)$ with the appropriate orthogonal partners $|p'_{\uparrow}\rangle$ and $|p''_{\uparrow}\rangle$. The transformation from the old basis (4) to the new states is given by

$$\begin{aligned}|d'_{\alpha}\rangle &= -\frac{1}{2}|d_{\alpha}\rangle + \frac{\sqrt{3}}{2}|p_{\alpha}\rangle, & |p'_{\alpha}\rangle &= -\frac{\sqrt{3}}{2}|d_{\alpha}\rangle - \frac{1}{2}|p_{\alpha}\rangle, \\ |d''_{\alpha}\rangle &= -\frac{1}{2}|d_{\alpha}\rangle - \frac{\sqrt{3}}{2}|p_{\alpha}\rangle, & |p''_{\alpha}\rangle &= \frac{\sqrt{3}}{2}|d_{\alpha}\rangle - \frac{1}{2}|p_{\alpha}\rangle,\end{aligned}\quad (5)$$

where $\alpha = \uparrow, \downarrow$ is a spinor index. The main difference with the previous works [11, 12] is that we use real basis states (4) or (5) instead of defining complex chiral states. This yields a more transparent form of the first-order Hamiltonian and simplifies the subsequent derivation of a QDM.

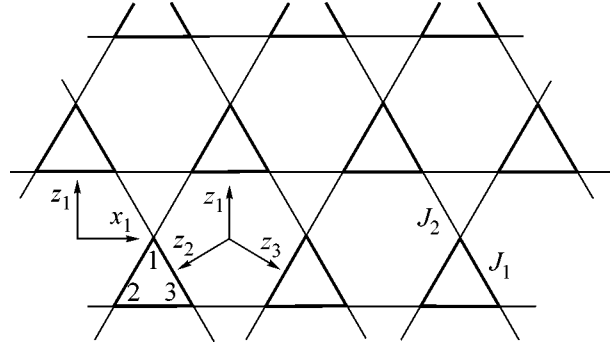


Fig. 1. Trimerized kagomé lattice with two exchange constants. The indicated labeling of sites and axes is used in the text.

At this point, we introduce two sets of the Pauli matrices: σ^i , which act between the spin-up and spin-down states, and τ^i , which act in the orbital subspace (d, p) preserving the total spin. The convenient choice of orbital axes shown in Fig. 1 corresponds to

$$\tau^{z_1}|d_{\alpha}\rangle = |d_{\alpha}\rangle, \quad \tau^{z_1}|p_{\alpha}\rangle = -|p_{\alpha}\rangle. \quad (6)$$

Then, the orbital operators projected onto the rotated axes

$$\tau^{z_2} = -\frac{1}{2}\tau^{z_1} - \frac{\sqrt{3}}{2}\tau^{x_1} \quad \text{and} \quad \tau^{z_3} = -\frac{1}{2}\tau^{z_1} + \frac{\sqrt{3}}{2}\tau^{x_1}$$

yield $\tau^{z_2}|d'_{\alpha}\rangle = |d'_{\alpha}\rangle$ and $\tau^{z_3}|d''_{\alpha}\rangle = |d''_{\alpha}\rangle$ and so on.

In order to find the effect of coupling J_2 between the triangular blocks, we have to calculate the matrix elements of the on-site spin operators between the basis states $|d_{\alpha}\rangle$ and $|p_{\alpha}\rangle$. This problem is greatly simplified once all the symmetries are taken into account. The final result is

$$\mathbf{S}_1 = \frac{1}{2}d_{\alpha}^{\dagger}\boldsymbol{\sigma}_{\alpha\beta}d_{\beta} - \frac{1}{6}p_{\alpha}^{\dagger}\boldsymbol{\sigma}_{\alpha\beta}p_{\beta}, \quad (7)$$

$$\mathbf{S}_{2,3} = \frac{1}{3}p_{\alpha}^{\dagger}\boldsymbol{\sigma}_{\alpha\beta}p_{\beta} \pm \frac{1}{2\sqrt{3}}(p_{\alpha}^{\dagger}\boldsymbol{\sigma}_{\alpha\beta}d_{\beta} + \text{h.c.}).$$

The spinor structure is a consequence of the spin-rotational symmetry, while the permutation symmetry P_{23} fixes the orbital part in (7). The above representation is further simplified once the total spin of a triangle $\mathbf{S} = \frac{1}{2}\boldsymbol{\sigma}$ is defined and the orbital operators τ^{z_k} are used. Then, the n th spin ($n = 1, 2, 3$) of the i th triangular block is represented by

$$\mathbf{S}_{ni} = \frac{1}{3}\mathbf{S}_i(1 + 2\tau_i^{z_n}), \quad (8)$$

where $\hat{\mathbf{z}}_n$ goes from the center of a triangle in the direction of the corresponding spin (see Fig. 1).

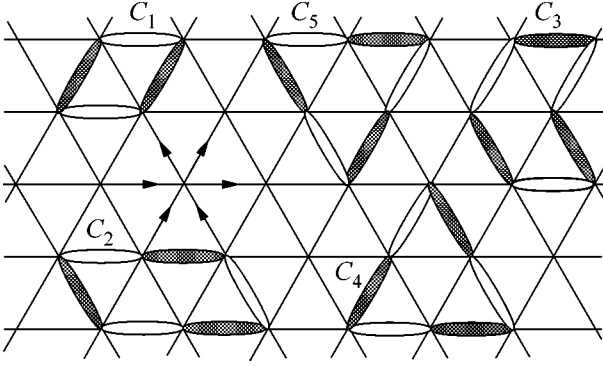


Fig. 2. Effective triangular lattice with five shortest loops. The arrow direction indicates a sign convention for the singlet wave-function on each bond.

The effective Hamiltonian of the first order in a weaker coupling J_2 is found by substituting Eq. (8) into the Hamiltonian (2):

$$\hat{\mathcal{H}}_1 = \frac{J_2}{9} \sum_{\langle ij \rangle} \mathbf{S}_i \cdot \mathbf{S}_j (1 + 2\tau_i^{z_n})(1 + 2\tau_j^{z_m}), \quad (9)$$

where a trivial constant term $-\frac{3}{4}J_1N_\Delta$ is omitted for

convenience. The derived spin-orbital Hamiltonian $\hat{\mathcal{H}}_1$ is defined on a triangular lattice such that every site corresponds to one Δ block of the trimerized kagomé model and is attributed with spin and orbital operators. The bond orientation uniquely determines the orbital axes for two participating sites. In the following, we drop the common energy factor J_2 , which is the same for all the results obtained in the first-order perturbation theory.

The search for the low-energy states of Hamiltonian (9) can be approached from a two-site problem (two adjacent Δ triangles of the original kagomé lattice) [12]. This problem is solved exactly and its ground state corresponds to a spin singlet with the orbital degrees fully polarized along the bond: $\langle \tau_i^{z_n} \rangle = \langle \tau_j^{z_m} \rangle = 1$. The ground-state energy is $-3/4$. A variational solution for the lattice problem (9) is constructed by splitting the whole lattice into a close-packed structure of dimers between nearest-neighbor sites such that the dimer wave-function is given by the ground-state solution of the two-site problem. A remarkable feature of these variational states is that, at the mean-field level with respect to the orbital degrees of freedom, the total energy is just a sum of energies of individual dimers and does not depend on a particular dimer covering of a triangular lattice [12]. Indeed, once $\langle \tau_i^{z_n} \rangle = 1$, then, for the two other axes, $\langle \tau_i^{z_m} \rangle = \langle \tau_j^{z_k} \rangle \equiv -\frac{1}{2}$. Therefore, the expectation value of any empty bond, i.e., a bond with-

out a dimer, identically vanishes over the variational wave-function: either one or both sites of the bond have $\langle \tau_i^{z_m} \rangle = -1/2$.

In [12, 16] the degenerate set of variational mean-field states has been identified with low energy states of spin-1/2 antiferromagnets on trimerized and isotropic kagomé lattices. The number of low-lying singlets of the kagomé model scales are then, as 1.15^N , in good agreement with the full exact diagonalization study [10]. The previous works leave off, however, without answering the following questions: (i) how good is the mean-field approximation? (ii) does the true singlet ground state break certain symmetries of the lattice? (iii) is there a finite gap between the ground state and the first excited singlet levels? We shall address these problems in the following text.

In order to go beyond the mean-field approximation, one has to consider the off-diagonal matrix elements of Hamiltonian (9) between various dimer configurations as well as the corresponding overlap matrix. The general rule to compute the overlap matrix for models, where every dimer represents a singlet pair, is to construct the transition or overlap graph by drawing two dimer configurations on the same lattice [2]. Every closed nonintersecting loop of dimers contributes $2/2^{l/2}$ to the overlap matrix, l being the length of the loop. The sign of the overlap matrix element depends on the sign convention for singlet wave-functions. We adopt the standard convention such that the singlet bond wave-function is $[ab] = \frac{1}{\sqrt{2}}(\uparrow_a \downarrow_b - \downarrow_a \uparrow_b)$, where b is an upper site in the pair or is directly to the right from a (see Fig. 2).

To study the local dynamics of the valence bonds in the trimerized kagomé model, it is natural to select a few shortest loops on an effective triangular lattice shown in Fig. 2. Taking into account the orbital part of the wave functions, the overlaps of two dimer configurations on each loop are calculated as $c_1 = -1/2^4$, $c_2 = c_3 = -1/2^7$, $c_4 = -1/2^8$, and $c_5 = 1/2^5$. These overlap matrix elements are significantly smaller than for the singlet bond configurations on the original triangular lattice. In the latter case, the corresponding loops have $c_1 = 1/2$, $c_2 = c_3 = 1/2^2$, and $c_4 = c_5 = -1/2^2$. The difference reflects the fact that the loops on an effective triangular lattice correspond to significantly longer loops on the original trimerized kagomé lattice. Note also that loops C_4 and C_5 are different for the considered model because the trimerized kagomé lattice has only a three-fold rotation axis in the center of every triangle. Comparison of the overlap matrix elements explains why the QDM is a poor approximation for a spin-1/2 Heisenberg antiferromagnet on a triangular lattice but might be a good one for the trimerized kagomé model.

In [3], the derivation of QDM from a particular spin Hamiltonian has been formulated in a general form via

calculation of the inverse square root of the overlap matrix. The actual calculations can be performed more straightforwardly by operating with the wave functions. The final result are, of course, equivalent in both approaches. Specifically, let us consider two linearly independent normalized states $|\psi_1\rangle$ and $|\psi_2\rangle$ that have a small (real) overlap $\langle\psi_1|\psi_2\rangle = c$. The matrix elements of the Hamiltonian between the two states are assumed to be known: $E_{11} = \langle\psi_1|\hat{H}|\psi_1\rangle$, $E_{12} = E_{21} = \langle\psi_1|\hat{H}|\psi_2\rangle$, and $E_{22} = \langle\psi_2|\hat{H}|\psi_2\rangle$. The aim is to compute the matrix elements in a new properly orthogonalized basis $|\phi_n\rangle$. We write for this

$$|\phi_{1,2}\rangle = \lambda(|\psi_{1,2}\rangle - \mu|\psi_{2,1}\rangle) \quad (10)$$

and demand that $\langle\phi_1|\phi_2\rangle = 0$, $\langle\phi_1|\phi_1\rangle = \langle\phi_2|\phi_2\rangle = 1$.

This yields

$$\mu = \frac{c}{1 + \sqrt{1 - c^2}}, \quad \lambda^2 = \frac{1}{1 + \mu^2 - 2\mu c}. \quad (11)$$

Now, calculating the matrix elements between the new states and assuming $E_{11} = E_{22}$, for simplicity, we find

$$\begin{aligned} \tilde{E}_{11} &= E_{11} + \frac{c}{1 - c^2}(cE_{11} - E_{12}), \\ \tilde{E}_{12} &= E_{12} + \frac{c}{1 - c^2}(cE_{12} - E_{11}). \end{aligned} \quad (12)$$

Since $|c| \ll 1$, one can safely neglect c^2 in the denominators and also use $\mu \approx c/2$.

Returning back to model (9), let us explicitly write the wave-functions of the two dimer configurations for the shortest loop C_1 while numbering the sites counter-clockwise starting from the left lower vertex:

$$\begin{aligned} |\psi_1\rangle &= [12][43]|d_1d'_2d'_3d_4\rangle, \\ |\psi_2\rangle &= [32][41]|d'_1d'_2d'_3d''_4\rangle. \end{aligned} \quad (13)$$

Here, the first part of $|\psi_{1,2}\rangle$ is given by a product of two spin singlet states, while the second part is an orbital wave-function represented as a product of states (4) or (5) such that every site is in fully polarized orbital states along one of the \hat{z}_n axes. An explicit calculation gives for the diagonal matrix element a sum of two dimer energies $E_{11} = \langle\psi_1|\hat{H}_1|\psi_1\rangle = \langle\psi_2|\hat{H}_1|\psi_2\rangle = -3/2$, while the off-diagonal matrix element is $E_{12} = \langle\psi_2|\hat{H}_1|\psi_1\rangle = 9/64$. Substituting the above values into Eq. (12), we obtain for the properly orthogonalized basis

$$\tilde{E}_{11} = -\frac{3}{2} + \frac{3}{2^{10}} \equiv E_{\text{MF}} + V, \quad \tilde{E}_{12} = \frac{3}{2^6} \equiv -t. \quad (14)$$

The off-diagonal matrix element \tilde{E}_{12} is identified with the kinetic energy term in the corresponding QDM Hamiltonian. It amounts to less than 5% of the coupling

constant J_2 . The diagonal matrix element \tilde{E}_{11} is split into the mean-field energy $E_{\text{MF}} = -3/2$ and an excess part determined by quantum fluctuations. This excess part is present only if two parallel dimers occupy an elementary plaquette and should be identified with the potential energy V of QDM. The ratio of the potential energy to the kinetic term constant is very small $V/|t| = 1/16$. Note that $t < 0$ in the above calculation. As was noted in [3, 5], the sign of t is a matter of convention. A gauge transformation from real wave-functions used to calculate Eq. (14) for complex wave-functions with appropriately chosen phase factors leads to $t \rightarrow -t$ (see below).

Since the potential energy V is very small, the next relevant interaction in the QDM Hamiltonian may be resonances along longer loops. Let us first consider the loops C_4 and C_5 , which can be investigated by a simple extension of the previous analysis. For two dimer configurations consisting of three dimers along the loop C_4 ($c_4 = -1/2^8$), the diagonal matrix elements coincide again with the mean-field result $E_{11} = E_{22} = -9/4$ while $E_{12} = -9/2^9$. Using Eq. (12), we find that, for the properly orthogonalized basis, $\tilde{E}_{12} = -27/2^{10} = -t$ while the potential energy term is vanishingly small $V/t = 1/2^8$. For loop C_5 ($c_5 = 1/2^5$), explicit calculations yield $\tilde{E}_{12} \equiv 0$ or no tunneling. This can be understood by drawing the two dimer configurations on a corresponding cluster of a kagomé lattice and noticing that they are exact degenerate eigenstates for such a cluster.

Finally, let us consider the loops C_2 and C_3 . One cannot use the previously derived Eq. (12) in this case since, in addition to the two dimer configurations resonating along a perimeter of C_2 , there is an extra state with three parallel dimers on the same parallelogram. The first two state are denoted by $|\psi_1\rangle$ and $|\psi_2\rangle$, $\langle\psi_2|\psi_1\rangle = c'$ and the third state by $|\psi_3\rangle$, $\langle\psi_3|\psi_{1,2}\rangle = c$. Three orthogonal states are constructed similar to Eq. (10):

$$\begin{aligned} |\phi_{1,2}\rangle &\sim [|\psi_{1,2}\rangle - \mu'|\psi_{2,1}\rangle - \mu|\psi_3\rangle], \\ |\phi_3\rangle &\sim [|\psi_3\rangle - \mu(|\psi_1\rangle + |\psi_2\rangle)]. \end{aligned} \quad (15)$$

The orthogonality conditions yield $\mu \approx \frac{1}{2}c + O(c^2)$, which coincides in the leading order with Eq. (11). The second relation for the relevant case $|c'| \ll |c| \ll 1$ becomes $\mu' = \frac{1}{2}\left(c' - \frac{3}{4}c^2\right)$. The resonances around smaller loops lead to a renormalization of the large loop resonance. Now, calculating the matrix elements of the Hamiltonian between states (15), we find that the resonances on smaller loops, that is, \tilde{E}_{13} and \tilde{E}_{23} , do not change compared to Eq. (12), whereas the large loop resonance is

$$\tilde{E}_{12} \approx E_{12} + (c^2 - c')E_{11} - cE_{13}. \quad (16)$$

Using the above expression to calculate the resonance of the singlet bonds on C_2 and C_3 , we find that in both cases $\tilde{E}_{12} = 15/2^{10} = -t$. The potential energy term is again extremely small.

Following [6], let us consider now more carefully the issue of the sign of the kinetic energy coefficients t . To change the sign of the resonance matrix element for the shortest loop, one multiplies the basis states by a factor $i^{n_r + n_{l,e} - n_{l,o}}$, where, for a given dimer configuration, n_r counts the number of dimers on links pointing upwards and right and $n_{l,e}(n_{l,o})$ counts the number of dimers on links pointing upwards and left from sites with even (odd) vertical coordinates. Dimers on strictly horizontal bonds do not contribute to the phase factor. By means of this operation, every resonance move along C_1 loops picks up an extra (-1) factor, thus, changing $t_1 \rightarrow -t_1$. At the same time, the resonance moves along C_2 and C_3 loops and does not change its sign, while the sign change takes place again for the C_4 loops: $t_{2,3} \rightarrow t_{2,3}$ and $t_4 \rightarrow -t_4$. An effective QD Hamiltonian for the trimerized kagomé antiferromagnet is, therefore, dominated by kinetic energy terms for resonance moves between the orthogonal dimer configurations $|\phi_n\rangle$ and $|\phi'_n\rangle$ for every loop C_n of four different types $n = 1, \dots, 4$ on an effective triangular lattice:

$$\hat{\mathcal{H}}_{\text{QD}} = \sum_{l_n} -t_n |\phi_n\rangle \langle \phi'_n|. \quad (17)$$

The kinetic matrix elements are $t_1 = 3/2^6$, $t_2 = t_3 = -15/2^{10}$, and $t^4 = -27/2^{10}$. The tunneling matrix elements for the longer loops have no significant smallness compared to the strongest resonance move: $t_4/t_1 \approx -0.56$, $t_{2,3}/t_1 \approx -0.31$. They have also different signs, which leads to frustration and a sign problem for possible Quantum Monte Carlo investigations of this model [17].

The QDM (17) with only the shortest loop resonance was investigated in [5, 6] via mapping to a frustrated Ising model in a transverse field. The ground state of the dimer model is believed to be a crystalline $\sqrt{12} \times \sqrt{12}$ state, which consists of locally resonating dimer pairs and breaks the translational symmetry of the lattice. Such a state should have a fully gapped excitation spectrum. The properties of the QDM (17) with several dimer resonances are not clear at the moment. Since the potential terms are vanishingly small, the QD Hamiltonian is far away from the RK pint and the ground state should break certain lattice symmetries.

The excitation spectrum is also expected to be gapped unless a fine tuning of t_n drives the system towards a transition point between two crystalline states.

In conclusion, the presented derivation of QDM for a realistic spin model on a trimerized kagomé lattice illustrates the generation of small energy scales in frustrated quantum magnets. The dimer resonance matrix elements in (17) are given by small fractions of a weaker exchange constant, e.g., $t_1 \approx 0.047J_2$. In a wide temperature interval $t_1 \ll T \ll J_2$, the quantum spin systems are described by an RVB liquid of singlet pairs. At very low temperatures $T < t_1$, a valence bond crystal probably replaces the RVB state. The dimer crystallization is, however, driven by local resonances. Therefore, variational mean-field type approaches [12, 14] are not capable of describing the precise nature of the corresponding ground states.

The author is grateful to D.A. Ivanov and G. Jackeli for interesting discussions.

REFERENCES

1. P. Fazekas and P. W. Anderson, *Philos. Mag.* **30**, 423 (1974); P. W. Anderson, *Science* **235**, 1196 (1987).
2. B. Sutherland, *Phys. Rev. B* **37**, 3786 (1988).
3. D. S. Rokhsar and S. A. Kivelson, *Phys. Rev. Lett.* **61**, 2376 (1988).
4. R. Moessner, S. L. Sondhi, and P. Chandra, *Phys. Rev. Lett.* **84**, 4457 (2000).
5. R. Moessner and S. L. Sondhi, *Phys. Rev. Lett.* **86**, 1881 (2001).
6. R. Moessner and S. L. Sondhi, *Prog. Theor. Phys. Suppl.* **145**, 37 (2002).
7. A. Ioselevich, D. A. Ivanov, and M. V. Feigelman, *Phys. Rev. B* **66**, 174405 (2002).
8. A. Auerbach, *Interacting Electrons and Quantum Magnetism* (Springer, New York, 1994).
9. P. Lecheminant, B. Bernu, C. Lhuillier, *et al.*, *Phys. Rev. B* **56**, 2521 (1997).
10. C. Waldtmann, H.-U. Everts, B. Bernu, *et al.*, *Eur. Phys. J. B* **2**, 501 (1998).
11. V. Subrahmanyam, *Phys. Rev. B* **52**, 1133 (1995).
12. F. Mila, *Phys. Rev. Lett.* **81**, 2356 (1998).
13. C. Raghun, I. Rudra, S. Ramasesha, and D. Sen, *Phys. Rev. B* **62**, 9484 (2000).
14. R. Budnik and A. Auerbach, *Phys. Rev. Lett.* **93**, 187205 (2004).
15. L. Santos, M. A. Baranov, J. I. Cirac, *et al.*, *Phys. Rev. Lett.* **93**, 030601 (2004).
16. M. Mambrini and F. Mila, *Eur. Phys. J. B* **17**, 651 (2000).
17. Similar results have been recently obtained by F. Mila *et al.*, private communication (2004).